PHYSICS-BASED FORWARD MODELING OF MULTISTAGE HYDRAULIC FRACTURING IN UNCONVENTIONAL PLAYS

A Dissertation

by

SERGEI PARSEGOV

Submitted to the Office of Graduate and Professional Studies of
Texas A&M University
in partial fulfillment of the requirements for the degree of

DOCTOR OF PHILOSOPHY

Chair of Committee,	David S. Schechter
Committee Members,	Sara Abedi
	Frederick Chester
	Jeff Spath
Head of Department,	Jeff Spath

May 2019

Major Subject: Petroleum Engineering

ABSTRACT

This dissertation proposes a workflow for modeling of multistage hydraulic fracturing stimulation in unconventional formations. Based on the field case of a horizontal well targeted lower Wolfcamp formation in Midland Basin, this study identifies main gaps of publicly available data and provides estimations for critically important inputs: elastic properties, horizontal stress anisotropy, and pressure dependent leakoff.

Breakdown and shut-in pressure are used to constrain horizontal stress anisotropy to a narrow range of 7.6-11.0% and avoid misleading published data for the Midland Basin. The developed model shows that oilfield operators can significantly, up to two times, reduce the size of the pad and associated cost without risk of streenout. From the estimation of friction losses and modeling in planar-3D model this work shows how to overcome adverse effects of stress shadowing by perforation redesign and reduce cluster spacing.

Finally, fracture conductivity and production history are used to model fluid flow in two reservoir simulators. History match demonstrates that effective permeability should be several orders of magnitude higher than measured from the pressure pulse decay method.

This dissertation will be useful for completion and reservoir engineers.

ACKNOWLEDGMENTS

I want to thank the committee chair, Dr. Schechter, and committee members: Dr. Abedi, Dr. Chester, and Dr. Spath for their guidance and support throughout this research.

I also wish to thank my colleagues Fan Zhang, Geng Niu, Kiran Nandlal, Dr. Marcelo Laprea-Bigott, and Dr. Ruud Weijermars for their contribution to papers and text of this dissertation.

Thanks also go to all friends and colleagues in the Petroleum Engineering department for making my time at Texas A&M University a great experience.

CONTRIBUTORS AND FUNDING SOURCES

This work was supported by Crisman Institute for petroleum research and Nexen Energy ULC (NEXEN).

NOMENCLATURE

ANI	=	Horizontal stress anisotropy, $(S_{Hmax} - S_{hmin})/S_{hmin}$, [%]
A_φ	=	Horizontal stress anisotropy, $(S_{Hmax} - S_{hmin})/(S_v - S_{hmin})$, [1]
B_c	=	A ratio of fracture aperture to the proppant grain diameter, [1]
BEM	=	Boundary Element Method
C	=	Leakoff coefficient, [ft/min$^{0.5}$]
C_{fd}	=	Dimentionless Fracture Conductivity
CFOP	=	Critical Fissure Openning Pressure, [psi]
DDM	=	Displacement Discontinuity Method
DFIT	=	Diagnostic Fracture Injection Test
DFN	=	Discrete Fracture Network
DTC and DTS	=	Compressional and shear slowness respectively, µs/ft
FEM	=	Finite Element Method
FIB	=	Focused Ion Beam
h_f	=	Fracture height, [ft]
p_i	=	Initial reservoir pore pressure, [psi]
P_e	=	Effective stress, [psi]
P_p	=	Pore pressure, [psi]
PR	=	Poisson's ratio
PRREST, PRPHIA, PRGR, and PRDTC	=	Synthetic Poisson's ratio log calculated from respective resistivity, total porosity, gamma, and compressional slowness
PZS	=	Process Zone Stress, [psi]

LEFM	=	Linear Elastic Fracture Mechanics
MEM	=	Mechanical Earth Model
Np	=	Proppant number
$q_{leakoff}$	=	Leakoff rate, [ft^3/min]
SEM	=	Scanning Electronic Mictoscopy
S_{Hmax}	=	Total maximum horizontal stress, [psi]
S_{hmin}	=	Total minimum horizontal stress, [psi]
S_v	=	Total vertical stress, [psi]
VRo	=	Vitrinite reflectance
V_p and V_s	=	Compressional and shear sonic velocities respectively, [ft/sec]
w_f	=	Fracture width, [inch]
X_f	=	Fracture half-length, [ft]
YM	=	Young's modulus, [Mpsi]
α	=	Vertical Biot's poroelastic coefficient
ρ_b	=	Bulk density, [g/cc]
$\emptyset$	=	Porosity, [1]
μ	=	Viscosity of hydraulic fluid, [cP]

TABLE OF CONTENTS

LIST OF FIGURES

Page

LIST OF TABLES

Page

1. INTRODUCTION AND LITERATURE REVIEW

This dissertation consists of five chapters. Literature review in the first chapter identifies gaps in existing knowledge of hydraulic fracturing modeling. The second chapter is dedicated to the analysis and quality check of publicly available input data for the numerical simulation of multistage hydraulic fracturing for the case study area of Upton County, the Midland Basin. Chapter 3 presents the main modeling results and identifies limitations of grid-based modeling tools. Chapter 4 demonstrates the value of modeling results and the ability of integration between hydraulic fracturing simulator and reservoir simulator for single and dual-porosity formulation. Finally, Chapter 5 provides conclusions and summarizes the contribution of this work.

1.1.History of hydraulic fracturing

Hydraulic fracturing is a near wellbore treatment by injecting liquid slurry at a pressure higher than minimum closure stress. The primary objective of hydraulic fracturing is to break formation to either increase near wellbore effective permeability by creating new conductive channels and keeping them open for low permeable formations via proppant or by acid fracturing; or to improve stress regime of target interval near wellbore and prevent well from extensive production of solid particles (“frac-pack”).

In contrast to well-known explosion type torpedoing of open hole Roberts (1866), hydraulic fracturing is generally relative long process securing proppant agent transport or necessary timing for chemical reactions. The concept of fluid induced fracturing most likely rooted in production increase resulted from incidental fracturing of injection wells. Today

injection of co-produced brine at pressures higher than fracture gradient is a common practice for water utilization and as IOR technique.

Hydraulic fracturing was field tested for 240 ft limestone formation in 1947 by Halliburton for Stanolind Oil company in the Hugoton gas field, Kansas. As described by Smith and Montgomery (2015) the treatment was comprised of 1,000 gallons of napalm, followed by 2,500 gals of gasoline with amine breaker sand from Arkansas river was used as a proppant. A typical hydraulic fracturing treatment starts with a "pad" stage of fracture fluid without proppant to create sufficient width for further proppant transport in the fluid-proppant mixture called slurry.

In one of the pioneering publications discussing the new method, Clark (1949) mentioned a significant increase of production in 11 out of 23 treated wells and proposed pumping viscous oily fluid with carried propping agent at rates higher than leakoff. He also described shallow hydraulic fracturing experiments of military grade napalm (jellied gasoline) injection into tight sandstone as a target formation 15 ft deep.

First commercial use of fracture treatment took place on March 17, 1949, near Duncan, Oklahoma. In the USSR hydraulic fracturing was used since 1952 in test and since 1954 in industrial applications. By 1955 more than 100,000 hydraulic fracturing treatments were done in the United States only. It was found that hydraulic fracture propagates perpendicular to the direction of the least principal stress Hubbert and Willis (1957).

Multiple efforts were done to predict an increase of production due to horizontal plane fracture in shallow Crawford and Landrum (1954), where minimum principal stress is an overburden; and vertical/inclined fracture Crawford and Landrum (1955) in more deep formations, where the minimum stress will likely be horizontal. It was found that "infinite

conductivity" fracture may increase production up to three times compared to that before fracturing.

In order to propagate fracture into formation three conditions must be met:

1. Fluid pressure in the wellbore should be higher than required for initial rock breakdown (initial rock strength). As it will be shown below for some well orientations and stress regimes, initial breakdown pressure may be higher than overburden stress.
2. Fluid pressure inside fracture must be higher than local minimum stress (usually minimum horizontal stress) to generate positive net pressure. In this work value of treating pressure will be used as a calibration parameter for the hydraulic fracturing model.
3. The fluid rate should exceed the rate of leakoff out of the fracture via matrix infiltration and leakage into the secondary fracture system.

At the same time, transport proppant inside created fracture requires that local fracture width should be enough to avoid bridging and keep at least part of particles in suspension.

The following Sections of Chapter I will cover publications focused on these conditions.

1.2. Initial fracture propagation and growth

Griffith (1921) showed that the rupture propagation of fracture in tension (Mode I) requires tensile stress an order of magnitude lower than is coming from the strength of molecular forces inside isotropic material. One possible explanation is the presence of multiple cracks inside the material several thousand molecules long. For the 3D case, Griffith's theory

was extended by Sack (1946); Sneddon (1946). It was shown that the crack becomes unstable and grows if the principal stress normal to the crack plane exceeds some critical value.

A common misconception though is that for horizontal wellbores hydraulic fractures tend to be vertical and propagate in the direction of maximum horizontal stress (transverse fractures). Most of the commercially available hydraulic fracturing simulators ignore the growth of longitudinal fractures (Section 1.3).

According to classical 2D analytical solution of Kirsch (1898), confirmed by experimental photoelastic method by Frocht (1941) and extended for 3D case of deviated wellbore by Weng (1993), tensile fracture will initially grow in the direction of local maximum stress, along the wellbore, regardless of the far field stress state and only after propagation beyond some predetermined distance.

It is possible for the fracture plane to turn toward the direction of maximum far-field stress, forming the S-shape curve in the map view. The reason for that is the additional tangential ("hoop") stress around the wellbore formed because of rock removal exceed both minimum and maximum horizontal stress and force fluid to open rock in the local direction of maximum stress and create near wellbore tortuosity. The difference in breakdown pressure to different perforation angle may lead to limited entry and high-pressure loss due to a limited number of open perforations.

Therefore, breakdown pressure, fracture extension pressure, and closure pressure potentially can be used for the determination of principal stresses. Hubbert and Willis (1957); Kehle (1964) made the first two models with penetrated or non-penetrated fluid assumptions. However, Gretener (1965) showed that inferred high value of maximum horizontal stress (near

overburden stress) might be an artifact of underlying assumptions. Also, he explained that in the general case of vertical well, the number of unknowns exceeds the number of equations.

Because of its importance, values of minimum and maximum horizontal stresses are of constant debate, and there is a need to constrain assumptions of physical based fracture propagation models. As will be shown in Chapter 2 questionable data from existing literature may lead to inconsistent results of physics-based modeling.

Weng (1993) analytically predicted the propagation of multiple transverse fractures from a single perforation cluster of horizontal wellbore. Weijers et al. (1994) presented laboratory experiments of fractures reorientation near wellbore to far-field stress direction. For open hole horizontal wellbore drilled in the direction of minimum horizontal stress longitudinal fracture initiated at a relatively high horizontal stress anisotropy (ANI) of 25%:

$$ANI = \frac{S_H - S_h}{S_h} = 25\%$$

Later Abbas et al. (2013) through detailed dimensionless analysis studied early fracture propagation. They concluded that initial wellbore compressibility effects would dominate first 150 wellbore radii (or ~56 ft), after which an infinite medium approach may be applied. For laboratory scale experiment it was shown that, for realistic geometries (up to 60 times wellbore radius), injection system compressibility would dominate in fracture propagation all times. Waters et al. (2006) showed the presence of axial and transverse drilling-induced tensile fractures (DITF) for horizontal wellbores in Barnett Shale. Mahrer (1999) summarized a review of the published evidence of multiple fractures propagation up to 120 ft from the wellbore and concluded that wellbore orientation, perforation design, treatment rate, and pressure significantly affect the probability of near wellbore screenout.

Warpinski et al. (1993) provided coring through experiment description for MWX hydraulic fracturing stimulation conducted in 1983-1984 and cored out in 1990. It was the first documented data for relatively deep deltaic formations (TVD 7,100 ft). They figured out parallel echelon propagation of multiple vertical fractures (32 separate fractures in 4 feet interval showed in **Figure 1**), with only two fractures were identified to be natural. Abounded cross-linked gel residuals effectively glued fracture surfaces with small (~200) mesh sand particles. For two fractures 1-3 mm offsets were reported at crossings with horizontal bedding planes of 1-2 mm thick.

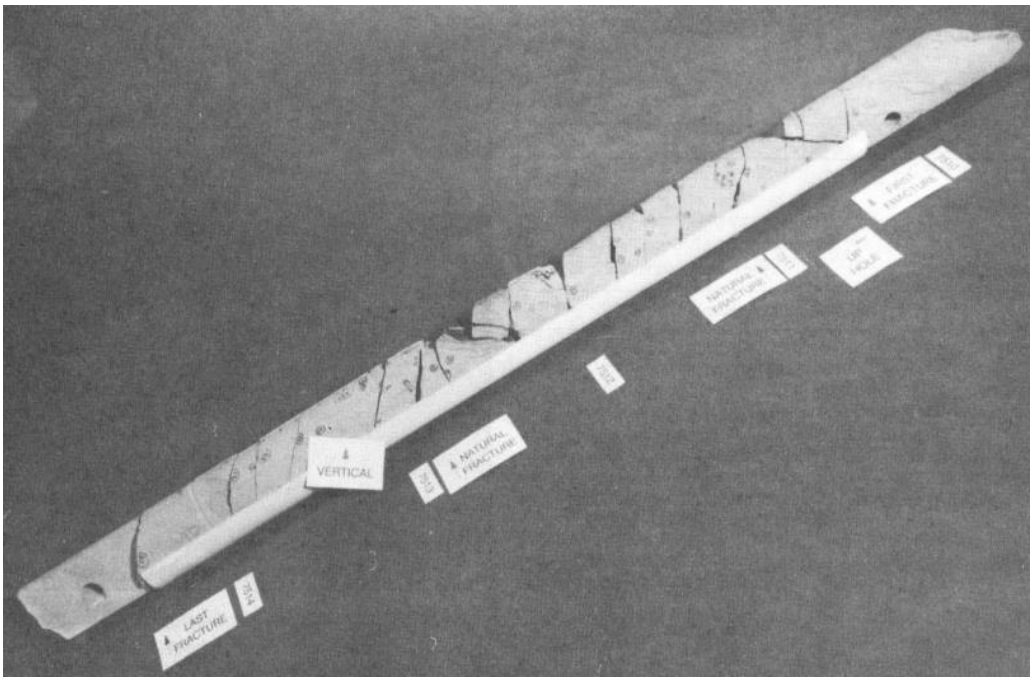

Figure 1 Photography of inclined core drilled through the MWX experiment area. Length - 4 ft, with 32 vertical fractures. Reprinted with permission from Warpinski et al. (1993).

Complex fracture behavior was also confirmed for horizontal wells with multistage hydraulic fracturing in lower Eagle Ford formation in 2014-2016 by ConocoPhillips published

by Raterman et al. (2017) and in 2016-2018 in Permian Basin by Laredo Petroleum Inc. published by Ciezobka et al. (2018).

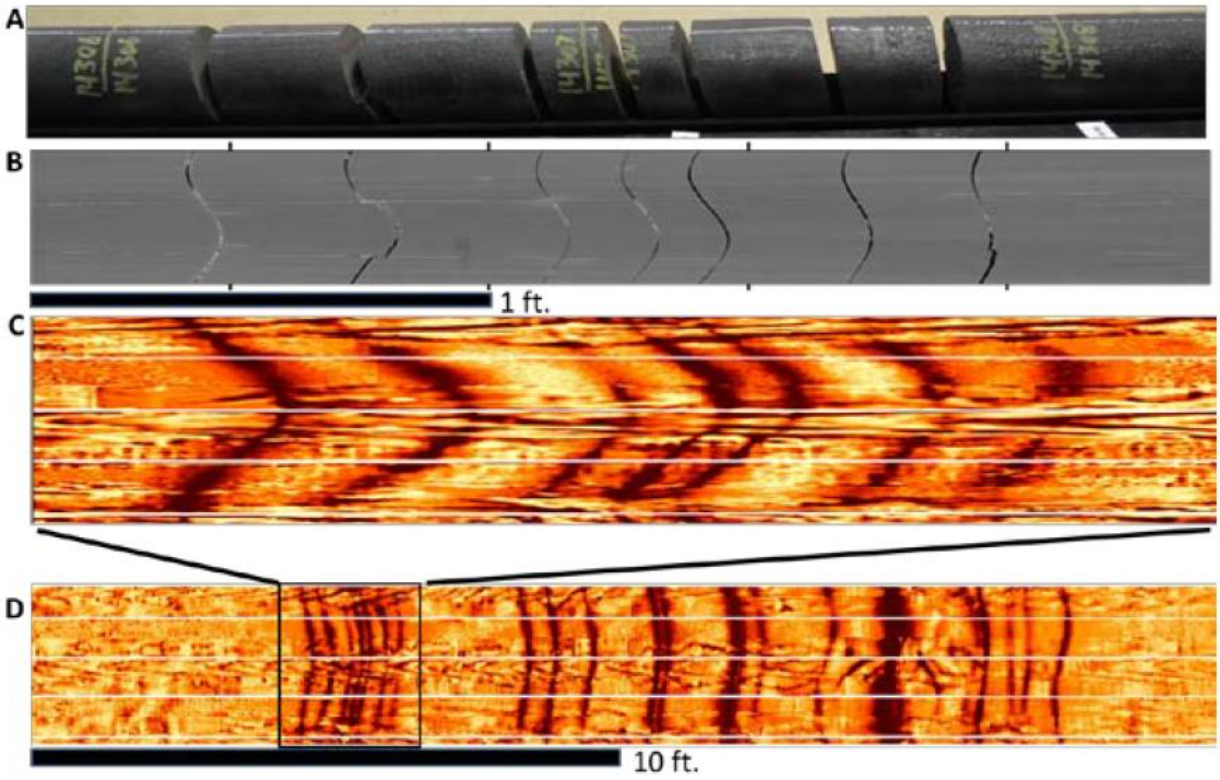

Figure 2 Hydraulic fracture swarms in Eagle Ford formation. Dipping at 75-80^0 parallel hydraulic fractures inches apart. Reprinted from Raterman et al. (2017) with permission from URTeC, whose permission is required for further use.

1.3. Evolution of hydraulic fracturing models

The first analytical model, coupling fluid flow and rock mechanics to describe fracture geometry during pumping, was proposed by Khristianovic and Zheltov (1955) – KGD model. Without numerical methods available today they used a complex variable analysis for a two-dimensional (2D) formulation. Later, Perkins and Kern (1961) developed the second 2D model abbreviated as PKN.

Two 2D models assume constant fracture height, but have a different assumption about fracture geometry in vertical (Z) direction: PKN model assumes long fracture (L>H) and elliptical fracture cross-section (in XY plane), whereas KGD – a short fracture (H<L) and rectangular fracture in XY plane. PKN is more applicable when fracture length is more than height, KGD – in the opposite case. For fracture height growth prediction in through a system of three symmetrical layers, Simonson et al. (1978) proposed an analytical solution for fracture height confinement. Fung et al. (1987) extended Simonson's equations for an asymmetric multilayer case. Liu and Valkó (2017) corrected typos in legacy deriviations and generalized height confinement for any number of layers in the generalized semianalytical lumped P3D model. It was shown that fracture toughness is a much smaller confining factor comparing to horizontal stress difference.

With the development of numerical models and CPU capacity coupled equations governing fracture propagation, elasticity, fluid, and proppant flow are solving numerically on the grid. This transition allows relaxation of the constant height assumption.

As the next step grid based pseudo-3D (e.g., MFrac/MShale) and planar-3D models (e.g., GOHFER and StimPlan) were proposed to capture nonuniform height growth, effects of individual formation layers, and mechanical interaction between fractures ("stress shadowing"). Numerical models attempt to couple numerical solutions for rock mechanics, fluid flow, and proppant particles transport in the most physical and the least computationally expensive way.

Pseudo-3D models do not consider fracture geometry variation in three dimension geometry; instead, they use a modification of PKN or KGD models, coupled with height variation along the fracture length and associated width variation. Settari and Cleary (1986) used a numerical solution of vertical propagation problem with a singular integral equation on a

suitable set of Chebyshev points. Reported increase of numerical burden for presented software (currently known as FracPro) was extra 50%, comparing to 2D simulations.

Planar 3D models are generally more accurate than P3D, they do not rely on assumptions of fracture propagation from a layer of minimum closure stress and hence allow to model fracture pinch out as it demonstrated in Chapter 3. P3D models, however, provide inaccurate height and width prediction, but two orders of magnitude faster than Planar-3D what is essential for practical use as mentioned by Cohen et al. (2017).

As for numerical techniques for solving a problem of elastic response of fracture wall for fluid pressure Barree (1984) uses simplified formulation based on Boussinesq (1885) solution for displacement at homogeneous half-space, with (x, y) to be a vertical plane:

$$u(x,y) = \frac{1 - PR^2}{\pi \cdot YM} P_{net}(x,y) \iint d\psi dr$$

To some degree, this approach may be extended for heterogeneous formation by putting Young's, Poisson's ratio and net pressure under the integral as a function of local radial coordinates r and ψ:

$$u = \iint \frac{1 - PR^2}{\pi \cdot YM} P_{net} d\psi dr$$

The validity of this simplification approach depends heavily on the low variation of Young's modulus assumption and the fact that the influence function is fast declining with distance as $1/r^2$. Additional simplification of the numerical model may be achieved with introducing a shear decoupling radius, introducing the upper limit of the integration:

$$\iint d\psi dr \approx \frac{\Delta x \cdot \Delta z}{\pi \cdot r^2} \sim 1/r^2$$

Shear decoupling radius (an order of 20 ft) may be a numerical "knob" which describes the loss of full elastic coupling required by LEFM over the whole fracture (infinite decoupling radius). The physical meaning of such parameter though may be found in multiple shear slippages of the fracture face detected by microseismic monitoring. Shear failure releases part of elastic energy and limits transmission of elastic deformation far from perforations.

Barree and Winterfeld (1998) demonstrated what such parameter decrease height, width, and length of the resulted fracture. In addition to that slippage increases leakoff and decrease net pressure. Therefore, shear slippage detected by microseismic events may be an effective fracture confinement mechanism in addition to stress contrast along height (between layers) and along fracture length (transverse heterogeneity).

At the same time, the proposed simplified approach may not adequately describe heterogeneity of mechanical rock properties (YM and PR), and local net pressure may result in significant width profile errors for the heterogeneous reservoir. Presence of thin layers with contrast mechanical properties may magnify these numerical artifacts. This behavior of numerical models is covered in more details in Section 3.1.

In this case, a more rigorous Finite Element Method (FEM) used by Smith et al. (2001), or the Boundary Element Method (BEM) proposed by Crouch and Starfield (1983) may be required. BEM has an advantage of reduced dimensionality since the only 2D boundary of the 3D domain is discretized. For three layers problem, Peirce and Siebrits (2001) proposed Discrete Discontinuous formulation which reduces numerical burden for fracture propagation problem near the bedding plane by applying the asymptotic solution.

A few fracturing simulators today predict the propagation of hydraulic fractures in naturally fractured media with an explicit description of the interaction between natural and

hydraulic fractures extending interaction criteria of Renshaw and Pollard (1995). These models have their limitations such as:

- 2D geometry, presented by Shetty and Lin (2014)
- predefined paths for fracture propagation McClure et al. (2016)
- vertical DFN and height confinement via stacked pseudo-3D models, as described by Cohen et al. (2017); Kresse et al. (2013), (2011).

Overall, the use of true 3D DFN in the modeling of the secondary fracture system is extremely computationally expensive and available only for research purposes for supercomputers as described by McClure et al. (2015). In addition to that, limited knowledge of the initial fracture system leaves uncertainty of the exact location and orientation of fractures. At the same time, as it will be shown further, modeling of leakoff into such secondary system is essential for proppant placement problem as well as in the design of proppant schedule required to maximize fracture conductivity without increasing risk of screenout.

1.4. Stress state and geomechanical model

All grid-based models require knowledge of properties (such as density, porosity, Young's modulus, and Poisson's ratio) distribution from cell to cell (Mechanical Earth Model - MEM) extracted from log data, core calibrations, and downhole stress tests. The total minimum horizontal stress for each grid cell may be estimated assuming uniaxial vertical strain as proposed by Eaton (1969) and with further improvement by Daines (1982) to include tectonic stress component:

$$S_{hmin} = \frac{PR}{(1 - PR)}\left(S_v - \alpha \cdot P_p\right) + P_p + S_t$$

where S_v – vertical stress may be obtained by integration of density log.

Smith et al. (2001) demonstrated that the vertical variation of Poisson's ratio might effectively prevent vertical growth by creating grid blocks of higher closure stress. Similar results were obtained with an analytical model of Liu and Valkó (2017). At the same time, a spatial variation of YM is rarely covered, whereas this variation creates a local contrast of resulted fracture width, which in turn creates additional constraints for proppant transport.

For highly anisotropic formations (e.g. tight shales of the Horn River Basin) Hamza et al. (2018); Suarez-Rivera et al. (2006) proposed to use VTI (Vertical Transverse Isotropy) model and more complex calculation of minimum horizontal stress assuming that PR, YM, and Biot's coefficient have different values parallel and perpendicular to bedding planes as follows:

$$S_{hmin} = \frac{E_h}{E_v}\frac{PR_v}{(1-PR_h)}\left(S_v - \alpha_v \cdot P_p\right) + \alpha_h P_p + S_t$$

Minimum horizontal stress and stress contrast of fracture barriers will be higher for the anisotropic case, whereas breakdown pressure will be lower than for isotropic model which may be crucial for fracture design in such formations as proposed by Suarez-Rivera et al. (2011).

High-quality cross dipole sonic log (Stoneley, compressional, fast shear, and slow shear wave slowness) is required as well as calibration with triaxial tests in multiple orientations on core samples to estimate all required parameters. In addition to that, multiple anisotropic models: ANNIE, modified ANNIE (MANNIE) and more complicated models provide a range of S_{hmin} in order of 10% depends on underlying assumptions Aderibigbe et al. (2016), which is comparable to uncertainty in isotropic cases for practical applications. As it described in Chapter 2, datathe set for the treatment well contains only compressional and shear slowness.

For specific cases of high anisotropy or heterogeneity, numerical modeling of hydraulic fracturing may be done by populating the grid from third-party wellbore mechanical or full-scale geological models.

Multiple attempts were made to correlate existing logs and seismic data into a facies model to better characterize the geomechanical model. The following resolutions of geological models are reported in the area of interest:

- Cherian et al. (2018) - 100 ft x 100 ft x 2 ft, with Shmax orientation at N 100-104^0
- Casey (2018) – 300 ft x 300 ft x 2 ft
- Dommisse et al. (2018) – 750 ft x 750 ft x 3 ft

The main benefit of the proposed lithofacies model is an ability to resolve layers below limitation logs resolution and, at the same time populate lateral variation of properties along the wellbore and in the direction of fracture propagation. The initial objective of the development of such models is to better characterize formation for calculation of OOIP and main geological attributes – porosity, water saturation, TOC, and sometimes dynamic geomechanical properties.

Unfortunately, to the date, such models are not publicly available and have no systematic use in hydraulic fracturing modeling due to the following limitations:

- Lower than required lateral resolution – hundreds of feet vs. tens of feet. It should be noted that for practical use of lithofacies models they should have a lateral resolution not worse than the grid size of the fracturing model grid (~10 ft). Scale depended effects associated with grid models are discussed in Section 3.1.
- The lack of static geomechanical attributes (YMS and PR) for stress state calculation and elastic response of the fracture. This gap will be addressed in Section 2.5.3

- The absence of pore pressure estimation, and other required attributes for hydraulic fracturing models. This gap will be discussed in Sections 2.3.2 and 2.4.

Vertical stress may be easily calculated from the integration of the overburden density log. It is generally assumed that the vertical stress gradient in the area of interest is in range of 1.0-1.1 psi/ft as published by Agharazi (2016); Friedrich and Monson (2013); Shoemaker et al. (2019); Xu and Zoback (2015). Higher assumed vertical stress gradient transfers into higher treatment pressure and increases stress contrast between barriers and target zone.

Direct measurement of minimum horizontal stress in unconventional reservoirs, however, is challenging because of low matrix leakoff and extended period of fracture closure. Multiple techniques are developed to overcome this issue including step rate tests, equilibrium rate test, correlation of closure pressure with ISIP. Each method, however, has its limitation, and therefore crosschecking is required to establish reasonable value of minimum horizontal stress.

Maximum horizontal stress is the most challenging to measure. As it will be shown in Chapter 2, very limited publications are available with reported horizontal stress anisotropy, and a consensus is yet to be achieved on how to interpret inversion of microseismic moment tensor data. At the same time, some estimation of maximum stress anisotropy may be made from breakdown or closure pressure, overburden stress and pore pressure for inclined wells with simultaneous inversion as proposed by Hossain et al. (1999); Huang et al. (2011).

1.5. Permeability measurements

In traditional steady-state permeability measurement, the specimen is subjected by constant fluid flux there as pressure drop is measured between specimens borders. For Ultra-

Low Permeability (ULP) formations (absolute permeability less than 0.1 mD) it is unpractical to conduct such flow experiments for two main reasons: extremely low possible flux with associated measurements issues and the extremely long period of establishing steady-state flow. Therefore starting with pioneering work of Passey et al. (2010) multiple attempts were made to use transient flow methods: pulse and pressure decay. Ning (1992) further improved pressure decay method was to capture a fast response from the fracture system and much slower dissipation of pressure pulse in the matrix.

For Devonian age gas prone shales of Appalachian basin, Luffel et al. (1993) developed gas pulse decay method (now commonly known as Gas Research Institute - GRI method) for crushed core samples. Guidry et al. (1996) reported a new method of measuring porosity and water saturation in drilling cuttings; they also proposed a technique for permeability measurement for core samples in the range from 1 to 20 $x10^{-8}$ mD. Authors claimed that permeability measured on crushed samples was in satisfactory agreement with that from core plugs under confinement, whereas previous studies inferred from one to two orders of magnitude higher gas permeability for unconfined rock chips.

Even though it is safe to conclude that inside one laboratory permeability, calculated with different methods lead to similar values; a problem of inconsistent results between laboratories is not yet solved. Sondergeld et al. (2010) reported two-three orders difference in measured permeabilities of the same rock samples. Therefore, it is important to find multiple literature sources for the same formation in addition to publicly available porosity-permeability correlation from the target well.

Mathur et al. (2016) conducted pressure build up and pulse decay measurements as well as comparison with the steady-state flow for five Wolfcamp core samples. After double-slip gas

correction, they found a reasonable agreement in the 30% range with permeability varying (from sample to sample) from 8 to 800 nD.

Later, Bhandari et al. (2019) measured permeability of two ("as received") lower Wolfcampian core samples from Delaware basin with the depth comparable to the target well (TVD of 11,750 ft in the paper versus 10,500 ft for this study). With two methods: transient pulse decay and steady-state dodecane under confinement, it was found that individual facies of heterogeneous core samples have matrix permeability in a range from 30 to 1000 nD. Steady-state measurements along bedding planes took 1.5 months per test to achieve steady-state flow at confinement pressure of 4,350 psi.

For such low permeabilities, Carter leakoff model published by Howard and Fast (1957) leads to unrealistically low leakoff coefficient and high values of fluid efficiency. At the same time, propagation of fracture fluid out of the main fracture plane was previously documented for Barnett shale by Fisher et al. (2004), (2002). The slurry plugged observation wells 500 ft out of the fracture direction. Identified from tiltmeters "fairway" width was as wide as 900 ft. Downhole tiltmeters showed fracture half-length of 2,500 ft, while analysis of microseismic reveals X_f = 1,500 ft.

Therefore, matrix permeability measured from GRI pressure decay test (or with an alternative technique) alone cannot describe flow behavior during hydraulic fracturing and production. Thus, without correction of matrix permeability for created effective permeability of the fracture system (enhanced permeability) or applying dual porosity model, reasonable fluid production rate would require unrealistically high-pressure depletion.

1.6. Leakoff model

Since hydraulic fracturing requires injection of fluid in porous and permeable media, fracturing fluid tends to leakoff out the main hydraulic fracture plane. To correctly place proppant into open tensile fracture an engineer has to calculate an optimal pumping schedule which maximizes the effect of fracturing on hydrocarbons production.

For conventional formation, Nolte (1986) proposed a practical proppant schedule design solution (typically 20-60% of the proppant-free pad and power low proppant concentration curve) assuming the following:

1. Carter's leakoff model and hence constant fluid pressure along the fracture.
2. Known fluid efficiency from pressure decline test (mini-frac or DFIT).
3. High viscous fracture fluid can keep proppant in suspension.

Smaller that required pad size may lead to slurry dehydration, proppant bridging inside the fracture, and premature screenout. At the same time, if pad volume is more than needed, some portion of the fracture will not have designed proppant concentration, and part of horsepower of pumps will be underutilized.

At the same time, early experiments with hydraulic fracturing in ultra-low permeability reservoirs showed the following problems: screenouts at steady treatment pressure, formation damage, higher than expected leakoff. The solution for this discrepancy may be found in secondary leakoff mechanisms. Warpinski (1990) based on MWX test site data proposed activation of secondary fractures with an increase of local fluid pressure to threshold value activating dilation of preexisting natural fractures. Reported leakoff rate after threshold increased by fifty times comparing to matrix leakoff. He also presented experimental data showing successful use of 100 mesh proppant to control excessive pressure dependent leakoff.

Nolte and Smith (1981) derived a condition for a tensile opening of vertical natural oriented in any direction to the main hydraulic fracture:

$$P_{net} > \frac{S_H - S_h}{(1 - 2 \cdot PR)}$$

It will be shown in Chapter 2.8.1., net pressure, required for tensile opening of fissures depends on orientation as proposed Delaney et al. (1986) and may occur at pressures significantly lower than with estimation of Nolte and Smith (1981).

In addition to the opening of fissures in tensile (Mode I), shear (Mode II) failure of natural fractures and discontinuities may be an additional mechanism of increasing leakoff at a lower pressure.

The hydraulic fracture may continue propagation along the direction of maximum horizontal stress after reinitiation with an offset along natural fracture forming a “dogleg” across the crackShear stimulation will require lower net pressure than the tensile opening and may be part of mixed mode stimulation as described by McClure (2012).

Secondary leakoff may be described from stochastically generated DFN with limitations discussed by Parsegov et al. (2018b), or by the following practical approaches of effective media:

- Fluid loss multiplier for leakoff into DFN proposed by Meyer and Bazan (2011).
- Pressure-dependent leakoff – PDL (or more correctly - pressure dependent coefficient of leakoff) by Barree and Mukherjee (1996).
- Dual porosity models initially proposed by Warren and Root (1963) and used in combined hydraulic fracturing- reservoir simulator by Mcclure and Kang (2018).

Industry fracturing simulator should, therefore, support dual leakoff mechanisms in addition to matrix leakoff through the fracture faces.

1.7.Proppant transport

As slurry moves in the fracture more dense proppant gradually moves downward as a result of gravity force. In addition to gravity settling, slurry experiences leakoff and concentration of proppant rises along fracture length. For highly viscous fluids proppant stays in slurry long enough for concentration rise due to leakoff. In thin fluids settling might be so fast that the concentration of suspended proppant does not rise significantly. Propped fracture geometry depends on the ability of proppant particles travel vertically and laterally without bridging and taking stress from walls and related shear strength.

1.7.1. Bridging condition and tip screenout

Length and height of created hydraulic fracture are higher than propped ones because proppant cannot reach all formed fracture surface. At some critical width, the proppant inside the fracture begin bridging and block following particles from further propagation through the sand pack. One of the practical limitations is the ratio of fracture width and proppant diameter (B_c). Gruesbeck and Collins (1982) conducted laboratory bridging experiments along circular holes mimicking perforations. The experiments show that with $B_c > 6$ no practically achievable concentration lead to bridging. At the same time bridging occurs depends on concentration at $B_c < 6$. At $B_c < 2$ bridging occurs at any concentrations in the lab. Therefore $B_c > 3$ was a common design parameter Economides et al. (2002); Schechter (1991); Smith and Montgomery (2015).

At the same time, bridging in vertical slots (open fracture) should be fundamentally different from bridging over round holes in the casing. Barree and Conway (2001); Ray et al. (2017) performed proppant flow experiments in slots with variable width to imitate real fractures and observed that bridging starts at Bc close to one for both Newtonian and non-Newtonian fluids. At the same time, due to wall effects, proppant has the highest velocity in the center of the slot, and such proppant velocity is higher than average fluid velocity (acceleration effect). Therefore, engineers overdesign fractures with a higher desired fracture width and net pressure. Higher net pressure, especially in the proximity to the wellbore, may lead to an opening of secondary fissures and increase local leakoff.

Barree and Conway (2001) also noted that such fissures opening might significantly decrease the efficiency of proppant transport by triggering bridging near such fissures. Even with 95% fluid efficiency, the area near open secondary crack may lead to proppant accumulation in the main fracture, the sudden growth of backpressure, and, hence, a screenout. Therefore it may be advisable to decrease the pumping rate and related treatment pressure to reduce bridging at the end of the proppant ramp-up stage. Here is one of the knowledge gaps to be addressed in the dissertation.

1.7.2. Transport model in thin fluids

The regime of vertical proppant transport depends mainly on fracture fluid type. In his work Nolte (1986) assumed no settling of proppant particles to the bottom of the fracture and ideal viscous drag transport in slurry along the fracture length. With the revolutionary engineering paradigm shift from cross-linked gels to slick-water engineer, however, should consider a very fast settlement of the proppant and further avalanching over settled proppant

bed. Therefore proppant rump up design should be developed based on more feasible transport models.

The first physical models for sand transport in vertical slots with thin fluids (viscosity 10 cP and lower) can be traced to the original work of Kern et al. (1959) which postulates that sandbank is formed near the wellbore with early pumped sand and, therefore, highly conductive proppant should be pumped the earliest. In multiple experiments, it was shown that settled proppant might propagate further along fracture length at a fluid velocity higher than the resuspension limit.

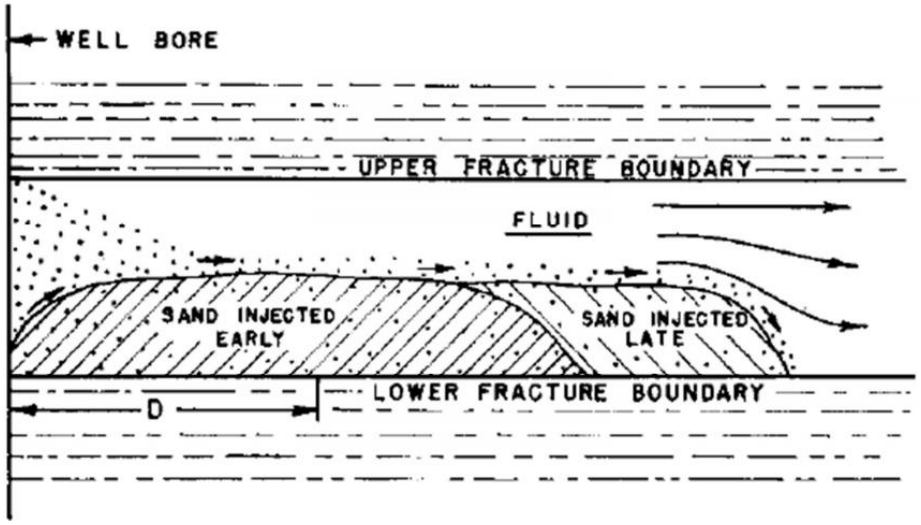

Figure 3 Immobile sandbank and mobile bed of sand in slot experiment with thin fluid. Reprinted with permission from Kern et al. (1959).

The authors also provided the first empirical rules for the overflush procedure without proppant washout near the wellbore. Since fracture area near entry perforations have significant turbulence and low equilibrium height of proppant pack, it was recommended to reduce the

pumping rate at overflush stage and hence keep the equilibrium pack covering the wellbore to ensure sufficient conductivity.

Blot and Medlin (1985) Medlin et al. (1985), however, challenged results of laboratory experiments of Kern et al. (1959) and pointed out that equilibrium proppant height should be scaled with a total fracture height which was not observed in their 1 ft by 20 ft slot experiments. Therefore, they concluded that the mobile bed transport mechanism might be efficient in the laboratory, but in the field scale, the viscous drag mechanism should dominate. They argued that equilibrium sand height is seldom achieved and additional mechanisms of transportation is required to describe large volume fracturing treatments.

Slot experiments with a slick-water design of Patankar et al. (2002), showed the similar transport pattern in a wide range of parameters - only a thin upper layer of the proppant pack is moving. Experimental results were generalized as correlations of Wang et al. (2003).

Based on a comparison of abovementioned laboratory experiments Woodworth and Miskimins (2007) extrapolated laboratory bi-power law correlations to the field scale in the analytical form applicable to fast calculations in hydraulic fracturing simulators. These correlations for the top of the clean fluid region and of movable proppant bed ("proppant carpet") at equilibrium conditions provide a useful instrument for proppant schedule optimization in thin fluids with viscosities of 10 cP and below. It was also shown that a smaller ratio of fracture width to proppant diameter is beneficial for proppant transport along the fracture length. The increase in pump rate also decreases equilibrium proppant height.

Fast proppant settling problem may be valid also for hybrid designs, where clean fluid pad and proppant rich slurry have a significant density difference. In this case, slurry withholding proppant will settle as a more dense phase, and clean fluid will be pushed on the

top of the fracture. Use of a large pad size increases that effect of convective settling due to excessive creation of height and width. Therefore modeling software should include advanced physics-based proppant transport models.

For the pad stage localized leakoff may also be undesirable since cubic law will predominantly support leakoff via a small number of fissures with highest hydraulical aperture, while the final objective of pad stage in unconventional hydraulic fracturing is to create dense fracture network. Localized leakoff also undesirable for multicluster fracturing job, because it makes fluid and sand distribution unequal between individual clusters due to premature screenout at some of the perforation clusters. Since a significant amount of proppant may be transported into mechanically open fissures before bridging, pumping of small mesh sand at low concentrations during pad stage may reduce secondary leakoff and redistribute fluid flow for fractures of lower aperture.

An additional complication for proppant transport may be caused by the development of axial fractures which may take not only pad fluid, but some amount of proppant and further decrease the volume of proppant pack available for transportation into the main fractures. Meanwhile, improvement of near-wellbore conductivity along the cement ring may decrease the adverse chocking effect of the flow through transverse fractures toward wellbore; some correction should be made in the total amount of proppant lost in axial fractures and near wellbore open fissures.

Multiple observations show that the typically created length of hydraulic fracture is much higher than effective propped one. For Marcellus gas shale Edwards et al. (2011) compared six months production history of 1,000ft and 500ft spaced wells and showed no production decline due to parent-child interaction even though microseismic derived X_f was

more in range of 500-1,350 ft. At the same time, obtained from RTA, X_f was only 150 ft, with 50 mD·ft of effective conductivity.

Raterman et al. (2017) showed that for multistage hydraulic fracturing with gel in lower Eagle Ford diagnostic drilling along the treated wellbore failed to identify a significant amount of proppant. Therefore, it was concluded that proppant could not be effectively transported in the multistage hydraulic fracturing for more than 120 ft. It is important to mention, however, that the coring was done 30 ft TVD above perforations of the treatment well. So proppant may be placed below the well S3.

Maity et al. (2018) reported for Hydraulic Fracture Test Site experiment that in Upper Wolfcamp in Midland Basin microseismic height of 500 ft was accompanied with only 30 ft of fracture height covered by proppant at the lateral offset of 85 feet from the treatment wellbore. Proppant was localised in sporadic areas suggesting stress or leakoff variations.

These observations contradict with general believes of long conductive fracture geometry and motivate for the development of new numerical studies to find control mechanisms of fracture propagation, proppant transport, and creation of conductivity inside the rock.

1.8. Stress shadowing

Propagation of hydraulic fracturing changes increases the minimum horizontal stress state in the proximity. Stress shadowing has a maximum value at the face of the fracture (~ P_{net}), but it also irradiates into elastic media for hundreds of feet. First analytical solution for plane strain case (L>>H) was proposed by Griffith (1924) and for penny shape fracture - by

Sneddon (1946). It was noted that penny shape crack creates less stress perturbation in the surrounding elastic media.

For vertical wells, Warpinski and Branagan (1989) suggested to use stress shadowing as a diversion tool for reorientation of hydraulic fractures on the offset wells and increase drainage of the target formation.

For the case of horizontal wells, in multicluster multistage operations, this effect makes fluid and proppant distribution unequal and prevent fractures in middle clusters from growth. With a decrease of spacing between stages and increase average size of the job, it may create an additional complication for fluid distribution and proppant placement. Several researchers over decades report strong stress shadowing effects in 2D simplified geometry (plane strain condition).

Kresse et al. (2013); Olson (2008) modeled interaction of hydraulic and natural fractures and figured out that fractures may turn from the direction of far-field maximum horizontal stress if crossing natural fractures at a favorable angle. Under assumption of uniform fluid distribution between three clusters with simplified 3D DDM method, Wu and Olson (2016) showed that for typical slickwater fracturing, outer fractures grow at angles of ~6^0 to direction of far-field maximum horizontal stress and tips of resulting fractures (H = 100 ft, Xf ~ 400 ft) are separated by extra 40 ft over cluster spacing of 50 ft. Under dynamic fluid flow distribution assumption, however, the middle fracture was almost terminated (Xf ~ 150 ft). An Implicit assumption for both cases was a constant fracture height and symmetry related to the horizontal plane.

Lecampion and Desroches (2014) pointed out that simultaneous propagation of transverse fractures generally occurs in viscosity dominated regime with less severe than in toughness dominated regime. For cluster spacing of 50ft in slick water job it was highlighted

that middle fractures are not terminated as proposed by Germanovich and Astakhov (2004); instead, they grow at a slower pace.

Instances of growing shut-in pressure (ISIP) from toe to heel stages have been recorded in multiple operations by Manchanda et al. (2012); McClure and Zoback (2013). Roussel (2017) analytically predicted stress shadowing from multiple fractures in a stage and estimated the effect of ISIP escalation from stage to stage with the primary assumption is 2D plane strain problem and vertical symmetry of fractures.

The industry consensus was that severe interference with near-wellbore (width reduction of more than 10% at the same net pressure) happens when the distance between two fractures is less than 0.5 of fracture height. From an analysis of microseismic data in Barnett Shale, Fisher et al. (2004) proposed to limit minimum spacing by 1.5 fracture height. For practical applications, it means 150 ft of cluster spacing for every 100 ft of fracture height and hence the creation of 60 fractures for 10,000 ft wellbore (assuming H=100 ft). Over the last five years, however, operators decrease cluster spacing from 60 to 15 ft, significantly increased size of the individual frac job, while still improving production rates and economics.

As it will be shown in Chapter 3 the solution of this controversy coming from taking into account asymmetrical fracture propagation in the vertical direction. By analysis of microseismic events in Utica Shale and Bakken tight sandstone formations, Dohmen et al. (2014) demonstrated that 3D nature of stress shadowing makes a basis for a 2D calculation – the assumption of reflection symmetry against horizontal plane - invalid. Series of out-off formation vertical bounces of microseismic activity, by approximate 50 - 200 ft, effectively release cumulative stress shadowing from the previous stages and allow subsequent fractures to propagate in planned fracturing zone.

An additional concern about Sneddon (1946) solution is coming from the premise of perfectly elastic (or poroelastic) media without plastic deformation, shear fracturing and related dissipation of stress shadowing. Two dimensional and many P3D and planar 3D model ignore the presence of axial fractures, capable of taking part in treating fluid and proppant and further reduce the severity of stress shadowing. The final effect of stress shadowing will be analyzed from the created model and compared with the ISIP recordings stage by stage and compared with results of Roussel (2017).

1.9. Microseismic fracturing monitoring

Microseisms are low-intensity rock movements induced by the change of stress state or liquid pressure in pores and fractures that results from the opening of hydraulic fractures and leakoff of pumped fluid. Using acoustic signal recordings (P and S waves) from geophones these events may be localized in 3D space around the wellbore with some degree of uncertainty coming from noise, unknows in velocity model and rock heterogeneity.

1.9.1. Fracture geometry

For homogeneous and poroelastic media Shapiro and Dinske (2009) proposed diffusion equation for pore pressure perturbation and introduced the concept of triggering front for a probability of the triggering of microseismic events coupling pore pressure perturbation and growth of hydraulic fracture with time. Assumed that length of the microseismic cloud has the same evolution as fracture length from PKN model Shapiro et al. (1997); Shapiro (2015); Shapiro and Dinske (2009) proposed to calculate an effective diffusivity coefficient from the

leading envelope of the microseismic cloud and, from that, to come up with an effective permeability of the unstimulated rock between an outside of hydraulic fractures.

McClure and Horne (2011), however, showed that if the pore pressure diffusion is slower than the front of shear failure, no conclusion can be made about intact rock permeability. Some of the lithologies may be aseismic due to friction strengthening behavior during the fracture slip.

Warpinski and Wolhart (2016) concluded that there is no reliable methodology to distinguish between "dry" and "wet" microseismic events in liquid-rich shale reservoirs with a non-elastic geomechanical response. Recall here that Maity et al. (2018) experimentally showed that only 30 ft of the 500 ft fracture height, inferred from microseismic, is filled with proppant ~85 ft away from the wellbore for Upper Wolfcamp formation in nearby Reagan County, Midland Basin.

Therefore, the quality of hydraulic fracture dimensions inferred only from a recorded cloud of microseismic events is questionable. At the same time, analysis of microseismic events momentum requires at least two set of geophones.

1.9.2. Moment stress inversion

Rutledge et al. (2018) published a comprehensive microseismic survey of a vertical well drilled in Midland County, TX with four monitor wells. Hydraulic fracture originated in Lower Wolfcamp (Stage 3 in **Figure 4**) was contained between two stress barriers. Meanwhile, the fracture from Stage 2 initiates from perforations in the Base Wolfcamp (TVD ~ 9,900 ft) break the upper carbonate stress barrier and causes the majority of microseismic events in the lower stress region of Lower Wolfcamp (blue bubbles). Fracture from the Stage 4 grows downward

from high-stress carbonate interval and causes microseismic events in the previous Stage 3 (bubbles colored in cyan).

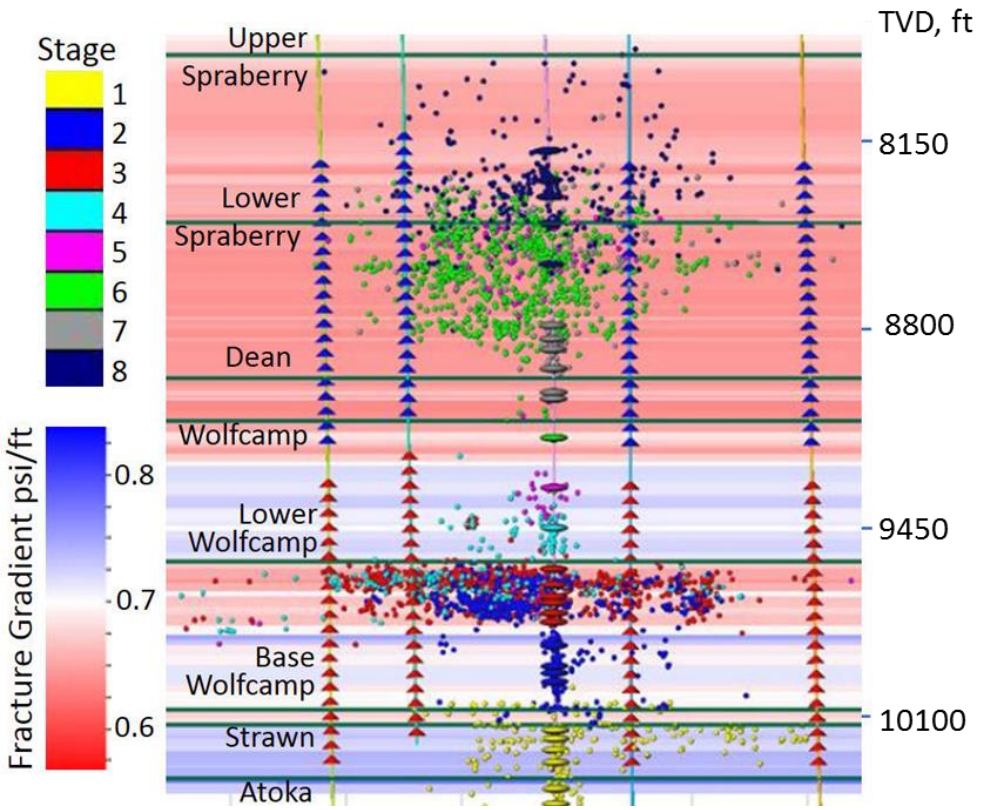

Figure 4 Treatment vertical well in Midland County, TX with four monitor wells. Reprinted with permission from Rutledge et al. (2018).

Moment tensor inversion for Stage 3 events leads to strike-slip stress environment interpretation which contradicts to normal faulting stress environment of Midland Basin in Upper Wolfcampinan/Leonardian formation accepted by Xu and Zoback (2015).

The same conclusion about stress state is published by Kuang et al. (2017) for Barnett Shale. The authors pointed out that with imperfect two monitor wells measurement configuration, relative stress anisotropy of φ=0.8, which means mixed Normal faulting/Strike-

slip stress regime (NF/SS) with high-stress anisotropy. This conclusion, however, contradicts with the general belief of low horizontal stress regime with small anisotropy of φ=0.3-0.36 in Barnett shale core area, estimated from data provided by Vermylen and Zoback (2011). Additional evidence of low-stress anisotropy in Barnett shale is the wide "fairway" stimulation mentioned by Fisher et al. (2004) and log inferred ANI=5-10% by Daniels et al. (2007).

As will be shown in Section 2.4. Wolfcamp formation also should have low-stress anisotropy and normal faulting stress regime, contrary to inferred by Snee and Zoback (2018).

As a possible solution for these contradictions, Agharazi (2016) pointed out that microseismic events close to hydraulic fracture are affected by local stress perturbation due to tip propagation and stress shadowing effects in the proximity to the fracture walls. Therefore, such events must be excluded before momentum inversion. Without such subjective procedure of selection qualified events, the microseismic inversion would provide a bias toward strike-slip and dip-slip events and, hence, critically overestimate stress anisotropy for practical modeling applications as it is demonstrated in **Table 2**, Section 2.6.2.

Recent microseismic studies of Grechka et al. (2017) for middle Bakken formation showed that microseismic anomalies which may be interpreted as propped fractures have half-length of ~65-75 ft with a reasonable height of 240-260 ft. Contrary to the conventional method of passive microseismic monitoring, this study shows a high resolution, because the authors used microseismic events as active seismic sources to highlight closed fractures in previous stages. Microseismic events from the current stage illuminated the previous stage fractures. Cracks filled by fluid produced a strong enough reflection to apply dip and azimuth attributes. Unfortunately, this type of monitoring is still too expensive and has not found its way into industry yet.

For the treatment well #46 of this study microseismic data is available, however, microseismic events were recorded from only one offset horizontal well. Therefore the microseismic dataset provides only spatial-temporal distribution of hypocentral locations with recorded magnitude ("bubble maps").

In this study, microseismic fracture images are used only as a secondary informational source for hydraulic fracturing model calibration and analysis of cyclical vertical bounces of microseismic activity against ISIP for each stage.

This dataset in the future work, however, may be reinterpreted with a semi-stochastic DFN methodology proposed by Fisher et al. (2004) and further developed by Niu et al. (2017).

1.10. Hydraulic fracturing software modeling comparison

Comparison of hydraulic fracturing simulators is a matter of constant debate over the decades. The most comprehensive comparative study conducted with GRI Staged Field Experiment (SFE) data by Warpinski et al. (1994) is continuing by American Rock Mechanics Association Technical Committee on Hydraulic Fracturing (ARMA TCHF) with more than 20 different fracturing simulators compared by 30 test cases as presented by Han (2017).
A new generation of hydraulic fracturing simulators is including explicit formulation of natural fractures and their interactions with propagating the hydraulic fracture. This formulation may lead to a better understanding of physics and provide better optimization results in comparison to an effective medium approach.

However, full 3D description of such interactions as well as initiation of fractures is still computationally prohibitive Carter et al. (2000); McClure et al. (2016). For example, a popular boundary element method (BEM) may be used to natural fractured into the model explicitly at

the cost of special gridding algorithms. For some cases of unfortunate fracture network geometry, it may create numerical instability. Therefore, a vast majority of DFN models use simplifications such as the vertical fracture network. Another problem of advanced algorithms is a requirement for detailed formation evaluation and knowledge of fractures before starting simulations.

1.11. Conclusions

The following conclusions can be made from the literature review:

1. Field observations in unconventional reservoirs showed that multiple parallel tensile fractures propagation is possible over thousands of feet from the horizontal wellbore. At the same time, it is not clear why proppant coverage is limited to hundreds of feet even for crosslinked gel formulations.
2. The complexity of physical processes and simplified models used in the industry may lead to misleading optimization, stage spacing, unfavorable proppant placement, premature near wellbore screenouts, and lower than expected production.
3. Ultralow permeability of matrix measured from GRI type tests do not correctly describe fluid leakoff. In addition to open in tensile (Mode I) fractures which initially take slurry and proppant during hydraulic fracturing, a second, pressure dependent fracture system can be identified from DFIT and falloff tests. This secondary system may be composed of intersecting shear and tensile fractures, activated by slurry leakoff.

4. Proper description and calibration of stress state inside the formation, rock mechanics model, leakoff behavior, proppant transport, and created conductivity of proppant pack is needed to history match achieved production and optimize future operations.
5. All hydraulic fracturing simulators have their pros and cons. In most cases, however, there is a balance between physics captured in the model, computation and memory cost, and practical value of better decisions.
6. Practical fracture stimulators should be capable of modeling axial (longitudinal) and transverse fractures, open secondary fissures, and realistically model proppant transport.

2. INITIAL DATA FOR MODELING*

As it was said in the previous chapter, the practical application of numerical models is limited by available data and its quality. Therefore, before deciding a particular modeling instrument, it is essential to collect and evaluate available dataset for the treatment well or the multiwell pad. It is also necessary to formulate questions for the future model and initial hypotheses. After that, an engineer may pick the right instrument.

This study demonstrates efficient workflow for data collection, analysis, and correction a horizontal well #46 (API 42-461-39156), drilled into Wolfcamp-C formation in Upton County, Midland Basin. This well is a part of a multiwell pad targeted all late Permian layers: Wolfcamp-A (WC-A), WolfCamp-B (WC-B), Wolfcamp-C (WC-C), and Wolfcamp-D (WC-D). The main advantage of vertical stacking for the selected pad is an ability to use logs from the vertical part of an offset drilled 500 ft apart (Reference well #31) to populate numerical grid for hydraulic fracturing model.

Proposed planar-3D fracture model is constructed based on publicly available data as described previously by Parsegov et al. (2018b), (2018a); Zhang et al. (2019).

* Part of the data reported in this chapter is reprinted with permission from "Physics-Driven Optimization of Drained Rock Volume for Multistage Fracturing: Field Example from the Wolfcamp Formation, Midland Basin" by Parsegov, S.G., Nandlal, K., Schechter, D.S., Weijermars, R., Proceedings of the 6th Unconventional Resources Technology Conference. Copyright 2018 by American Association of Petroleum Geologists; and from "Benefits of Engineering Fracture Design. Lessons Learned from Underperformers in the Midland Basin" by Parsegov, S.G., Niu, G., Schechter, D.S., Laprea-Bigott, M., Proceedings of the SPE Hydraulic Fracturing Technology Conference and Exhibition. Copyright 2018 by Society of Petroleum Engineers.

2.1. Description of field data

In the case study area of Upton County, the Midland Basin, the treatment well #46 targets deepwater Wolfcamp-C formation. According to Dutton et al. (2005), Wolfcamp was deposited in a tectonically quiet period of early Wolfcampian age (280-300 Ma ago).

Baumgardner et al. (2014); Hamlin and Baumgardner (2012) showed from core analysis that Wolfcamp shale is, in fact, the interplay of deepwater silica-rich mudstones and interbedded with thin layers of carbonate debris from shallow marine carbonate system of the Central Platform located southwest to the area of interest.

Wolfcamp thickens toward depocenter in the south-east part of Midland Basin. From core description (intervals: WC-C1 of 9,115-9,181 ft TVD and WC-C2 of 9,440-9,515 ft TVD) and logs interpretation for offset well Pan American Green 2 API 42383105750000 (Reagan County) it may be concluded that mudrock lithofacies has a typical thickness of 1-3 ft, whereas sandstones and carbonate-rich packstones may reach a thickness of 10 ft and more. The lower interval - Wolfcamp C2 contain more blocky clay-rich mudstones, whereas the upper interval - Wolfcamp C1 is more organic and carbonate-rich.

White et al. (2014) described stress settings in the nearby Reagan County and mentioned two vertical paleo fracture families: set J1 $N30^0$-60^0 and J2 $N310^0$-330^0 . Authors inferred maximum horizontal stress paleo direction to be NE-SW, whereas current to be W-S (from drilling induced fractures). Coherency attribute on top of Strawn formation (2,000 ft below the target Wolfcamp C) shows strike-slip paleostress regime. Similar observations were reported for two families of natural fractures in Reagan County for upper and middle Wolfcamp by Gale et al. (2018).

Treatment well #46 has 29 stages (numbers 2-30, while Stage 1 was abandoned because of mechanical issues) with 5 clusters each. Type of fracturing techniques: Plug-and-Perf.

The following dataset is available in the public database of University Lands http://www.utlands.utsystem.edu/ :

- Drilling and completion report for the Treatment well #46
- Wellbore survey for treatment well #46 and Reference well #31.
- Quadro-combo logs ASCII (LAS) files for the Reference well #31.
- Geomechanical analysis of core for well #31. Dynamic and static measurements.
- GRI permeability and porosity measurements for three offset wells

Recorded treatment pressure for each stage was used for history match hydraulic fracture model and further independent reservoir simulations showed poor drainage of rock surrounding fracture planes.

2.2. Modeling software selection

Hydraulic fracturing simulators can be divided by the type of fracture mechanics model: 2D, P3D, planar-3D, full-3D model and by numerical scheme type: FEM, BEM, finite difference, and so on as described in Section 1.3. There are also additional, less significant differences.

In general case fracture modeling software should meet the following requirements:

- Utilization of available data for the 3D geological model, honor thin fracture barriers (high stress, high modulus layers). This requirement comes from the industry scale stacking problem for pad development. Therefore, research focused models with 2D geometry for rock properties is an unacceptable simplification. This requirement limits the use of DFN based fracture models and force to apply an effective medium approach.

As it was discussed previously, pseudo-3D models are not capable of modeling multilayer propagation of isolated hydraulic fractures (with fracture barriers in the middle layers).

- Build-in correlations and meaningful defaults to avoid unnecessary assumptions. This requirement limits the choice to commercially available simulators with developed geophysical packages, a database of fluids rheology properties and a library of sands' properties.
- Ability to capture the following physical processes:
  - Stress shadowing of individual fractures in a multistage operation
  - Fracture initiation from perforation clusters, including effects of local wellbore deviation and perforation design. Ability to model longitudinal and transverse fractures explicitly.
  - Realistic proppant transport with both Newtonian and non-Newtonian fluids, the ability to capture the hybrid type of stimulations with multiple fluids and handle multiple kinds of sand during one treatment. Proppant transport in thin fluids as discussed in Section 1.6.
- The speed of calculation. Multistage hydraulic fracturing for the target well(s) should be calculated in a reasonable amount of time for a reasonably detailed grid. Optimization of design requires a large number of runs. Therefore modeling should be much faster than the treatment itself. As it was discussed in Chapter 1, modern simulators designed for explicit calculation of interaction between hydraulic fractures and natural fractures do not meet this criterion.

From this section, we can summarize that only planar-3D models are currently capable of modeling abovementioned physics with a reasonable numerical burden. The final selection between NSI Stimplan (uses FEM) and GOHFER (uses modified Boussinesq's solution) is dictated by speed advantage of GOHFER v.9.0 and better flexibility of numerical parameters for the simulation study. Similar results, however, might be obtained in any planar-3D simulator.

2.3. Perforation design

The general guideline is to have four perforations per barrel of fluid per minute Smith and Montgomery (2015). However, for the treatment well, only 40 shots were fired per stage (2 bpm per shot) without any problems with proppant placement.

Oriented perforation with 0^0 or 180^0 phasing is the most desirable perforation design to reduce treatment pressure. This conclusion is coming from the minimization of breakdown pressure discussed in more details in Section 2.4.

Unfortunately, oriented perforation is more expensive than a non-oriented one. Therefore, in oil field practice, use of 60 degrees phasing is desired to guarantee that one-third of shots are in 30 degrees error margin from the vertical direction. Length of the perforation cluster should not be more than four times the diameter of the casing to reduce the number of initiated fractures and reduce treatment pressure.

All stages we designed in the similar geometrical fashion: 5 clusters of 2 ft with four shots per feet. 3 ½ inch perf guns with 60 degrees phasing. The nominal diameter of perforations - 0.42 inch. Cluster spacing is 60 ft (Figure 5).

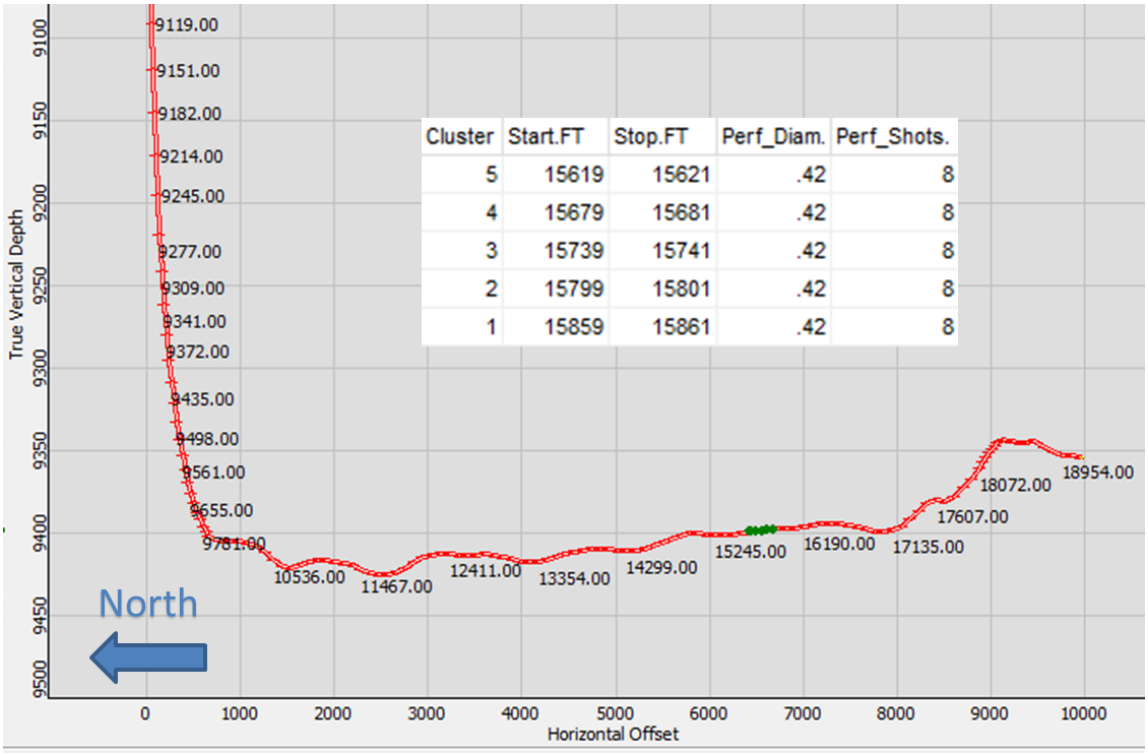

Figure 5 Wellbore trajectory (MD, TVD, and Horizontal offset from the wellhead) and perforations for Stage #9. Side view. North is to the left. Green diamonds indicate five perforation clusters. All length dimensions are in [ft].

Step rate tests show rate-dependency of pressure losses (**Figure 6**). Stages 2 and 4, for example, demonstrate some perforations-driven pressure losses, proportional to the rate squared, whereas Stage 3 demonstrates near wellbore tortuosity, proportional to square root of the rate. Overall flow capacity through perforations is adequate for the target rate of 80 bpm. The pressure at a zero pumping rate is taken equal to pad-ISIP.

From the following **Figure 6**, a step of 20 bpm (5 pressure-rate points) is not sufficient to fully describe pressure losses and find the fracture extension pressure. It is recommended to conduct step tests in smaller increments of 2-10 bpm, equivalent to pressure 100-200 psi higher than ISIP, to capture fracture extension pressure, and record transitional pressure

behavior from rate step to the next one as proposed by Smith and Montgomery (2015). Since each rate step requires about several minutes, it is recommended to have at least five data points to decouple perforation friction and near wellbore tortuosity effects.

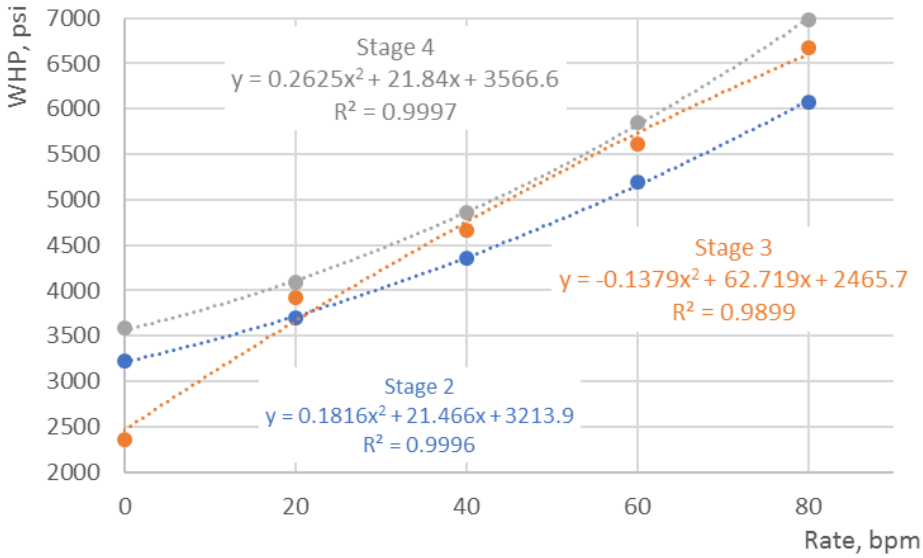

Figure 6 Step test diagnostic plot. Wellhead pressure as a function of Pumping rate for the first three stages of the treatment well.

2.4. Pumping schedule

For the treatment well (#46) the operator used a hybrid design combining slickwater pad and low viscosity linear/cross linear gel for the main treatment. For each stage, 150 gal of 15% HCl was pumped at 20 bpm to cleanup perforations and reduce near wellbore tortuosity **(Table 1)**. Then slick water pad (100,000 gals) to create fracture length, followed by gel pad and, finally, ramped up with proppant. At the end of each stage, 500 bbls (21,000 gal) of slickwater were used to flush wellbore. It should be noted that wellbore volume for the toe stages is about 18,000 gal (435 bbls), so about 3,000 gal of proppant-free slickwater were pumped into the

fracture system before closure in the toe stages and up to 12,000 gal. In Section 3.4., the adverse effect of slick water overflush will be discussed based on numerical results.

Table 1 Pumping schedule for the treatment well (#46). All stages have the similar design. The gel is linear guar equivalent to 15 lb loading, viscosity 9 cp at 80 ^{0}F. Proppant: Brady sand, 40/70 mesh.

Stage #	Elapsed Time.mm:ss	Stage Time.mm:ss	Fluid	Clean Stage Vol.GAL	Cum Clean Vol.GAL	Proppant	Slurry Conc.PPA	Cum Proppant.LB	Slurry Rate.BBL/M
1	0:00	0:00	SlickWater_120F	0.00	0.00	<None>	0.00	0.00	20.00
2	0:00	1:47	Acid_HCl_15%_100F	1500.00	1500.00	<None>	0.00	0.00	20.00
3	1:47	6:15	SlickWater_120F	21000.00	22500.00	<None>	0.00	0.00	80.00
4	8:02	23:34	SlickWater_120F	79200.00	101700.00	<None>	0.00	0.00	80.00
5	31:36	5:00	Guar_10#_120_SP_1	16800.00	118500.00	<None>	0.00	0.00	80.00
6	36:36	7:37	Guar_10#_120_SP_1	25000.02	143500.02	Brady Sand 40/70 (A)	0.50	12500.01	80.00
7	44:13	7:47	Guar_10#_120_SP_1	25000.00	168500.02	Brady Sand 40/70 (A)	1.00	37500.01	80.00
8	52:00	9:32	Guar_10#_120_SP_1	29999.99	198500.00	Brady Sand 40/70 (A)	1.50	82499.99	80.00
9	1:01:32	9:45	Guar_10#_120_SP_1	30000.00	228500.00	Brady Sand 40/70 (A)	2.00	142500.00	80.00
10	1:11:17	11:36	Guar_10#_120_SP_1	34999.99	263500.00	Brady Sand 40/70 (A)	2.50	229999.97	80.00
11	1:22:53	11:51	Guar_10#_120_SP_1	35000.00	298500.00	Brady Sand 40/70 (A)	3.00	334999.97	80.00
12	1:34:44	10:25	SlickWater_120F	17496.01	315996.00	<None>	0.00	334999.97	40.00
Total	1:45:09				315996.00			334999.97	

It should be noted that slickwater overflushing is designed at 40 bpm (50% of the maximum pumping rate). In Section 1.7 it was pointed out that according to (Kent 1959) such step-down rate overflush will be less damaging for the near wellbore fracture conductivity.

Here we can propose a further improvement of the shutdown procedure. From the standpoint of maximization of acquired information, it would be wise to add a small variation of proposed overflushing design and conduct step down test with four rates: 80, 60, 40, and 20 bpm as it was done for pad stage. In this case, extra information will be collected, the total volume of the liquid pumped will not change and adverse effects of potential Overflushing will be reduced because the last portion of slickwater will be pushed into fracture system at 20 bpm,

which is two times lower than proposed in completion design. Acquired data would be critical for after the job estimation of perforation erosion and near wellbore tortuosity.

2.5. Minimum horizontal stress estimation

From the literature review (Section 1.4.) Poisson's ratio, vertical stress, Pore pressure, and Biot poroelastic coefficient are required to estimate minimum horizontal stress as proposed by Daines (1982), assuming zero tectonic components, $S_t = 0$:

$$S_{hmin} = \frac{PR}{(1 - PR)}\left(S_v - \alpha \cdot P_p\right) + P_p$$

In this study vertical stress gradient is assumed to be 1.0 psi/ft as proposed by Friedrich and Monson (2013) for Wolfcamp formation in the Midland Basin.

It should be noted that Agharazi (2016); Xu and Zoback (2015) proposed a higher value of Sv = 1.1 psi/ft.

2.5.1. Pore pressure

Pore pressure depends on thermal maturation and geological history. For lower Wolfcamp vitrinite reflectance (Ro) is in range 1.0-1.19, indicating the oil generation window. Proprietary basin model of Loughry et al. (2015) supports that 700-1400 ft of uplift occurred in the Midland Basin since the pea of oil generation. Since kerogen is mature, evaporites of late Permian provided an excellent seal, and Wolfcamp is proven to be a source rock with a period of expulsion, overpressure is expected.

The best way to measure pore pressure is to conduct a Diagnostic Fracture Injection Test (DFIT) for each stage and to analyze after closure pressure behavior. Unfortunately, for

unconventional reservoirs, such measurements take up to several weeks. An additional complication in interpretation arises from the uncertainty of wellbore position in the lateral and created fracture geometry with a limited volume of fluid injected (usually less than 50 bbl).

Therefore, to overcome these issues operators used DFIT in vertical pilot holes for determining closure and pore pressure. Based on this data, Friedrich and Monson (2013) proposed a simple methodology of pore pressure estimation from ISIP measured during pad stage and after fracture treatment. From that analysis, the effective gradient of pore pressure in the treatment well was assumed as 0.622 psi/ft which is close to reported by Loughry et al. (2015) for Wolfcamp-C formation.

2.5.2. Biot's poroelastic coefficient

In many cases, the poroelastic coefficient is difficult to measure for unconventional reservoirs, and it is assumed to be unity as a standard industry practice. Numerous laboratory study showed that Biot's coefficient is lower than unity, which is valid for conventional coarse-grained reservoirs with high porosity.

For Barnett black shales Biot's coefficient was measured by Zhou et al. (2017), (2015). It was found for core plugs (D=1'') that Biot's coefficient decreases with an increase of effective confinement stress and generally is in range of 0.65-0.9. Much smaller Biot's coefficient in the range of 0.5-0.75 was obtained for Bakken by Havens and Batzle (2011).

For Lower Wolfcamp formation in the Delaware basin, Aderibigbe et al. (2016) came up with log differed Biot's coefficient in a range of 0.5-0.9 with lower values - 0.5 for high stressed calcite-rich layers. This study uses a power-law correlation between effective porosity and

Biot's coefficient proposed by Svatek (2017), showing similar behavior as presented in **Figure 20**.

2.5.3. Dynamic to the static conversion of rock elastic properties

Poisson's ratio and Young's modulus can be measured in static conditions on cores (triaxial test) or from sonic logs as it will be demonstrated below. Unfortunately, only 15% of drilled horizontal wells in the Midland basin have sonic logs with varying quality, and about 1% of wells have dipole sonic logs. The treatment well (#46) has no pilot hole, logs in the lateral section or core data for the target interval. Therefore, the static geomechanical model was constructed based on logs from the vertical part on nearby offset well (#31), which are also publicly available.

Traditional geophysical workflows provide an engineer with two independent elastic moduli for the target interval - Young's modulus (YM) and Poisson's ratio (PR). Calculation of YM and PR requires an open wellbore sonic log

For dynamic Poisson's ratio:

$$PR_{dyn} = \frac{1}{2} \cdot \frac{\left(\frac{V_p^2}{V_s^2}\right) - 2}{\left(\frac{V_p^2}{V_s^2}\right) - 1} = \frac{1}{2}\left(\frac{DTS^2 - 2 \cdot DTC^2}{DTS^2 - DTC^2}\right)$$

and for dynamic Young's modulus (in mln. psi)

$$YM_{dyn} = \frac{13{,}447\rho_b}{DTS^2}\left(\frac{3 \cdot DTS^2 - 4 \cdot DTC^2}{DTS^2 - DTC^2}\right)$$

Dynamic elastic properties should be converted into static ones with core calibration or regional correlations. The reason for such calibration is the fact that rock mass behaves differently at a different frequency of applied signal – acoustic dispersion.

A high frequency (~10 kHz) logging increases the apparent Young's modulus. Ultrasonic lab sources for small plugs measurements have an even higher frequency (300 kHz-1.0 MHz) and therefore requires more significant correction.

2.5.3.1. Young's modulus

Van Heerden (1987) demonstrated that dynamic Young's modulus is higher than static one up to 3 times, depends on frequency, confining pressure, density, porosity, and lithology. To compensate for this dispersion effect (in Figure 7), many researchers proposed empirical correlations for Young's modulus: Eissa and Kazi (1988); Lacy (1997); Morales and Marcinew (1993), to name a few.

For example, Eissa and Kazi (1988) provided the most general relationship (in mln. psi):

$$YM_s = 0.74 \cdot YM_d - 0.12, \text{ with } R^2 = 0.84$$

Mavko et al. (2009) provided a comprehensive list of correlations for different lithologies. Unfortunately, the development of such correlations is lagging from new drilling and completions in new formations. Therefore, there is a need for picking the best relationship for each formation type or improving one based on triaxial tests. In the absence of such data correlations between static elastic properties and "triple-combo" logs (gamma, density, and porosity) provide a better understanding of in-situ minimum horizontal stress and Young's modulus.

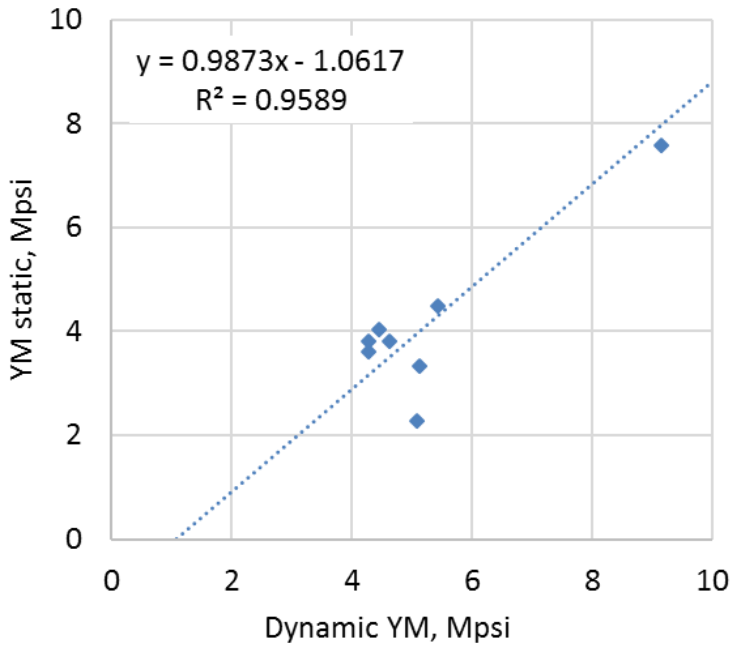

Figure 7 Correlation between Dynamic YM, measured on core samples with Static one, measured in triaxial tests for the reference well #31 and target depth interval.

Figure 8 demonstrates the measured static Young's modulus versus obtained from different correlations. Eissa and Kazi (1988) – green triangles, Van Heerden (1987) - crosses, and modified Eissa-Kazi from Barree et al. (2009) – blue diamonds. Solid line 1:1 is provided for the reference.

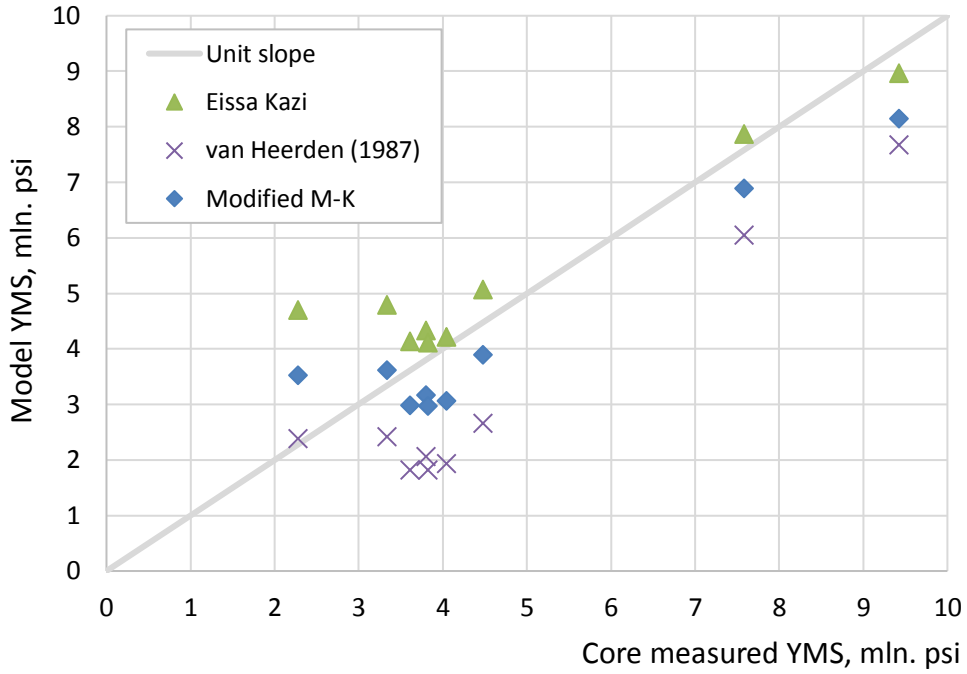

Figure 8 Comparison between Static YM measured in triaxial tests with that calculated from correlations for the reference well #31.

Modified Eissa-Kazi correlation from Barree et al. (2009) found to be the best match for the reference well #31 inside the target interval:

$$\log_{10} YM_s = \log_{10}(\rho_b \cdot YM_d) - 0.55$$

Additional to proposed modified Eissa-Kazi correlation, Mullen et al. (2007) showed that conventional petrophysical data could be used to generate pseudo sonic logs (DTC and DTS) for the Rocky Mountain region. Therefore, it is possible to populate geomechanical parameters without sonic logs if regional correlations are available.

2.5.3.2. Poisson's ratio

Dynamic Poisson's ratio measured on core samples is slightly higher than a static one (**Figure 9**), but since there is no industry-accepted correction from dynamic to static conditions for Poisson's ratio, engineers have to use dynamic Poisson's ratio without further correction.

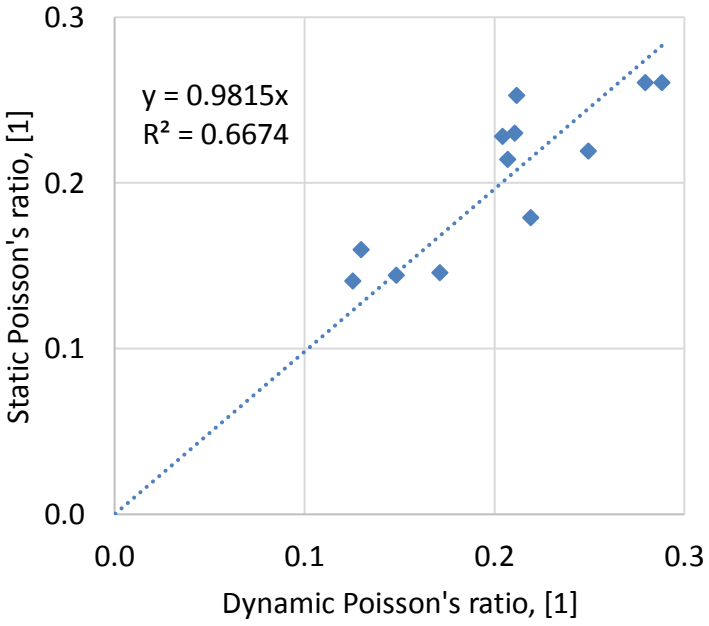

Figure 9 Dynamic Poisson's ratio measured on core samples comparing with Static Poisson's ratio, measured with triaxial tests.

Barree et al. (2009) identified multiple factors which may affect measured compressional and shear slowness – DTC and DTS. The increase in liquid saturation increases shear travel time and slightly decreases compressional travel times. It was shown that even small (5%) error in the measurement of compressional and shear slowness transfers to 20% error in Poisson's ratio and 26% in Young's modulus. Such uncertainty in Poisson's ratio leads to 26% error of minimum horizontal stress error.

From the analysis of dipole sonic logs it was found that Poisson's ratio calculated from raw DTC and DTS has an exceptionally high value of 0.32 on average (**Figure 10**, light blue curve – "PRACT" on the right track in **Figure 10**), corresponding to unusually low YM of 2.2 mln psi (light blue curve – "YMEACT" on the left track in **Figure 10**).

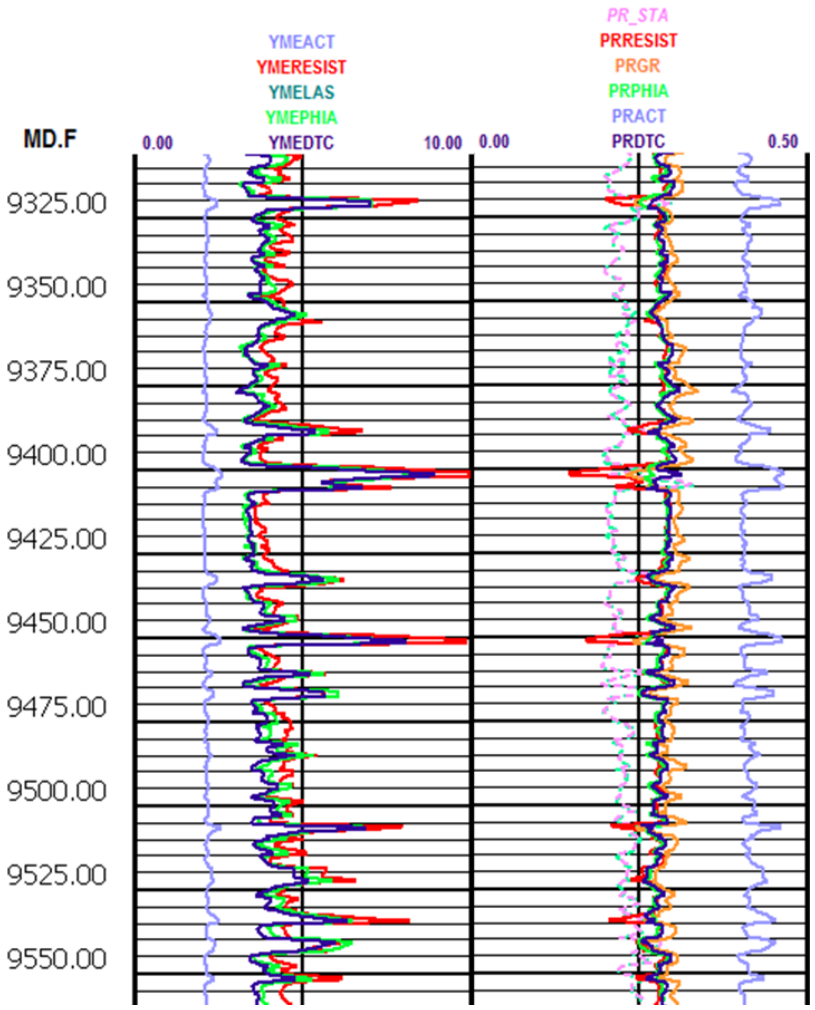

Figure 10 Calculation of YM (left track) and PR (right track) for the reference well #31. Individual curves: Actual from initial DTC and DTS; correlation from DTC log (YMEDTC and PRDTC - purple curve), gamma-ray log (PRGR – orange curve), total porosity resistivity log (YMERESIST and PRRESIST). PRSTA – stands for PR from manually corrected dipole sonic log. Correlations by Mullen et al. (2007).

At the same time, after manual slowness correction (PRSTA in **Figure 10**) values of Poisson's ratio is below 0.25 which does not match with ISIP data and literature values for S_h. Poisson's ratio spikes to the right (higher resulting stress) at the same depths as for initial interpretation discussed in Section 2.3.1. (PRACT – PR actual) for measured depth (MD) of 9,320 ft, 9,390 ft, 9,405 ft, 9,460 ft, and 9,467 ft.

For PR and YM values derived from proposed correlations are overlapping and deflect to the left at the same depth intervals. The calibration against ISIP values showing that the use of the proposed correlation is preferred.

Applicability of provided correlations and inadequate sonic log data are significant findings, because the static geomechanical model for the treatment well may be constructed without uncalibrated dipole sonic logs with the same or better accuracy. This may significantly reduce the cost of the well, without compromising predictive power of hydraulic fracturing modeling.

2.6. Estimation of horizontal stress anisotropy

Hydraulic fracture propagates in the direction of least resistance, which in the case of normal faulting regime means that vertical fracture is growing in the direction of the maximum horizontal stress. Horizontal wells are usually drilled parallel to lease boundaries. For the area of interest (NE part of Upton County) operators drill wells in North or South direction. Multiple pieces of evidence, including breakdown pressure analysis (Avasthl et al. (1991); Nolen-Hoeksema et al. (1994)), analysis of Drilling Induced Tensile Fractures (DITF) as proposed in Heidbach et al. (2016) and microseismic focal mechanism inversion by Agharazi (2016), indicate that direction of maximum horizontal stress in the area of interest is in East-West

direction. Cherian et al. (2018) proposed azimuth of maximum horizontal stress in a range of N 100-104^0.

With the absence of detectable faults and geological structures, it is safe to assume no stress direction variation from the regional trend. Since the uncertainty of the maximum horizontal stress direction is about ten degrees, therefore the azimuth of N103^0 was chosen as the best approximation as a best guess.

The second crucial parameter of stress state is a stress anisotropy – the difference between the maximum and minimum horizontal stresses, or by normalizing to the total minimum horizontal stress, as follows:

$$\mathrm{ANI} = \frac{S_H - S_h}{S_h}$$

Alternatively, the stress anisotropy may be described in equivalent terms of A_φ used in tectonophysics and microseismic analysis:

$$\mathrm{A}_\varphi = \frac{S_H - S_h}{S_V - S_h}$$

Small horizontal stress anisotropy drives the opening of the secondary fracture system, an increase of fluid leakoff, and development of complex fracture networks. High horizontal stress anisotropy, on the contrary, limits leakoff through secondary fracture system and favorite propagation of elongated fracture system with low complexity as was numerically modeled for 2D case by Olson and Taleghani (2009).

In high anisotropy stress areas in Barnett Shale FMI log has derived only transverse drilling induced fractures whereas in low anisotropy case, axial fractures have been detected as well; in high closure stress zones, no drilling induced fractures were reported by Ketter et al. (2008).

In the absence of tectonic stress and strain, sources horizontal stress anisotropy should be relatively low. Xiong et al. (2019), (2018)Agharazi (2016); Patterson (2017); Wilson et al. (2016) for Wolfcamp shale proposed anisotropy (as a fraction of minimum horizontal stress - ANI) in range of 1% to 18%. For the middle value of ANI = 8% it is equivalent to 630 psi horizontal stresses difference (at TVD = 9,310 ft).

Figure 11 demonstrates the numerical analysis of wellbore stability made in the software according to an analytical model which will be described below. The breakdown angle plot (to the left) shows the tensile fracture initiation pressure gradient as a function of the local wellbore azimuth (polar angle) and inclination (set of concentric circles ranging from 0^0 in the center for the vertical section to 90^0 for a lateral part). Black points indicate wellbore survey data points are starting from the vertical wellbore in the center and moving to horizontal wellbore drilled to south on the bottom. In the areas colored in purple fracture initiation pressure is above overburden stress (>1.0 psi/ft). Therefore in these areas initiated hydraulic fractures may be horizontal, opening bedding planes, or fracturing will start multiple shear failures.

From the breakdown angle plot, the breakdown pressure gradient is estimated at 0.86 psi/ft, compared with actual for stage 2 – P_w=0.87 psi/ft.

Drilling trajectory avoids areas of predominantly horizontal tensile failure (red and purple areas in the right plot in **Figure 11** since this stress condition is favorable for shear breakdown during the drilling.

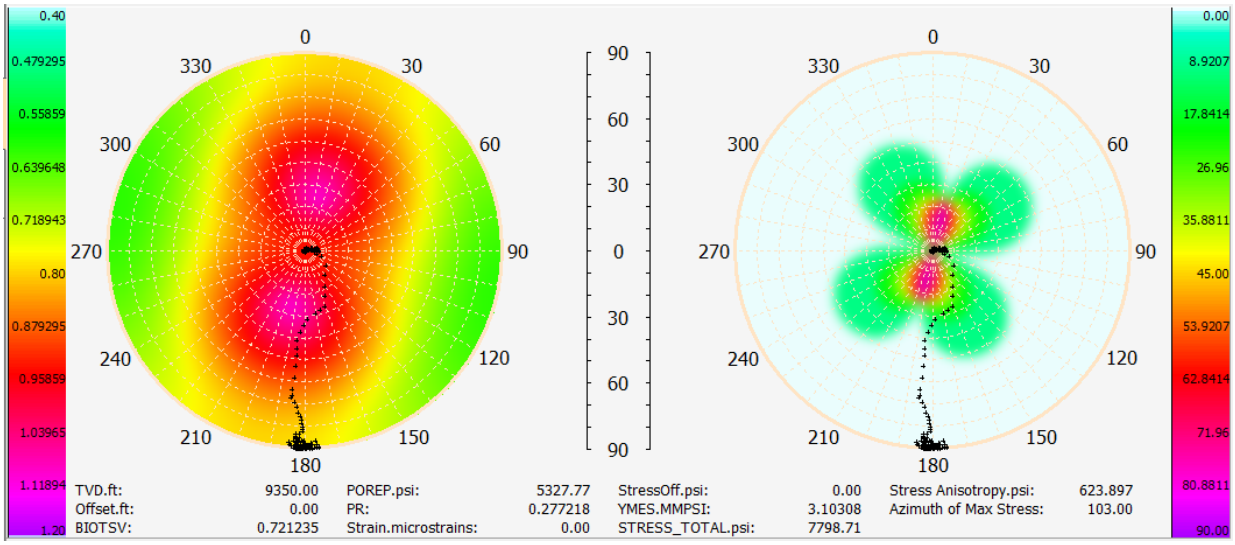

Figure 11. Wellbore stability analysis for the treatment well #46H with ANI = 8%.

So chosen stress anisotropy and azimuth of the maximum horizontal stress result in consistent observations of measured breakdown pressure and optimal well trajectory as provided in drilling and completion data for the treatment well.

2.6.1. Literature stress anisotropy data

Surprisingly, Snee and Zoback (2018) provided a much higher estimate of horizontal stress anisotropy and inferred mixed Normal faulting – Strike-Slip stress regime for the area of interest (**Table 2** and **Figure 12**).

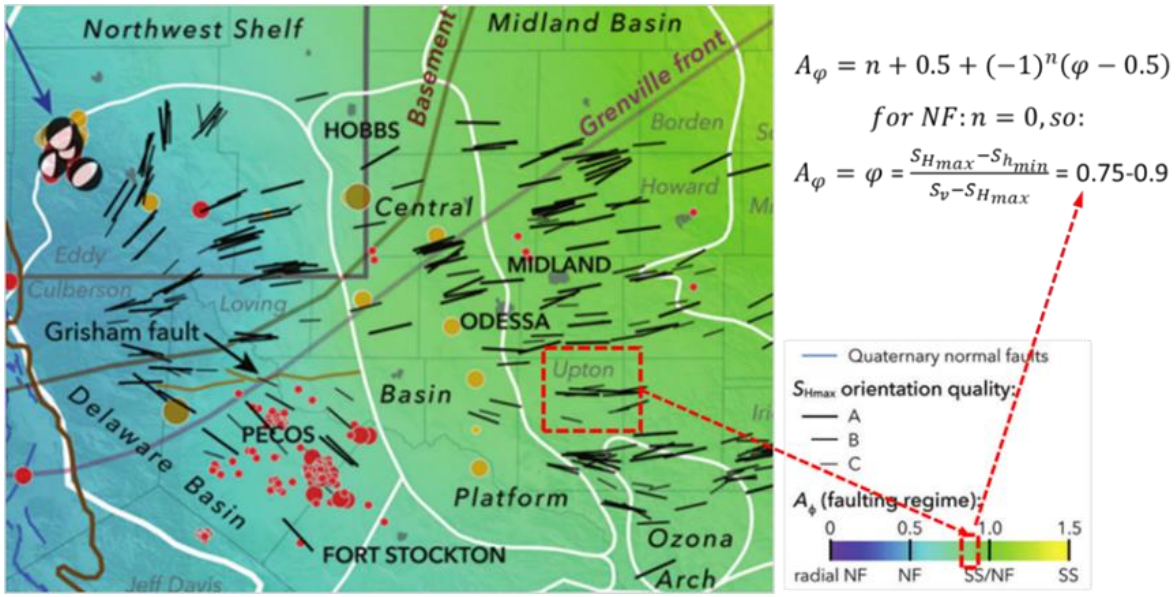

Figure 12 Proposed stress state in the area of interest. Black solid lines show the direction of the maximum horizontal stress, color-coded map – stress regime in A_φ notation defined by Simpson (1997). Reprinted with permission from Snee and Zoback (2018).

Table 2 Stress anisotropy in the area of interest. Location of the treatment well (#46H) is Lat: 31.266, Lon: -101.787. Reprinted with permission from Snee and Zoback (2018).

Lat_WGS84	Lon_WGS84	A_φ	Data_type	Source
31.96	-106.22	0.5	Geologic	Ricketts et al. (2014)
31.83	-103.12	1	Interpreted visually from focal mechanism(s)	Doser et al. (1991)
31.55	-101.94	0.9	In situ	Snee and Zoback (2018)
31.5	-101.8	0.8	Formal focal mechanism inversion	Snee and Zoback (2018)
31.14	-101.19	0.822	In situ	Xu and Zoback (2015)

For Aφ in the range of 0.75 – 0.9 and assumed Sv = 1.0 psi/ft, for TVD=9350 ft and $S_h =$ 0.83 psi/ft stress, ANI would be in the range from 37% to 50%. From that, with similar calculations, we can infer that horizontal wellbore drilled in the South direction will have a fracture gradient higher than overburden ($S_V = 1.0$ psi/ft). This local wellbore stress condition will lead to the propagation of horizontal hydraulic fractures near the wellbore for all Stages **(Figure 13**).

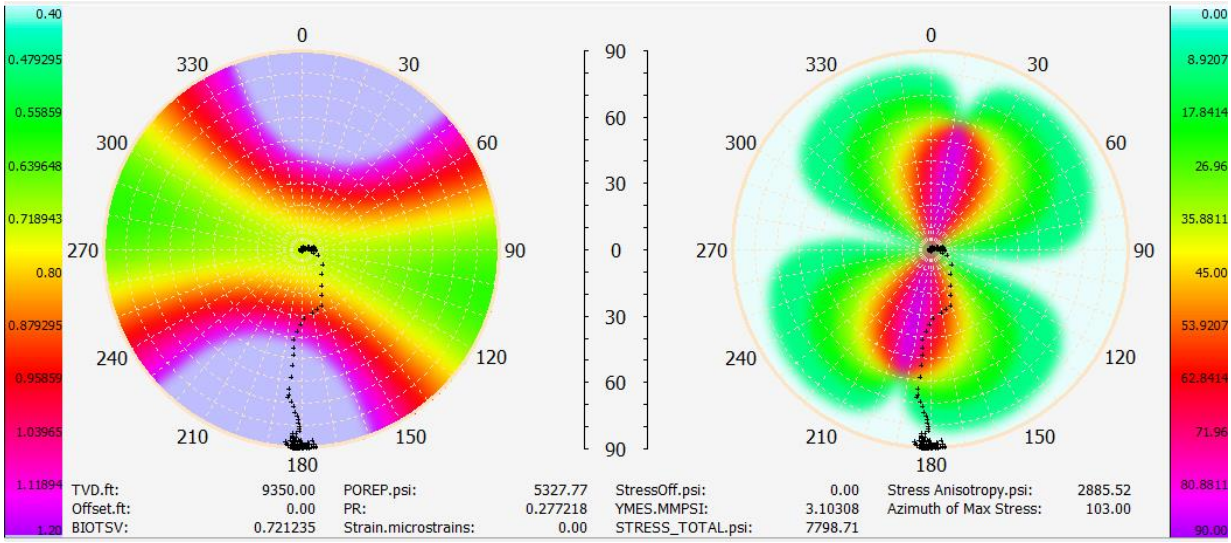

Figure 13 Wellbore stability diagram for A_φ=0.8 (ANI = 37%). From the left diagram, the breakdown pressure gradient is higher than 1.2 psi/ft (a gray area), which implies preferable propagation of horizontal fractures near the wellbore.

It should be noted that for Barnett shale, known for its low stress anisotropy (ANI) below 19-27% from tensile fracture opening modeling by (Vermylen and Zoback (2011)), Kuang et al. (2017) from inversion of microseismic moment tensor with two monitor wells concluded that Barnett shale (TVD = 6,300 ft) has higher anisotropy of A_φ=0.81 (ANI = 33%).

From these two examples for Barnett shale and Wolfcamp formation in Midland Basin, a gap in knowledge of horizontal stress anisotropy is identified. In addition to that, there is a significant difference in stress anisotropy reported from breakdown pressure data and inversion of microseismic moment tensor, sometimes drastically different stress anisotropy estimations reported by the same authors. Therefore, this contradiction should be resolved before the physics-driven model of fracture propagation may be proposed.

2.6.2. Estimation of stress anisotropy

In order to resolve the contradiction between literature data for horizontal stress anisotropy, an analytical stress model is proposed for estimation of the upper limit of breakdown pressure for the treatment well #46.

In multiple publications, researchers used formation breakdown pressure in inclined wells as a diagnostic tool to back-calculate far-field stress state. Kirsch (1898) proposed a solution for a 2D case which may be extended for the 3D case. Constant far-field stresses are used as a boundary condition. At the same time, conversion from vertical to principal horizontal stresses via uniaxial Poisson's ratio assumes zero lateral strain.

Rotation of stresses from the far-field to local wellbore coordinates may is given by:

$$\begin{matrix}\sigma_{xx}\\ \sigma_{yy}\\ \sigma_{zz}\\ \tau_{yz}\\ \tau_{xz}\\ \tau_{xy}\end{matrix} = \begin{bmatrix} 0 & sin^2\beta & cos^2\beta \\ sin^2\alpha & cos^2\beta \cdot cos^2\alpha & cos^2\beta \cdot sin^2\alpha \\ cos^2\alpha & sin^2\alpha \cdot cos^2\beta & sin^2\alpha \cdot sin^2\beta \\ -\sin\alpha \cdot \cos\alpha & \sin\alpha \cdot \cos\alpha \cdot cos^2\beta & \sin\alpha \cdot \cos\alpha \cdot sin^2\beta \\ 0 & -sin\beta \cdot \cos\beta \cdot sin\,\alpha & \sin\beta \cdot \cos\beta \cdot \sin\alpha \\ 0 & -sin\beta \cdot \cos\alpha \cdot \cos\beta & \sin\beta \cdot \cos\alpha \cdot \cos\beta \end{bmatrix} \begin{bmatrix} S_v \\ S_H \\ S_h \end{bmatrix}$$

where:

$S_H = (1 + ANI) \cdot S_h$ - total maximum horizontal stress

α - well diviation angle from the vertical direction

β - angle between the projection of the wellbore to horizontal plane and direction of S_H, for the case of the treatment well is 77^0.

For horizontal wellbore ($\alpha = 90^0$):

$$\begin{bmatrix} \sigma_{xx} \\ \sigma_{yy} \\ \sigma_{zz} \\ \tau_{yz} \\ \tau_{xz} \\ \tau_{xy} \end{bmatrix} = \begin{bmatrix} 0 & sin^2\beta & cos^2\beta \\ 1 & 0 & cos^2\beta \\ 0 & cos^2\beta & sin^2\beta \\ 0 & 0 & 0 \\ 0 & -sin\beta \cdot \cos\beta & \sin\beta \cdot \cos\beta \\ 0 & 0 & 0 \end{bmatrix} \begin{bmatrix} S_v \\ S_H \\ S_h \end{bmatrix}$$

Let θ – a polar coordinate, around the wellbore, so $\theta = 0^0$ corresponds to the top of the well and $\theta = 180^0$ corresponds to the bottom of the well.

In cylindrical coordinates at the wellbore wall, according to Bradley (1979), assuming nonpenetrating fluid, radial stress at the borehole wall (compressional possitive): $\sigma_r = P_w$

Tangential well stress: $\sigma_\theta = \sigma_{xx} + \sigma_{yy} - 2(\sigma_{xx} - \sigma_{yy}) \cos 2\theta - 4\tau_{xz} \sin 2\theta - P_w$

Axial well stress: $\sigma_z = \sigma_{zz} - 2 \cdot PR \cdot (\sigma_{xx} - \sigma_{yy}) - 4 \cdot PR \cdot \tau_{xy} \cdot \sin 2\theta$

Barree and Miskimins (2015) in their Eq. 16 and 17 show the similar to the provided above solution, and it contains a shear component.

Note, however, that contrary to the approach in Barree and Miskimins (2015); Roundtree et al. (2009) all stresses in the above formula should be total, not effective ones. While keeping total stresses in derivation, we keep ANI in calculations and avoid confusion with pore pressure deduction for effective stress calculation, first introduced by Daneshy (1973) and corrected by Bradley (1979) for a non-penetrating fluid case. Therefore, in Eq. 16 of Barree and Miskimins (2015) and Eq.A.12 of Roundtree et al. (2009) must be in total stress terms.

Minimum total principal normal stresses should be compared with the fluid pressure in the wellbore plus some tensile strength. In order to do that provided calculations should be continued with additional stress rotation to eliminate the shear component as follows.

There is a direction of principal stress which minimizes one of normal components and eliminates the shear one. Because of misalignment between well azimuth and the direction of minimum horizontal stress $\beta \neq 90^0$, the shear component is given by:

$$\tau_{\theta z} = 2\left(-\tau_{yz}\sin\theta + \tau_{xz}\cos\theta\right)$$

Since the fluids do not support shear stress, shear components should be the same for both effective and total notations. So stress tensor:

$$\sigma = \begin{bmatrix} \sigma_r & 0 & 0 \\ 0 & \sigma_\theta & \tau_{\theta z} \\ 0 & \tau_{\theta z} & \sigma_z \end{bmatrix}$$

may be rotated from the wellbore axis for the angle to eliminate shear component and find principal stresses orientation:

$$\gamma = \frac{1}{2}\arctan\left(\frac{2\cdot\tau_{\theta z}}{\sigma_\theta - \sigma_z}\right)$$

A non-zero value of this angle is significant because it analytically predicts growing of multiple parallel longitudinal fractures even for horizontal wellbore from each broken perforation before the increase of pressure open parallel transverse fractures at the complementary angle.

It also may be a key to explain the initiation of transverse fracture swarms. This local stress regime can be an explanation of observed fracture swarms by coring experiments of Raterman et al. (2017) described in Section 1.2. For nonhorizontal well $\alpha \neq 90^0$, the fracture swarm at initiation will be inclined.

To get components of effective principal stresses at the wall of the wellbore by Daneshy (1973):

$$\sigma'_1 = \mathrm{P}_w - P_p$$

$$\sigma'_2 = \frac{1}{2}\left(\sigma_\theta + \sigma_z + \sqrt{(\sigma_\theta - \sigma_z)^2 + 4\tau_{\theta z}^2}\right) - P_p$$

$$\sigma'_3 = \frac{1}{2}\left(\sigma_\theta + \sigma_z - \sqrt{(\sigma_\theta - \sigma_z)^2 + 4\tau_{\theta z}^2}\right) - P_p$$

Rocks will fail in tensile at: $\sigma'_3 + T = 0$, where T – tensile strenght of the rock which is generally neglible. For estimation of the upper limit of horizontal stress anisotropy, we can postulate zero value of the shear component $\tau_{\theta z} = 0$: $\beta = 90^0$ (wellbore is drilled along minimum horizontal stress), $T = 0$ psi (zero tensile strenght), $\theta = 0^0$ (top of the wellbore).

Minimum effective principle stress component σ'_3 simplifies at tensile failure as:

$$\sigma'_3 = \frac{1}{2}\left(\sigma_\theta + \sigma_z - \sqrt{(\sigma_\theta - \sigma_z)^2}\right) - P_p < 0$$

$$\sigma_\theta = \sigma_{xx} + \sigma_{yy} - 2\left(\sigma_{xx} - \sigma_{yy}\right) = 3S_V - S_h(1 + ANI) - P_w$$

$$\sigma_z = S_h - 2PR(S_h(1 + ANI) - S_V)$$

Knowing from Section 2.3.:

$$S_h = 0.834\ psi/ft$$

$$S_V = 1.0\ psi/ft$$

Finally, by taking observed breaking pressure from the completion report, downhole P_w= 0.87 psi/ft, we can solve the abovestated system and get:

$$\text{ANI} < 11\%$$

For the treatment well #46, $\beta = 77^0$ and ANI should be lower than 11% (or 862 psi in absolute terms). Therefore, ANI = 11% may be stated as an upper limit of horizontal stress anisotropy estimation.

For the lower limit estimation, Roussel (2017) proposed an independent way from ISIP escalation curves:

$$\Delta\sigma_{plateau} < S_H - S_h = ANI \cdot S_h$$

In other words, according to Roussel (2017), the difference between the plateau of ISIP curve and ISIP for the first stages, should not be higher than the difference of maximum and minimum horizontal stresses. Additionally, it should be stated that this method assumes that the apparent fracture toughness (including all fracture propagation tip and process zone effects) is the same and all fractures are staying in the target zone without breaking stress barriers. If stress barriers have lower stress difference than principal horizontal stresses, the ISIP curve should exhibit multiple buildups, signaling of stages breaking the upper or lower stress barriers.

It is worth noting that for Barnett Shale in Fort Worth Basin Vermylen and Zoback (2011) estimated small horizontal stress anisotropy with S_h = 0.63 − 0.67 psi/ft and S_H<0.8 psi/ft (A_φ = 0.3-0.36) with recoreded ISIP escalation as 1200 psi for simultaneous fracturing of two offset wells and only 600 psi for zip fracturing of other two offset wells. With typical for

Banett shale TVD = 7,400 ft, $\Delta S = (S_H - S_h)$, is in range of 962 to 1,258 psi, which is in good agreement with the abovementioned method for estimation of the lower boundary of horizontal stress anisotropy.

For the treatment well #46 from recorded ISIP in **Figure 27**, Section 2.6.2.: $\Delta\sigma_{plateau} \sim 600$ psi, and estimation of $ANI > 7.6\%$, so the anisotropy may be estimated in the range of 7.6% to 11%. Therefore, $ANI = 8\%$ is a reasonable assumption for the proposed hydraulthe ic fracturing model.

2.6.3. Discussion

Proposed breakdown analysis may be a useful instrument to constrain the value of maximum horizontal stress from formation breakdown and step test data. Therefore, it is recommended to check the feasibility of proposed horizontal stress anisotropy against measured fracture gradient, wellbore inclination, vertical and minimum horizontal stress values as well as implied pore pressure. This simple user entry check allows avoiding overestimation of breakdown pressure, ISIP, and closure pressure during simulation.

One possible explanation of the discrepancy between the World Stress Map project and abovementioned model for horizontal stress anisotropy may be the focus of Snee and Zoback (2018) on stress regime in brittle formations of the basement at 15,000 ft TVD. Because data points with A_φ>0.5 in **Table 2** are taken from inversion of microseismic focal mechanism inversion after hydraulic fracturing in clay-rich mudstones, including Wolfcamp formation, this explanation is discounted.

From that discussion, we can conclude that Wolfcamp-C formation should have Normal Faulting (NF) far-field stress regime with small horizontal stress anisotropy, close to “radial

NF" and stress state proposed by Snee and Zoback (2018) should be rejected for hydraulic fracturing modeling.

Additionally, on the other end of extremely low estimations of horizontal stress anisotropy, Xiong et al. (2018) estimated ANI=1% from history matching of hydraulic fracturing treatment pressure.

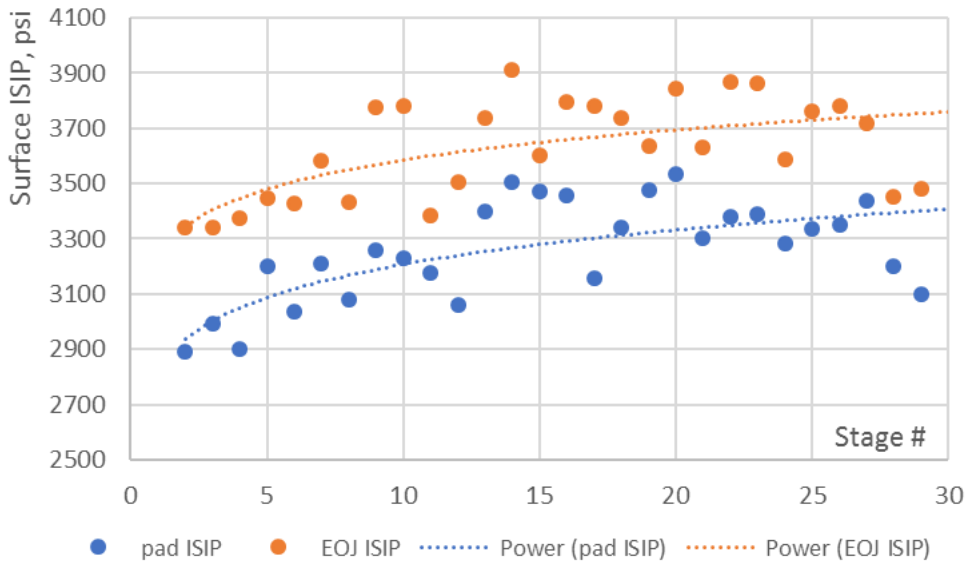

Figure 14 Recorded pad ISIP and EOJ ISIP for well 4H modeled by Xiong et al. (2019). Source: Drilling and completion report for well 4H from the University Lands website.

Following the same procedure, for data presented by Xiong et al. (2018) and Xiong et al. (2019), the difference between plateau of the pad and EOJ ISIP as well as from escalation of the treatment pressure is about 500 psi. Hence, ANI should be not less than 6.8% for Wolfcamp-B formation, assuming S_h = 7270 psi for TVD = 6950 ft from **Figure 20.**

2.7. Estimation formation permeability

Formation permeability is one of the primary controls for fracturing fluid leakoff during pumping. Since direct measurement of permeability in extremely low permeability formations is a challenging task, several methods were proposed to estimate permeability indirectly.

2.7.1. Matrix permeability (GRI methodology)

Traditional steady-state core-flood experiments are not helpful for permeability measurement of ULP formation due to the required high-pressure drop for measurable rates and significant time for achieving a steady state. Two transient methods exist to avoid these drawbacks: pulse decay on confined core pugs proposed by Jones (1997) and pressure decay on crushed rock samples - by Luffel et al. (1993).

Figure 15 demonstrates an example of effective porosity – Gas Research Institute (GRI) permeability for offset wells and rock samples with similar lithology. Rock samples were crushed and sewed at 20/35 mesh and treated in Dean-Stark apparatus, then dried at 110 °C/230°F. For a typical target interval porosity of 6-7% permeability is in order of 20-200 nD.

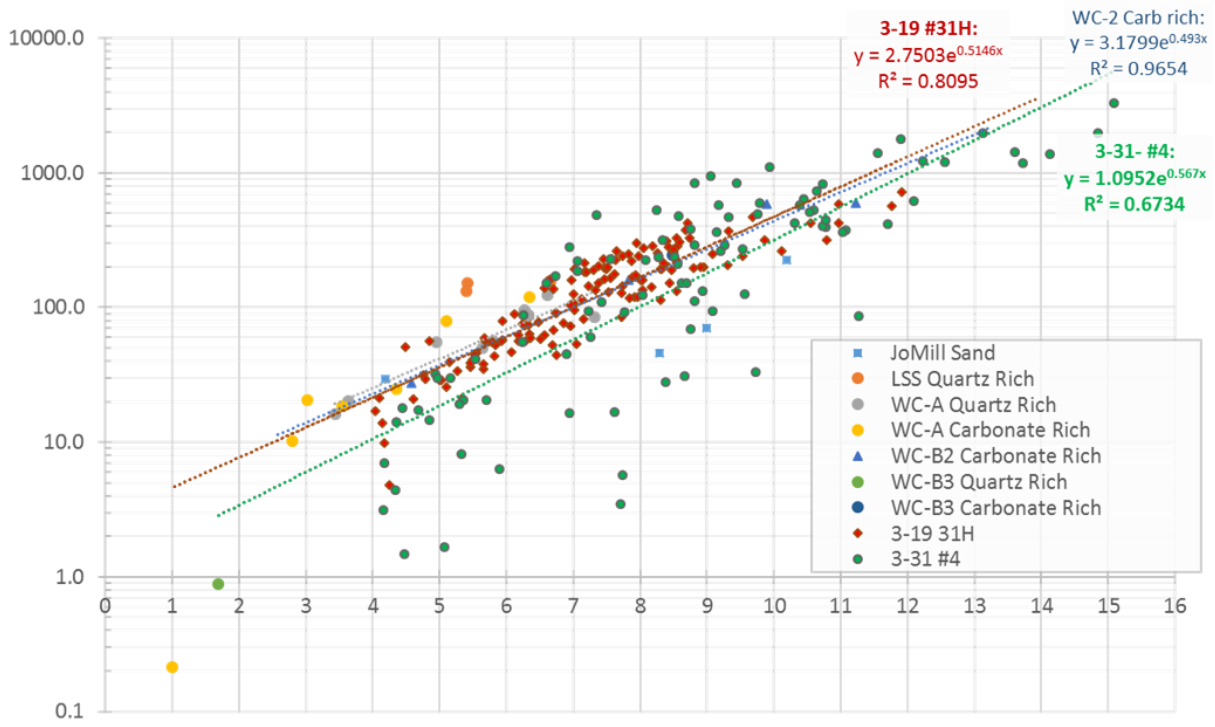

Figure 15 GRI gas permeability vs. total porosity for offset wells. Dean Stark extracted samples (20/35 mesh size) dried at 110 °C. Effective porosity is interconnected pore space. Reprinted from Parsegov et al. (2018a) with permission from URTeC, whose permission is required for further use.

For the reference well #31 after filtering out core samples with effective porosity lower than 4% (**Figure 16**), the following general formula for the matrix permeability is proposed from analysis of the log-log plot:

$$k = k_{mult} PHIE^{k_{exp}} = 2.152 \cdot PHIE^{2.152}$$

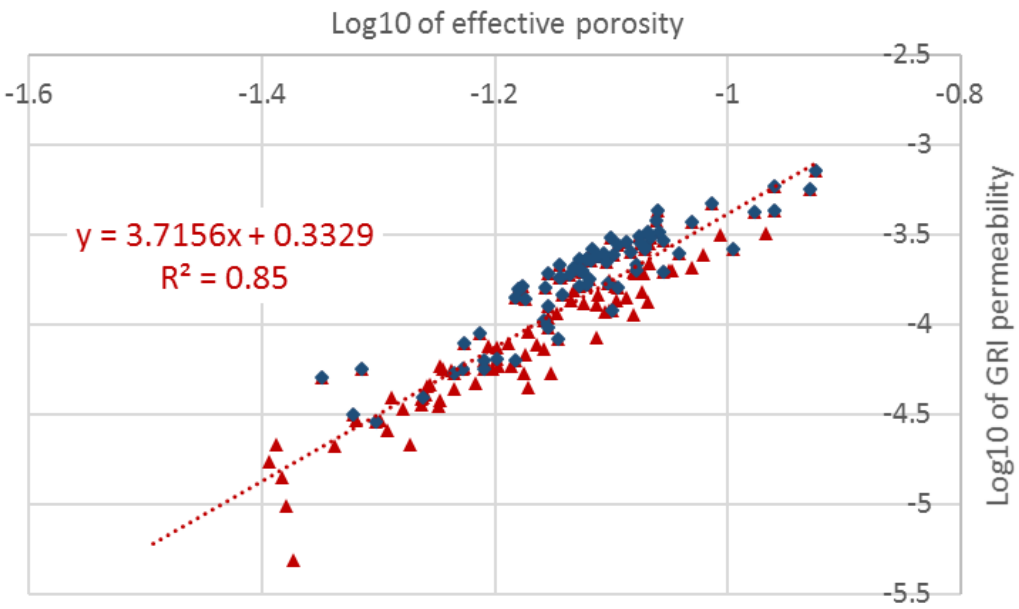

Figure 16 GRI gas permeability vs. effective porosity in Log-Log plot for the reference well #31. For permeability, [mD]: $k_{exp} = 3.7156$ and $k_{mult} = 10^{0.3329} = 2.152$.

2.7.2. Digital rock methodology

Novel high-resolution microscopy may be used for evaluation of pore size distribution and create a 3D volume of connected pore space. Walls and Foster (2017); Walls and Morcote-Rios (2015) used 3D FIB-SEM to reconstruct pore volume from 2D SEM images for eight core samples, mainly from Wolfcamp formation. Horizontal permeability was calculated with the modified Lattice-Boltzmann method described by Tölke et al. (2010). Authors found two distinct series of permeability-porosity trends for low and high porosity interconnection.

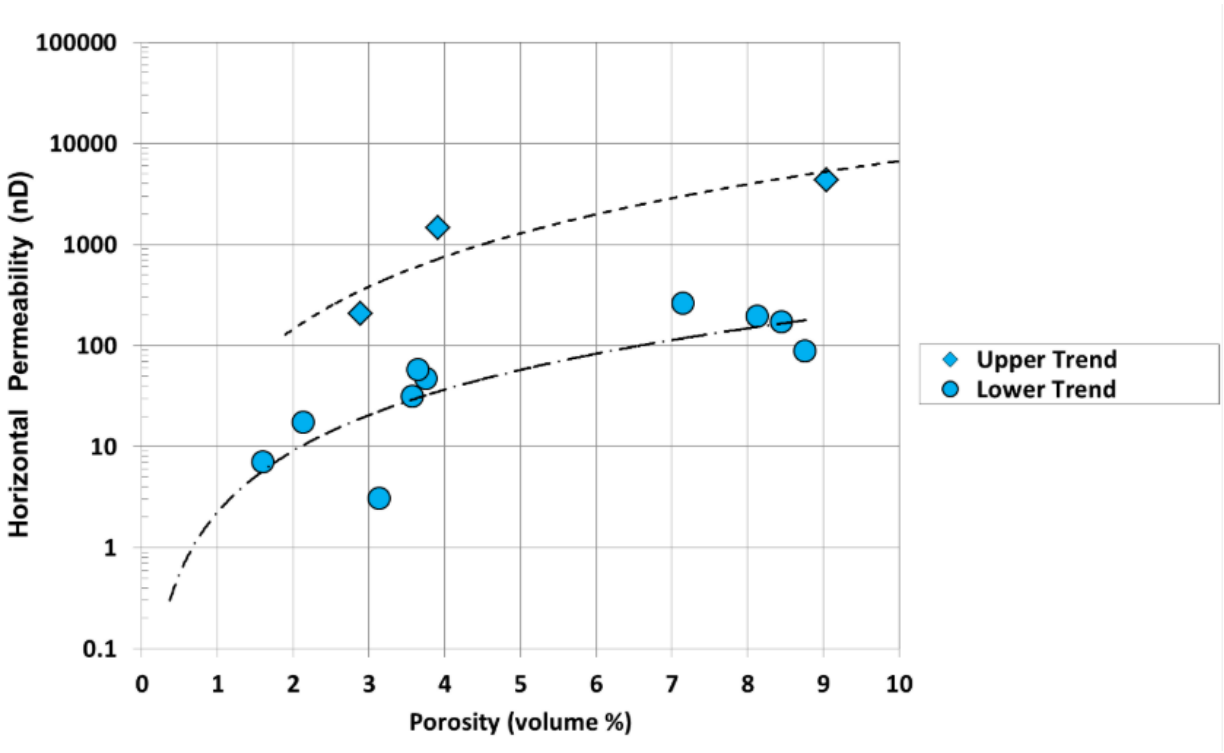

Figure 17 Correlation of numerical calculated horizontal permeability with total porosity for Wolfcamp formation in the southern part of the Midland Basin. Reprinted with permission from Walls and Foster (2017).

It is worth to mention that straight line in the semilog plot in **Figure 17** is breaking down at low porosity values. Therefore, the use of 4% effective porosity cutoff in **Figure 15** is independently justified. The proposed correlation for this study is in range calculated by Walls and Foster (2017) and close to the lower trend.

2.7.3. DFIT method

Figure 18 presented previously unpublished data by Craig et al. (2019) reports the broad statistical distribution of permeabilities than presented in Sections 2.7.1. and 2.7.2. for Wolfcamp formation. From the interpretation of DFIT data, measured permeabilities for

multiple wells have a lognormal distribution with P_{10} = 260 nD, P_{90} = 8,000 nD. About 40% of data points belong to the region of <1 µm.

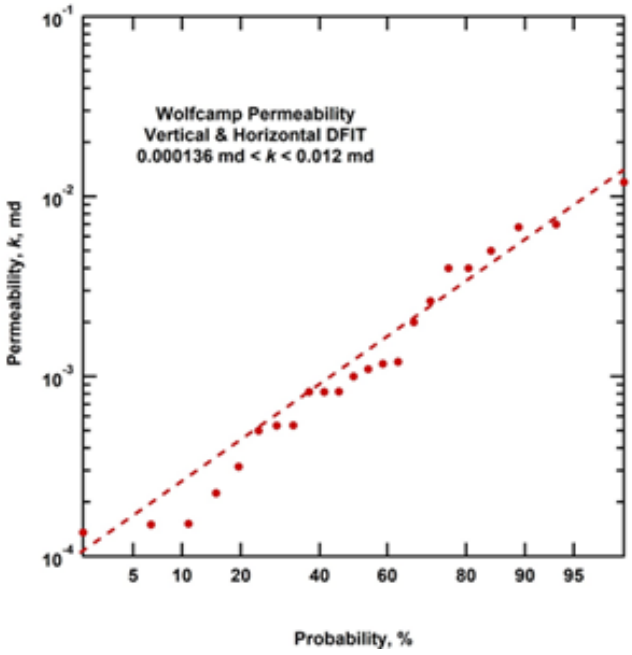

Figure 18 Wolfcamp permeability distribution from DFIT interpretation in vertical and horizontal wellbores. Reprinted from Craig et al. (2019) with permission.

2.8. Leakoff model

A formula for the region of investigation (in field units) for linear flow at constant wellbore pressure was proposed by Wattenbarger et al. (1998) as follows:

$$y_{inv} = 0.159\sqrt{\frac{kt}{\mu c_t \varphi}}$$

Assuming:

$$k = 0.2\ [\mu D]$$

$$\mu = 1.1\ [cP]$$

$$c_t = 10^{-5}[psi^{-1}],$$

$y_{inv} = 30\ ft$ (half-distance between clusters)

it gives:

$$t = \frac{39.5\mu c_t \varphi}{k} {y_{inv}}^2 = \frac{39.5 \cdot 1.1 \cdot 10^{-5} \cdot 0.06}{0.2 \cdot 10^{-3}} 30^2 = 117\ [days]$$

It means that for a typical liquid-rich shale play boundary dominated flow is achievable during the first year of production. For uncompressible one dimensional, one phase fluid flow under a steady-state condition in field units Craft et al. (1991):

$$q_L\ [STB/day] = 0.001127 \frac{k\ [mD] \cdot A[ft^2]}{\mu\ [cP]} \frac{1}{FVF\left[\frac{STB}{RB}\right]} \frac{\partial P}{\partial x}\ [psi/ft]$$

For a typical unconventional well we may assume:

$FVF = 1.1\ [STB/RB]$

$A = 2 \cdot N_{stages} N_{clusters} H_f \cdot 2X_f = 2 \cdot 30 \cdot 5 \cdot 2 \cdot 100 \cdot 100 = 6 \cdot 10^6\ [ft^2]$

$q = 500\ [STB/day]$ (at boundary dominated flow)

$$\frac{\partial P}{\partial x} = \frac{qB}{A} \frac{1}{0.001127} \frac{\mu}{k} = \frac{500 \cdot 1.1}{6 \cdot 10^6} \frac{1}{0.001127} \frac{1.1}{2 \cdot 10^{-4}} \sim 900\ [psi/ft]$$

Which gives unrealistic pressure drop (ΔP) of 27,000 psi over half distance between clusters. This demonstration shows that real unconventional reservoir has enhanced permeabilty region after hydraulic fracturing stimulation. Alternatively, this system may be described by a DFN model or by use of a dual porosity system for production modeling after hydraulic fracturing.

Empirical leakoff model in GOHFER consists of matrix leakoff through exposed fracture face and pressure dependent leakoff through dilated secondary fractures. To adequately describe such combined leakoff model one needs to know Critical Fissure Opening Pressure

(CFOP) and Pressure Dependent Leakoff coefficient, so total leakoff may be estimated for each grid block as follows:

$$C_p = C_0 \exp(P_f - CFOP - S_h)$$

2.8.1. Critical Fissure Opening pressure (CFOP)

Nolte and Smith (1981) concluded that pressure required for tensile opening of the vertical fissure, crossing hydraulic fracture at arbitrary angle θ, does not depend on that angle. As it was mentioned that shear failure is the source of microseismic events and shear failure may occur at net pressures below required for tensile opening of natural fractures. In order to investigate conditions of such shear failure, the 2-D coordinate transform of stresses is required. For the local stress along the wall of the hydraulic fracture in the middle height region, rotation to the angle θ:

$$\begin{bmatrix} \sigma_{xx} & \tau_{xy} \\ \tau_{xy} & \sigma_{yy} \end{bmatrix}_{new} = [Q] \begin{bmatrix} \sigma_{xx} & \tau_{xy} \\ \tau_{xy} & \sigma_{yy} \end{bmatrix} [Q]^T$$

Where Q – is a rotation matrix:

$$Q = \begin{bmatrix} \cos\theta & \sin\theta \\ -\sin\theta & \cos\theta \end{bmatrix}$$

$$\begin{bmatrix} \sigma_n & \tau \\ \tau & 0 \end{bmatrix} = \begin{bmatrix} \cos\theta & \sin\theta \\ -\sin\theta & \cos\theta \end{bmatrix} \begin{bmatrix} S_H + 2 \cdot PR \cdot P_{net} & 0 \\ 0 & S_h + P_{net} \end{bmatrix} \begin{bmatrix} \cos\theta & -\sin\theta \\ \sin\theta & \cos\theta \end{bmatrix}$$

$$\sigma_n = (S_h + P_{net})cos^2\theta + (2 \cdot PR \cdot P_{net} + S_H)sin^2\theta$$

$$\tau = \big((2 \cdot PR \cdot P_{net} + S_H) - (S_h + P_{net})\big) \sin\theta \cos\theta$$

Because by convention positive stress means compression, the tensile failure criterion is the negative value of effective normal stress:

$$\sigma'_n = \sigma_n - P_f = \sigma_n - (S_h + P_{net})$$

$$= (S_h + P_{net})cos^2\theta + (2 \cdot PR \cdot P_{net} + S_H)sin^2\theta - (S_h + P_{net})$$

$$= sin^2\theta\big((2 \cdot PR \cdot P_{net} + S_H) - (S_h + P_{net})\big) < 0$$

$$P_{net} > \frac{S_H - S_h}{1 - 2 \cdot PR} = \frac{ANI \cdot S_h}{1 - 2 \cdot PR}$$

Exactly is proposed by Nolte and Smith (1981). Note, however, that the value of normal effective stress depends on the angle θ, contrary to stated in the paper. In the direction close to parallel to the hydraulic fracture, normal effective stess will be small regardless of the value of $P_{net} > 0$ in the modeled case. For abovementioned conditions for the treatment well #46:

$$P_{net} > \frac{ANI \cdot S_h}{1 - 2 \cdot PR} = \frac{0.08 \cdot 7{,}800\ psi}{1 - 2 \cdot 0.277} = 1{,}400\ psi$$

$$CFOP = 1{,}400\ psi$$

It is worth to mention that according to Nolte and Smith (1981) the treatment pressure required to open fissures:

$$P_f = S_h + CFOP = 7{,}800 + 1{,}400 = 9{,}200\ psi$$

is higher than maximum horizontal stress (8,424 psi) and comparable to total vertical stress of 9350 psi. For higher horizontal stress anisotropy, say ANI = 11% as is the highest estimation in Section 2.4., $P_f = S_h + CFOP = 7{,}800\ psi + 1{,}920\ psi = 9{,}720\ psi$, which is higher than overburden. Therefore, according to Nolte and Smith (1981) at moderate stress anisotropy, it is impossible to open fissures in tensile (mode I) without forming T-shape fractures along bedding planes.

Assuming cohesionless closed natural fracture, the frictional law applies, and shear failure condition can be stated as follows:

$$\tau > \mu \cdot \sigma'_n$$

Collecting similar group in the and the left and right parts of inequality, for mechanically closed fracture:

$$P_{net} < \frac{S_H - S_h}{1 - 2 \cdot PR}$$

$$\cancel{\left((2\ PR \cdot P_{net} + S_H) - (S_h + P_{net})\right)} \sin\theta \cos\theta > \mu\ sin^2\theta \cancel{\left((2\ PR \cdot P_{net} + S_H) - (S_h + P_{net})\right)}$$

$$\sin\theta \cos\theta > \mu \cdot sin^2\theta$$

$$\tan\theta < \frac{1}{\mu}$$

Surprisingly, the shear failure condition does not include P_{net} with accepted assumptions which is, obviously, an indication of an unphysical solution. The contradiction may be resolved if some of the assumptions are relaxed (e.g., zero cohesion) or more physical 3D models are applied.

Therefore, the necessary conclusion is that, under assumptions proposed by Nolte and Smith (1981), rock is critically stressed and fails in shear along any natural fracture with approaching angle below critical one:

$$\theta_{crit} = arctan\left(\frac{1}{\mu}\right)$$

For practical cases $0.3 < \mu < 0.85$ and $73^0 > \theta_{crit} > 49^0$. These assumptions, however, are not consistent. Therefore, abovecalculated CFOP may be used only as a first order approximation for inition pressure of natural fractures openeing nearby hydraulic fracture face.

For the estimation of minimum pressure required for keeping the natural fracture open, stress ratio R condition of Delaney et al. (1986); Pollard et al. (1982) was used. Based on field observations of volcanic dikes (natural hydraulic fracturing events) and analytical solution for

mixed Mode I and III opening for echelon cracks, they proposed R stress factor corresponding to the angle θ between the hydraulic fracture and fissures:

$$\frac{(P_f - S_H) + (P_f - S_h)}{S_H - S_h} = R > -\cos 2\theta$$

It was postulated that for R>1 (equivalent to $P_f = S_H$) fissures will open at any unfavorable angle including in the direction of minimum horizontal stress. Therefore, CFOP may be as low as stress anisotropy (~624 psi) or even lower for some favorable oriented fractures.

As mentioned in Section 2.1., White et al. (2014) identified two vertical paleo fracture families: set J1 with azimuths $N30^0$-60^0 and J2 with $N310^0$-330^0. Since azimuth of maximum horizontal stress $N103^0$, natural fractures may be reopened at a pressure lower than predicted by Nolte and Smith (1981):

$$\frac{(P_f - S_H) + (P_f - S_h)}{S_H - S_h} = \frac{2CFOP - ANI \cdot S_h}{ANI \cdot S_h} > -\cos 2\theta$$

$$CFOP > \frac{ANI \cdot S_h(1 - \cos 2\theta)}{2} = ANI \cdot S_h \cdot sin^2\theta$$

So assuming $\theta = 45^0$, $CFOP = 0.5 \cdot ANI \cdot S_h = 312\ psi$. It is easy to show that for subvertical natural fractures CFOP will be higher for normal fauling stress regime due to an additional normal component associated with vertical total stress. These calculations were independently confirmed by Daneshy (2019). Vertical variation of CFOP in the hydraulic fracturing model is presented in **Figure 20**.

2.8.2. Pressure Dependent Leakoff (PDL) coefficient

Pressure Dependent Leakoff (PDL) an empirical coefficient and, in the general case, is coming from DFIT interpretation. In the absence of DFIT data, Parsegov et al. (2018b) proposed to use synthetic DFN and estimate the leakoff coefficient as a function of treatment pressure.

An approximation of stress-dependent fracture permeability for mechanically closed fracture with a rough surface is provided by Walsh (1981):

$$k = k_0 \cdot \left(1 - \sqrt{2}\left(\frac{h}{a_0}\right)\ln\left(\frac{p_e}{p_{0e}}\right)\right)^3$$

The pressure dependent leakoff was calculated for the range of treating pressures from 7,000 psi to 11,000 psi and for various ratios of fracture roughness to reference aperture (h/a_0). The calculation results for the case of h/a_0=0.4 are presented at the semi-log plot in **Figure 19**, together with the best fit exponential curve.

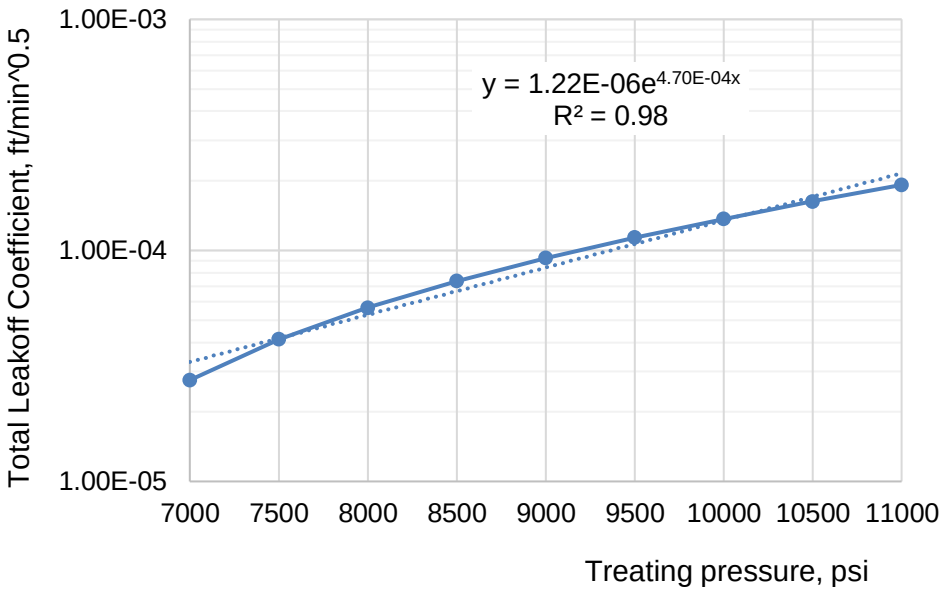

Figure 19 Total leakoff calculated based on generated DFN as a function of the bottom hole treating pressure. From the fitting equation, the pressure-dependent leakoff coefficient (PDL) is 0.00047 psi-1. Reprinted with permission from Parsegov et al. (2018b).

In this study, a moderate PDL coefficient of 0.0005 psi^{-1} is used because of better history matching. It is worth to notice that the PDL coefficient is estimated as an apparent property for entire DFN. In reality, local variations of the PDL coefficient may arise in areas with more dense network fractures.

2.9. Model parameters

After combing all available public data sources and assumptions, the following static grid model (**Figure 20**) was used for hydraulic fracture propagation. Track 1 shows geomechanical parameters – PR (red line) and YM (green line). Track 2 represents Biot's coefficient (red line) and permeability (green line). Estimated Porosity (PHIE, red line) and mineraology (volume share of dolomite – green line and limestone – blue line) are on Track 3/

Track 4 shows Pore pressure (red line) and estimation of PZS (green line). Finally, Track 5 demonstrates pseudolog for CFOP (red line) and S_{hmin}(green line).

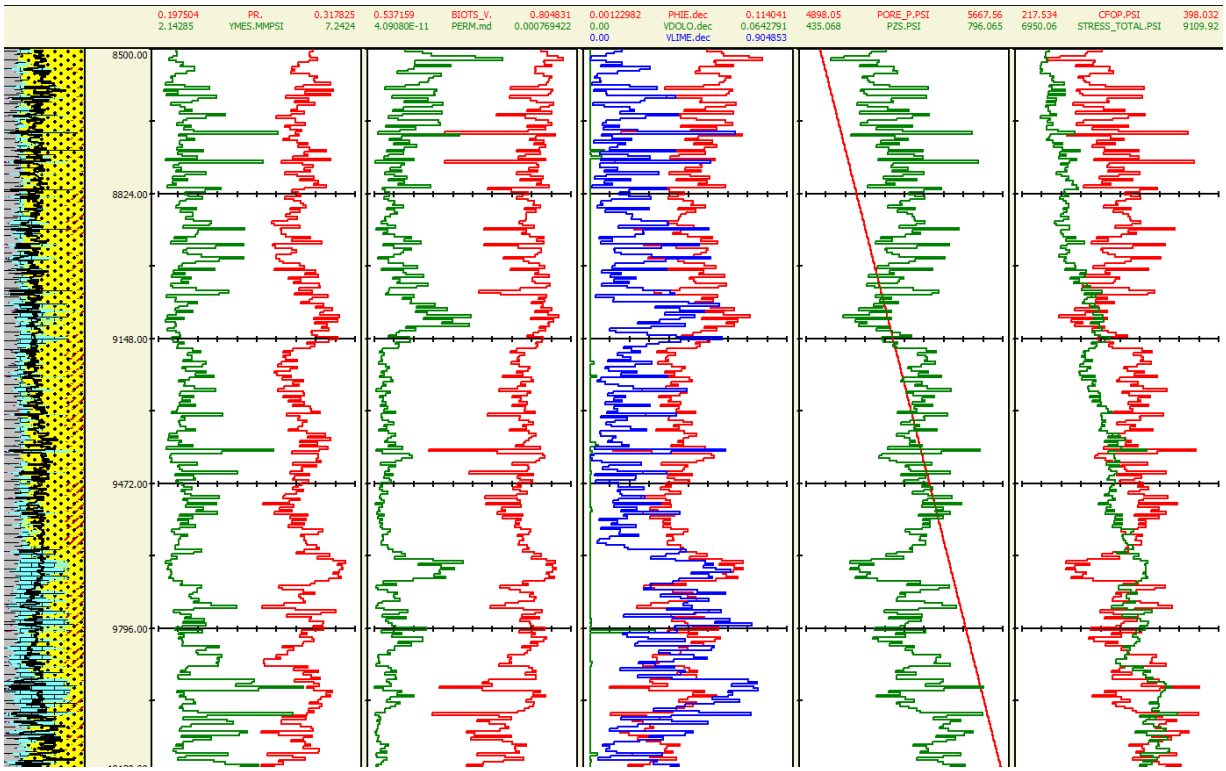

Figure 20 Key model parameters used in the grid-based model.

The recorded difference in EOJ ISIP and pressure 5 minutes after the pumps shutdown is higher than 400 psi. Since PZS for most of the grid blocks is higher than CFOP, fracture propagation will be associated with open tensile fissures and pressure-dependent leakoff. For a typical stage, the difference between average net treatment pressure and CFOP is 2,500 psi, resulting in 3.5 times higher leakoff in nodes close to the wellbore than original leakoff coming from matrix permeability only.

3. MODELING RESULTS AND DISCUSSION*

Modeling outcome from the hydraulic fracturing model consists of two parts:

1. Vector output. Time evolution of pressure, total leakoff, and fluid efficiency as a response for the specified geomechanical model, fluid and proppant ramp-up schedule;
2. Grid output. Time dynamics of grid attributes, including proppant concentration and baseline conductivity, after correction for all mechanisms of conductivity loss, including proppant embedment, pack compression and failure of grains.

The first set of output was used for validation purposes, the second one for making observations, interpretations, and recommendations. Validation of simulation results consists of matching between measured and modeled parameters in particular – treatment pressure.

Figure 21 demonstrates vector output for key treatment parameters: slurry rate, Bottom Hole Pressure (BHP), Pipe Friction, Wellhead and Bottom Hole proppant concentrations. It can be noticed that proppant ramp-up schedule designed in such a way that bottom hole and wellhead concentration overlap and provide constant tubular pressure losses. In these moments behavior of wellhead and bottom hole pressure is the same and variation of wellhead pressure may be used as a diagnostic tool for proppant flow restrictions. The pressure increase at timestamp 87 min may indicate an increase in pressure losses in fractures.

* Part of the data reported in this chapter is reprinted with permission from "Physics-Driven Optimization of Drained Rock Volume for Multistage Fracturing: Field Example from the Wolfcamp Formation, Midland Basin" by Parsegov, S.G., Nandlal, K., Schechter, D.S., and Weijermars, R. in Proceedings of the 6th Unconventional Resources Technology Conference. Copyright 2018 by American Association of Petroleum Geologists; and from "Benefits of Engineering Fracture Design. Lessons Learned from Underperformers in the Midland Basin" by Parsegov, S.G., Niu, G., Schechter, D.S., and Laprea-Bigott, M. in Proceedings of the SPE Hydraulic Fracturing Technology Conference and Exhibition. Copyright 2018 by Society of Petroleum Engineers.

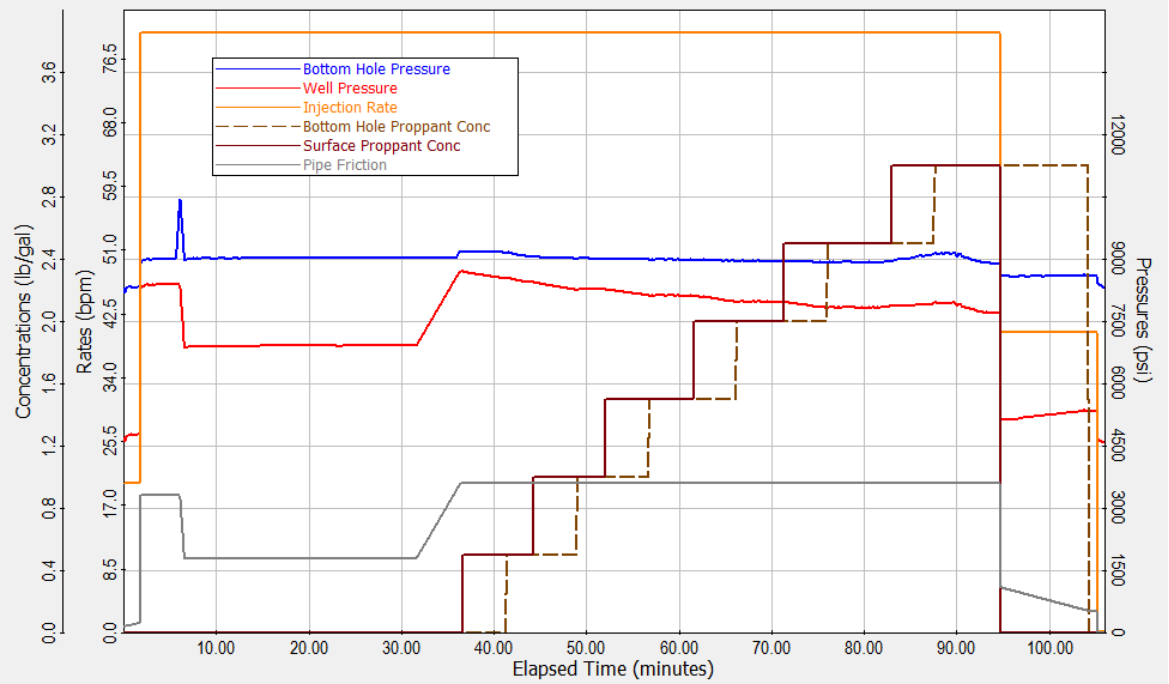

Figure 21 Modeling output for Stage 4 for the treatment design described in Table 1. Vector output for treatment pressure, slurry rate, and proppant concentration. Model output is in a reasonable match with recorded pressure.

In this study, pressure matching is combined with a correlation between modeled fracture geometry and recorded ISIP at pad stage (pad ISIP) and after the end of the job (EOJ ISIP) in Section 3.3.

Figure 22 and **Figure 23** demonstrate grid output for a selected transverse fracture for Stage 4, Cluster 3. Fracture geometry effects and observations are discussed in Section 3.2. The difference between the proppant distribution grid is discussed in Section 3.4. and created effective conductivity is discussed in Section 3.5. Mitigation strategies for more consistent proppant placement are discussed in Section 3.8.

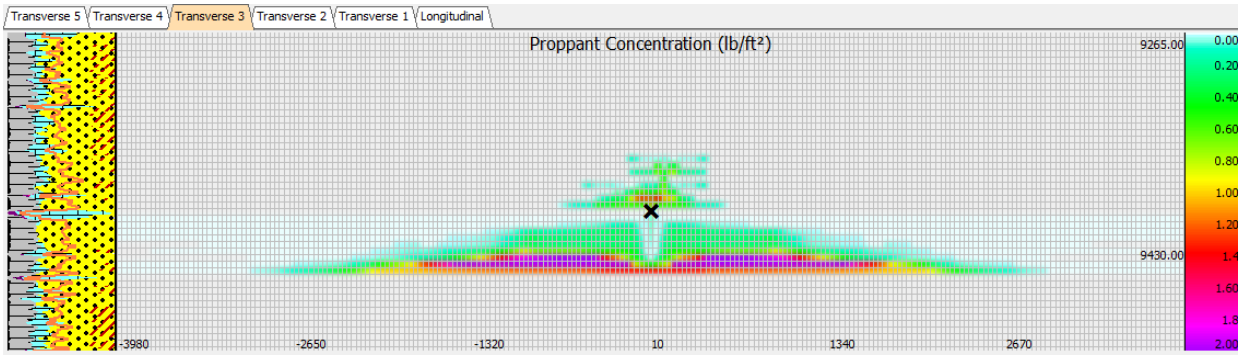

Figure 22 Proppant concentration [lb/ft^2] grid output for transverse fracture of Stage 4, Cluster 3.

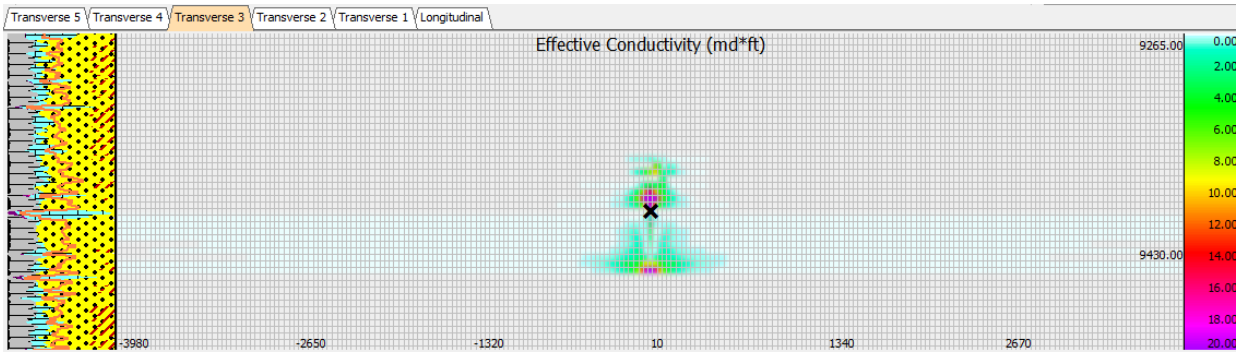

Figure 23 Effective conductivity [mD·ft] grid output for the transverse fracture of Stage 4, Cluster 3.

3.1.Scale-dependent solution

Mechanical properties of rock masses heterogeneous on the multiple scales from micrometers for individual grains to log scale of feet and seismic scales of hundreds of feet Parsegov and Schechter (2017). Chosen commercial planar-3D simulator (GOHFER v. 9.1) is based on a rectangular grid. Therefore, all material properties should be averaged inside each cell before simulation. In addition to that, fracture propagation in the simulation depends on the

chosen failure criterion in the boundary cells. Classical Linear elastic fracture model relies on constant critical fracture toughness, whereas grid-based simulators require an equivalent extra pressure to initiate the fracture propagation to the next cell.

3.1.1. Process Zone Stress

Shlyapobersky et al. (1988) pointed out that observed in field tests fracture toughness is an order of magnitude higher than conducted from laboratory tests. Therefore, a common assumption of constant fracture toughness may not be valid. Yew and Liu (1993) carried out theoretical work to analyze the effects of lagging fluid front during hydraulic fracturing for the apparent fracture toughness. They concluded that critical fracture toughness in a small scale laboratory experiment should be corrected for the size and shape of the dry fracture zone.

GOHFER combines tip effects of the fluid lag zone and tensile processing zone (fracture toughness) by conversion into effective Process Zone Stress (PZS). Since in LEFM fracture toughness has a dimension of [psi·inch$^{0.5}$], conversion into Process Zone Stress (PZS) is grid-scale dependent as the square root of grid cell length. By default the vertical resolution of the grid is 5 ft and aspect ratio 2:1, leaving the horizontal resolution to be 10 ft. Meanwhile, in the previous version – GOHFER v. 8.4, this default value was 10 ft, with a horizontal resolution of 20 ft.

For 20 ft length cell typical values of the fluid lag zone are in a range of 1-10 ft and plastic zone in the range of 2-6 ft as measured in Nevada test site by Warpinski (1985). It is unclear, however, how GOHFER models both effects in one grid block if the block length is less than 20 ft. There are two practical solutions for this problem: usage of PZS as a calibrating

parameter or increase of aspect ratio for 5 ft vertical resolution case from default 1:2 to 1:4, so the grid block will be long enough – 20 ft to accommodate both effects.

For the new versions, it is recommended to imply a numerical routine for autocalibration of field test results to grid value of PZS depending on the grid block length. In general case, equivalent PZS in the grid should be inversely proportional to the square root of the boundary grid block length.

3.1.2. Grid size dependent solution

In addition to the variation of apparent PZS with a size of the grid cells, vertical and lateral averaging of mechanical properties creates additional numerical artifacts which should be distinguished during analysis of results.

The standard reporting resolution of logs in Log ASCII Standard (LAS) files is 0.5 ft (6 inches), though the true resolution of sonic logs about the distance between receivers and is about 2 ft. Formation layers thinner than 2 ft may still be resolved, although the signal will not be fully developed. For density log vertical resolution is driven by the distance between near and far detectors and is about 10 inches. Hence, with density logs, beds can be resolved if the thickness is higher than 2 ft. The vertical resolution of the gamma log depends on logging speed and typically is about 3 ft. Vertical resolution may be improved via deconvolution, but this process usually reduces signal-to-noise ratio and adds numerical artifacts. From that, we can conclude that 3ft is the reasonable minimum for a vertical resolution of the numerical model. Shelokov et al. (2017) report vertical resolution of 4-6 ft for Wolcamp formation of sonic logs. It was also mentioned that only 15% of wells have sonic logs “of different quality”.

Numerical experiments with a 2.5 ft resolution grid showed high associated memory cost. At the same time, upscaling and averaging MEM creates numerical artifacts. In the case of multilayer formation, arithmetical averaging will reduce stress contrast (averaging of Poisson's ratio) and rock stiffness (static Young's modulus). For fracture propagation, problem upscaled case will result in taller and shorter fractures with higher values of fracture width. Hence, proppant distribution will be more favorable as well as resulted in fracture conductivity.

To illustrate this logic test cases were conducted on the synthetic model, similar to field data for treatment well #46 (Error! Reference source not found.). For the sake of simplicity, only one stage was modeled with three clusters in the toe section of the well.

Proppant is add-up in small increments, at Stage 7 there is a local maximum of proppant concentration – 2.6 ppa, after that in stage 8 concentration set to decrease to 2.0 ppa to illustrate the effect of overflush in viscous gels and at stage 10 by overflush with slickwater and concentration of 1.0 ppa. The slurry rate is kept constant 80 bpm for 3 clusters during proppant add-up, and 63 bpm for slickwater overflush.

Table 3 Treatment configuration for scale dependency test. Synthetic data. Guar loading set to be 40 lbs to increase viscosity and highlight effects of the grid size.

Stage #	Elapsed Time.mm:ss	Stage Time.mm:ss	Fluid	Clean Stage Vol.GAL	Cum Clean Vol.GAL	Proppant	Slurry Conc.PPA	Cum Proppant.LB	Slurry Rate.BBL/M
1	0:00	2:19	Acid_HCl_15%_100F	1722.00	1722.00	<None>	0.00	0.00	17.70
2	2:19	26:12	SlickWater_120F	55020.00	56742.00	<None>	0.00	0.00	50.00
3	28:31	6:01	Stage # Elapsed	20000.00	76742.00	Brady Sand 30/50 (A)	0.25	5000.00	80.00
4	34:32	10:03	Guar_40#_120_SP_2	33012.00	109754.00	Brady Sand 30/50 (A)	0.50	21506.00	80.00
5	44:35	12:27	Guar_40#_120_SP_2	40000.01	149754.00	Brady Sand 30/50 (A)	1.00	61506.00	80.00
6	57:02	10:30	Guar_40#_120_SP_2	33011.99	182765.98	Brady Sand 30/50 (A)	1.50	111023.98	80.00
7	1:07:32	5:13	Guar_40#_120_SP_2	15666.00	198431.98	Brady Sand 30/50 (A)	2.60	151755.59	80.00
8	1:12:44	11:59	Guar_40#_120_SP_2	5002.00	203433.98	Brady Sand 30/50 (A)	2.00	161759.59	80.00
9	1:24:44	3:27	Guar_40#_120_SP_2	9996.00	213429.98	Brady Sand 30/50 (A)	3.55	197245.41	80.00
10	1:28:11	4:00	SlickWater_120F	10121.97	223551.95	Brady Sand 30/50 (A)	1.00	207367.38	63.00
Total	1:32:11				223551.95			207367.38	

In this example, four runs were done with the same conditions except for the size of the grid block and results are presented in **Figure 24**. A huge difference is found between Case A (7.5 ft x 15 ft) with the classical elliptical distribution of proppant concentration at the pumps shut-in and Case D (2.0 ft x 4.0 ft) with fractures of smaller height and longer half-length with a higher concentration of proppant near the wellbore.

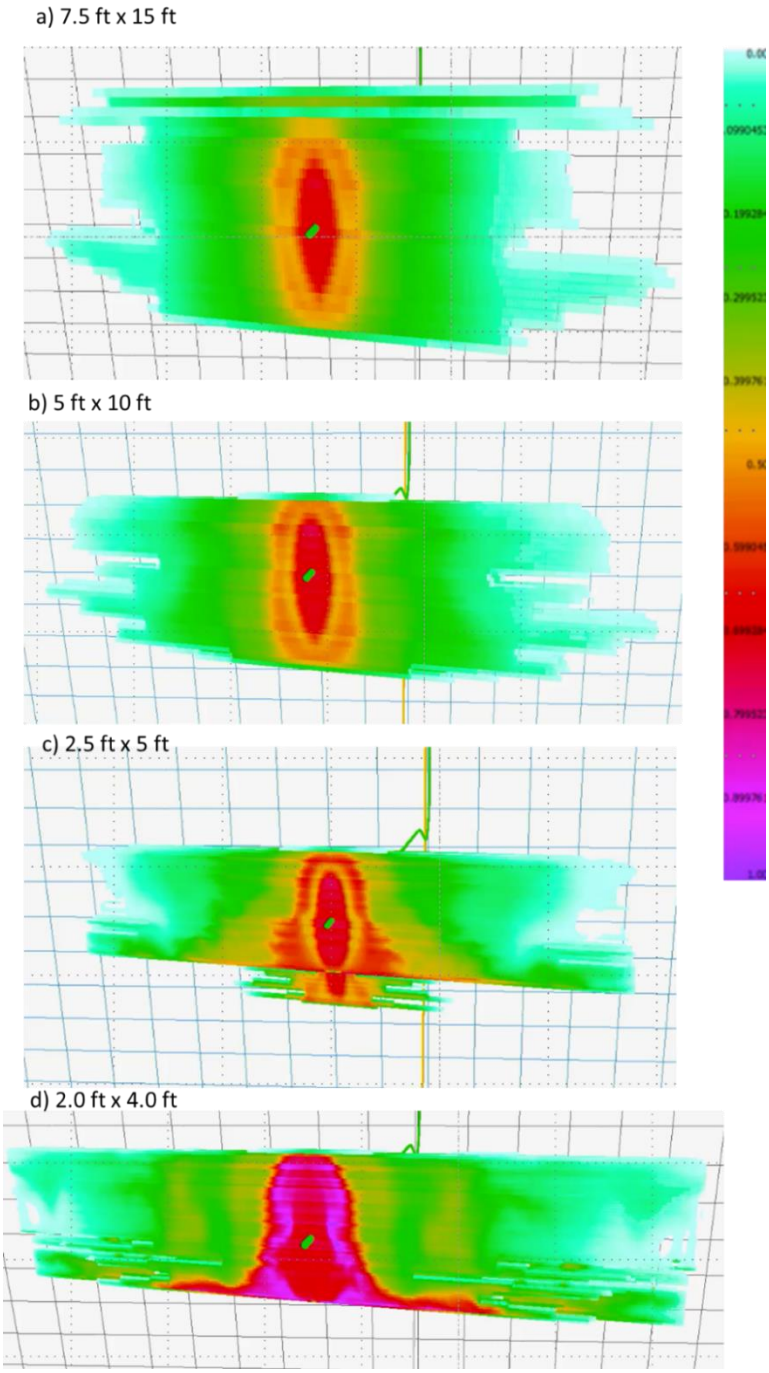

Figure 24 Comparison of runs with different grid block size. Proppant concentration is color-coded from 0 to 1.0 lb/ft^2 at the end of pumping. Each square gridblock on the background is 100 x 100 ft (for scale).

Significant changes of fracture geometry become apparent with grid blocks become smaller because more fracture barriers for vertical fracture propagation come into the calculation. With coarse grid local variations of Young's modulus and Poisson's ratio are averaged and this loss of accuracy resulting in more fracture height generated with a more uniform distribution of proppant. With refining vertical grid resolution from 5 to 2.5 ft, the inner fracture is propagating out of the target interval downward (**Figure 24, case C**). Previously indistinguishable variation of fracture width between layers becomes apparent and results in proppant stripes in the broader open fracture blocks of smaller horizontal stress or Young's modulus.

Finally, in **Figure 24 (Case D**) proppant settles far from the wellbore, and bedload becomes a significant type of proppant transport even with highly loaded gel (guar #40).

Similar observations as described in **Figure 24** were reported for 3rd Bone Spring formation in Delaware Basin by Narasimhan et al. (2017). To avoid described numerical artifacts it is critical to implement a calibration procedure for geomechanical properties in a way that average resulting fracture width becomes scale-independent. In general, FEM modeling is required for delivering new upscaling algorithms for elastic properties to deliver a fracture model with a minimum width profile scale dependency. For simplified cases of vertical variations, both analytical and numerical techniques are described elsewhere Elkateb et al. (2003); Smith et al. (2001).

3.2.Fracture geometry

In all modeled cases axial/longitudinal fractures were open and propped during the simulation (**Table 4**).

Table 4 Simulation results for fracture geometry of Stage 4.

Perforations:	17119-17121' MD, .42" Diam, 8 Holes								
	17179-17181' MD, .42" Diam, 8 Holes								
	17239-17241' MD, .42" Diam, 8 Holes								
	17299-17301' MD, .42" Diam, 8 Holes								
	17359-17361' MD, .42" Diam, 8 Holes								
Total Clean Volume:	315,796 gallons								
Total Proppant:	335,000 lbs								
Cum. Fluid Lost:	140,836 gal								
Fracture	Gross Frac Length.ft	Proppant Cutoff Length.ft	Est Flowing Frac Length.ft	Est Inf Conductivity Length.ft	Fracture Height.ft	Average Proppant Conc.lb/ft²	Average Fracture Width.in	Max Fracture Width.in	
Transverse 5	4010.00	220.00	3.93	3.92998	55.00	0.617588	0.207	0.287	
Transverse 4	3190.00	160.00	3.59424	3.59408	55.00	0.339163	0.108676	0.17	
Transverse 3	4010.00	220.00	3.8938	3.89365	80.00	0.432663	0.163337	0.326	
Transverse 2	4010.00	160.00	2.76118	2.76093	60.00	0.161487	0.113269	0.211	
Transverse 1	590.00	110.00	2.99492	2.99474	30.00	0.291615	0.051903	0.21	
Longitudinal 1	320.00	270.00	2.87694	2.87681	20.00	0.325611	0.0457583	0.213	
Fluids:	SlickWater_120F								
	Acid_HCl_15%_100F								
	Guar_10#_120_SP_1								
Proppants:	Brady Sand 40/70 (A)								

It was noticed that Gross Frac Length (length of open fracture or "wet length") is an order of magnitude higher than Proppant Cutoff Length (fracture length covered by proppant above a cutoff concentration, for example, of 0.1 lb/ft^2). Gross fracture length (wet length) controls pressure hits on offset wells, whereas flowing length is an estimation of the length which can be cleaned up from the gel residuals (Predict-K model) and contributes to production. Infinite conductivity length is estimated from flowing length and created fracture conductivity Barree et al. (2003):

$$X_{inf} = \frac{X_{flowing}}{1 + \left(\frac{\pi}{2}\frac{1}{C_{fd}}\right)}$$

For some stages (e.g., Stage 4 in **Table 4**), wellbore geometry was favorable for growing a single longitudinal fracture. For some stages (e.g., Stage 6 in **Table 5**) multiple short longitudinal fractures were observed. Length of individual longitudinal fractures varies because

of the wellbore curvature and ranges from 20 ft to 320 ft. With cluster spacing of 60 ft, axial fractures create conductive channels between clusters and stages averaging production of individual perforation clusters and reducing adverse effects of nonuniform stimulation.

Table 5 Simulation results for fracture geometry of Stage 6.

Perforations:		16519-16521' MD, .42" Diam, 8 Holes							
		16579-16581' MD, .42" Diam, 8 Holes							
		16639-16641' MD, .42" Diam, 8 Holes							
		16699-16701' MD, .42" Diam, 8 Holes							
		16759-16761' MD, .42" Diam, 8 Holes							
Total Clean Volume:		315,996 gallons							
Total Proppant:		335,000 lbs							
Cum. Fluid Lost:		142,038 gal							
Fracture		Gross Frac Length.ft	Proppant Cutoff Length.ft	Est Flowing Frac Length.ft	Est Inf Conductivity Length.ft	Fracture Height.ft	Average Proppant Conc.lb/ft²	Average Fracture Width.in	Max Fracture Width.in
	Transverse 5	4010.00	190.00	3.76	3.76	75.00	0.412703	0.177907	0.241
	Transverse 4	4010.00	190.00	3.78505	3.78492	35.00	0.415729	0.162815	0.253
	Transverse 3	4010.00	210.00	3.6943	3.69418	55.00	0.487318	0.165241	0.274
	Transverse 2	4010.00	210.00	3.77212	3.77201	55.00	0.490523	0.158109	0.269
	Transverse 1	3140.00	0.00	0.798754	0.10	0.00	1.10600E-07	0.079525	0.0985
	Longitudinal 1	20.00	10.00	2.29268	2.29264	5.00	0.556	0.036315	0.0679
	Longitudinal 2	20.00	10.00	2.0571	2.05705	10.00	0.353067	0.0336133	0.0861
	Longitudinal 3	20.00	20.00	2.61775	2.61772	20.00	0.548751	0.055968	0.176
	Longitudinal 4	20.00	20.00	2.6127	2.61267	20.00	0.540964	0.053588	0.166
	Longitudinal 5	30.00	20.00	2.63695	2.63691	20.00	0.760903	0.0848892	0.173
Fluids:		SlickWater_120F							
		Acid_HCl_15%_100F							
		Guar_10#_120_SP_1							

Transverse fractures from the clusters 1 and 2 of each stage (except for the toe one) have much smaller length and height due to mechanical interaction with fractures of the previous stage. Transverse fractures from the heel side clusters of each stage are generally the biggest. This adverse effect of stress shadowing may be identified by switching stress shadowing option between stages and partially mitigate by perforation redesign and use of diverters. Due to unfavorable geomechanical conditions, transverse fracture from the Cluster 1 of Stage 6 has virtually no proppant placed, and it was closed unstimulated.

Therefore fracture hit may be observed thousands of feet from the treatment wellbore in an offset well. For Eagle Ford formation pressure communication was observed over 3,000 ft. At the same time, due to inefficient proppant placement and conductivity degradation effective flowing fracture length and conductivity is disappointing.

Surprisingly small fracture height and surprisingly long fracture length for lower Wolfcamp may be attributed to strong high-stress fracture barriers and is similar with reported previously as modeling result of the 3D planar model in the vertical well by Alimahomed et al. (2017) in **Figure 25**. From this modeling, it may be concluded that three landing zones may be targeted in lower Wolfcamp because of smaller than in Upper Wolfcamp heights. With 80 bpm pumping rate, longer fractures were observed in Lower Wolfcamp and therefore with the same fracture design these landing zones are more prone for lateral fracture hits. Similar observations were made from the microseismic monitoring of multistage hydraulic fracturing presented in **Figure 4**.

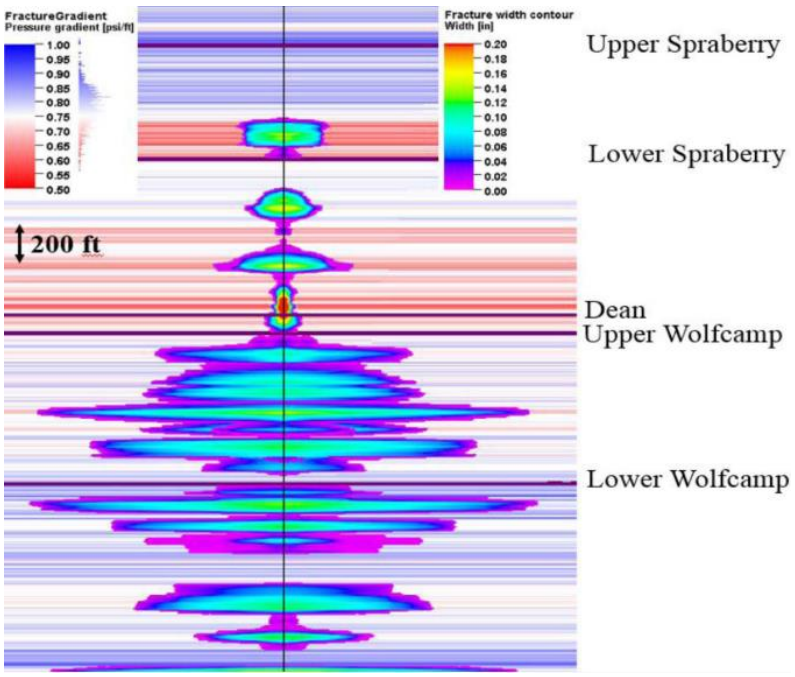

Figure 25 Geometry of individual fractures landed in different zones. Reprinted with permission from Alimahomed et al. (2017).

3.3.Stress shadowing and ISIP

It was found that fractures exhibit 3D behavior and due to stress shadowing can grow out of the target interval which reduces the severity of the adverse effect. Stress shadowing between stages and between clusters is modeled in GOHFER in the same manner – by applying Boussinesq's solution with empirical transverse exponent coefficient in the range from 1.0 for the plane strain case (linear decay ~1/L) to 2.0 for a point load case (~$1/L^2$).

The strongest stress shadowing effect is in the case of transverse exponent equals unity for plane strain case. It leads to the same result of middle fractures closure at the wellbore as was predicted by Germanovich and Astakhov (2004). It should be noted, however, that Germanovich and Astakhov (2004) used a 2D FEM code and the 2D physical model to illustrate

central fractures closure. Therefore, the stress shadowing effect may be artificially magnified by the assumption of vertical fracture symmetry which may not be the case due to gravity, wellbore inclination and local variations of horizontal stress.

All practical cases should be in between these extremes. In this study transverse exponent is taken to be 1.2 as a recommended default parameter in the simulator. Figure 26 demonstrates the modeling results and highlights significant observations.

For example for Stage 3, the insert in gun barrel view shows a higher concentration of proppant in the middle of target interval around the wellbore (marked as black crosses), nonsymmetrical proppant placement and adverse effects of overflushing.

Stages 3-7 showing bouncing of individual fractures out of target interval due to the mechanical interactions.

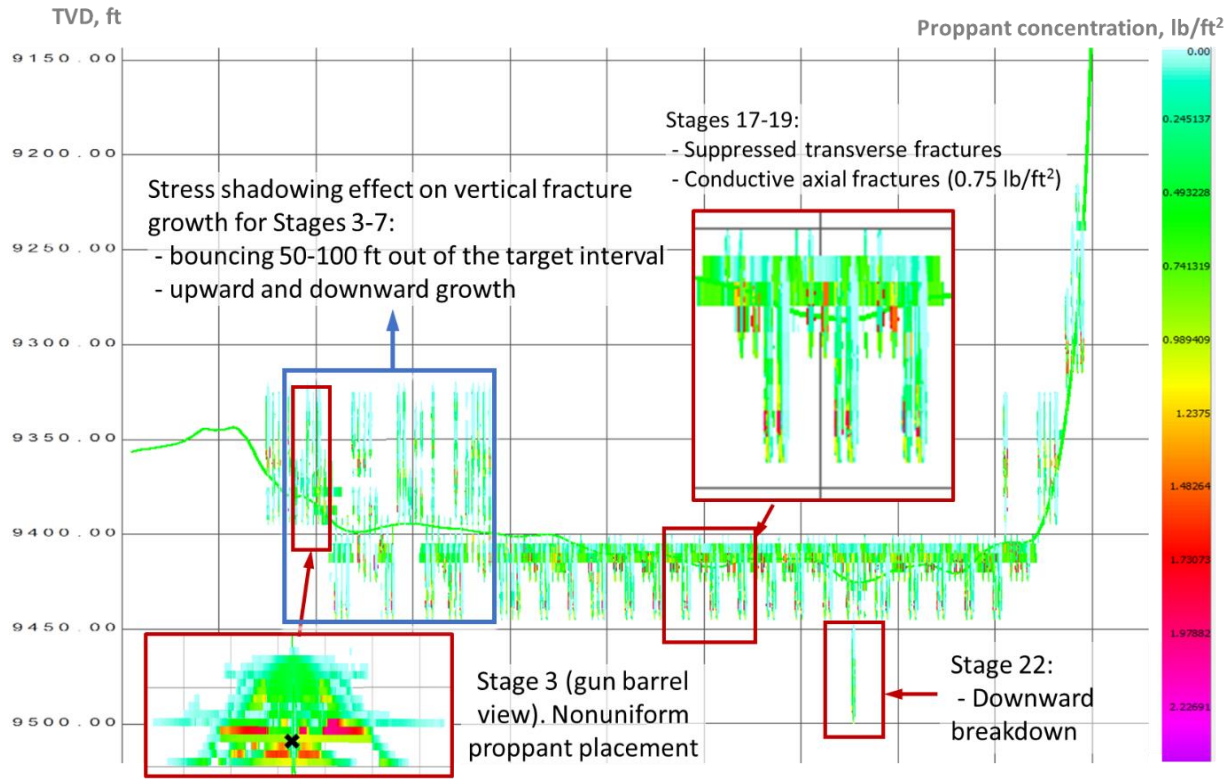

Figure 26 Fracture geometry and proppant concentration for the treatment well #46. Side view. Toe stage is to the left. Reprinted from Parsegov et al. (2018a) with permission from URTeC, whose permission is required for further use.

For stages 17-19 there is a strong indication of highly conductive axial fractures with proppant concentrations comparable or even higher than for transverse ones. Local deviation of the wellbore found to be a control for axial fractures. At some wellbore orientations, axial fractures may cross multiple transverse fractures and effectively connect clusters and stages.

Geometry variation of wellbore profile for Stage 22 results in downward propagation of the fracture from the middle cluster, partial release of cumulative stress shadowing, and more uniform stimulation at Stage 23.

In order to verify modeling results, created fracture geometry in 3D was superposed with stage-by-stage measurement of ISIP at the begging of pad stage (pad-ISIP) and the end of pumping – end of the job (EOJ ISIP).

Figure 27 shows measured pad ISIP and EOJ ISIP superpositioned with modeled proppant distribution (side view). Such a comparison of field and model data allows correlating stress shadowing effect with fracture geometry. Stages 2-12 demonstrate a general escalation of ISIP (200 psi/stage) which corresponds to taller fractures from these stages as predicted by Roussel (2017).

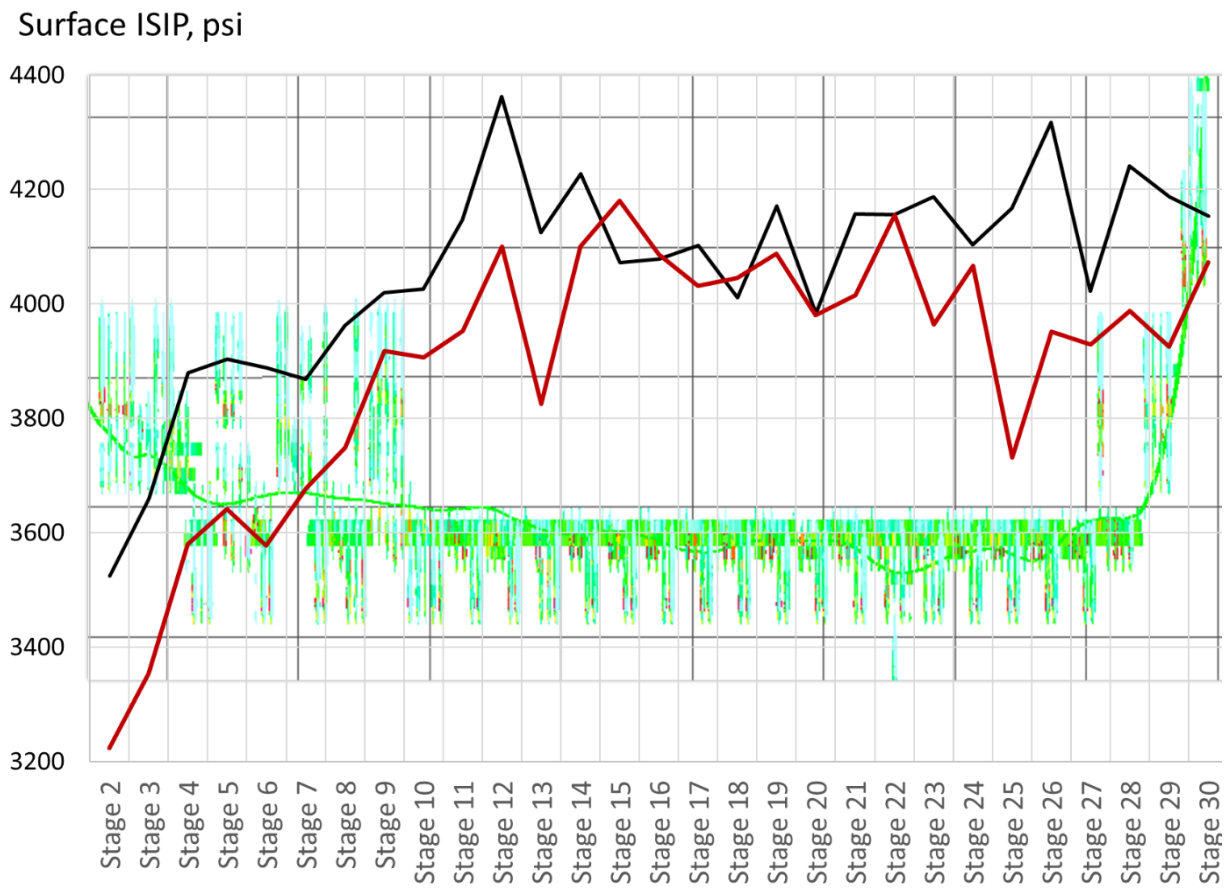

Figure 27 ISIP surface measurements for the treatment well #46. Pad ISIP – red line, EOJ ISIP – black line. Modeled proppant concentration map is used as a background for comparison between fractures geometry and ISIP response. Warmer colors mean higher proppant concentration as background. The solid green line represents wellbore.

However, each change of the direction of vertical propagation from preferably upward growth to preferably downward propagation and vice versa lead to smaller increments or even drop of ISIP values (Stages 4-7). Therefore, a drop of measured ISIP may be an indication of asymmetrical fracture growth against horizontal plane (Stages 3-7) or fracture breakdown out of the zone (Stages 22 and 27).

Comparison of pad ISIP and EOJ ISIP behavior also provide some insights. Pad ISIP is lower than EOJ ISIP with exception to Stages 14-23 where two values are close which correspond to the development of stable fracture pattern for each stage – suppression of fractures from first two clusters and predominant growth of fractures from the last three clusters of each stage. This effect may be used for diagnostic purposes. Since in multicluster completion ISIP measurement shows the minimum pressure among all clusters, similar values of pad ISIP and EOJ ISIP may have predictive power for detection of understimulated clusters and nonuniform proppant placement in the bottom of fractures. For the modeled case it indicates suppressed stimulation of the first two clusters in each stage.

Two simulations were done to show the importance of stress shadowing effect in 3D for stimulation of the Treatment well #46. **Figure 28** demonstrates solution with zero mechanical interaction between stages. As expected, without stress shadowing between stages proppant placement is more uniform between clusters and all transverse fractures have similar geometry.

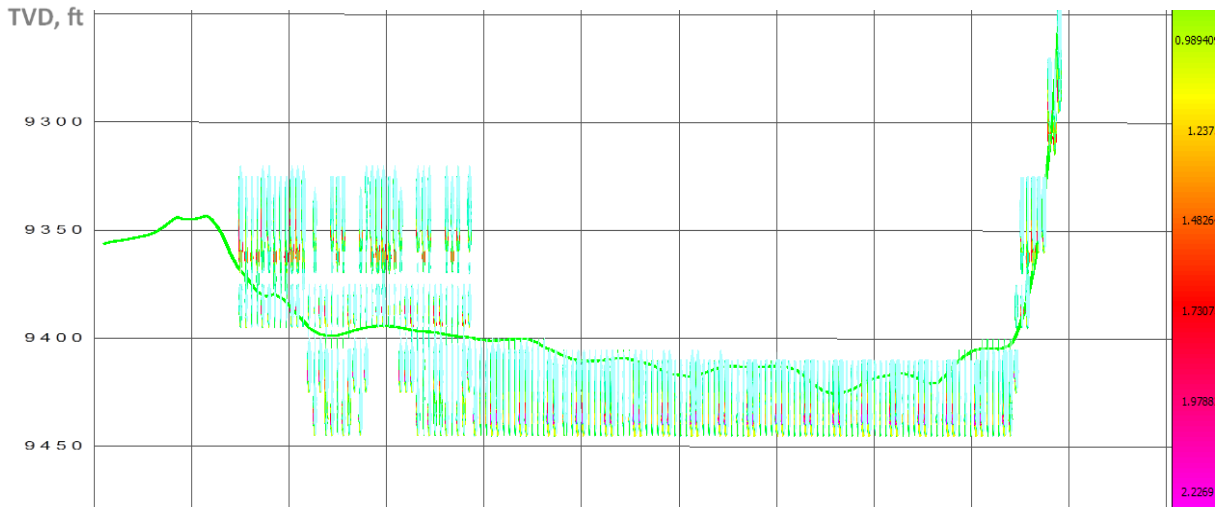

Figure 28. Hydraulic fracturing simulation output for proppant placement without stress shadowing between stages. Reprinted from Parsegov et al. (2018a) with permission from URTeC, whose permission is required for further use..

3.4. Proppant transport

In Section 1 I presented some gaps in industry understanding of proppant transport mechanisms in thin fluids and related usage of large pad stages and proppant-laden schedule.

Figure 29 demonstrates sporadic proppant placement due to vertical stress variation. Some low-stress layers with wide-open fracture segments received as much as 2.0 lb/ft2. At the same time interconnection of these highly conductive zones is challenged by proppant settling below the wellbore. In extreme case of the middle cluster, all proppant is placed below the target interval and virtually isolated from the wellbore with slickwater overflushing. It is worth mention that the proppant pack at shut-in does not reach equilibrium height. Therefore with the same fracture geometry, an increase of sand volumes with increase effective flowing fracture height and length.

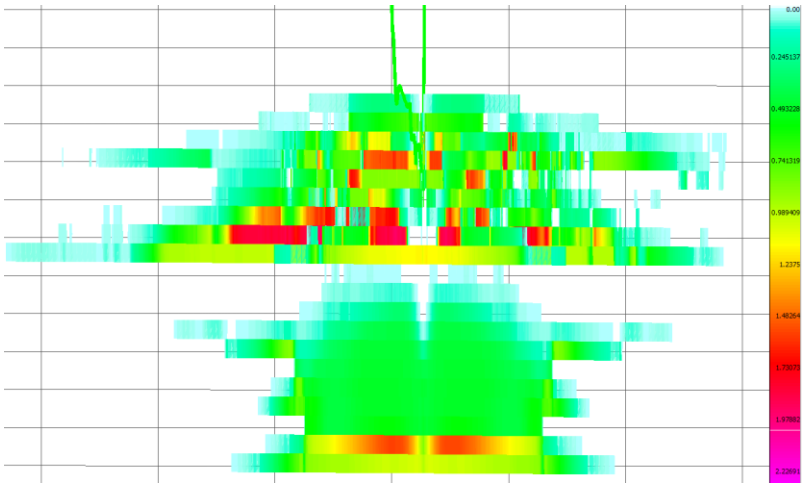

Figure 29 Proppant placement [lb/ft^2] for the Stage 22 (compositional gun barrel 3D view for all clusters, highly vertically exaggerated). Because of wellbore curvature, the inner cluster broke the lower stress barrier. Proppant for this cluster settled out of the target interval. Each colored pixel is 5ft x 10ft.

Middle fracture in **Figure 29** also shows an adverse effect of overflushing for final conductivity around the wellbore. In addition, to overflush, even thin (5-10ft) layers of calcite-rich rock (associated with high closure stress and high Young's modulus) received a lower amount of proppant. Such pinchout layers cut proppant pack from the wellbore at TVD of 9,425-9,435 ft.

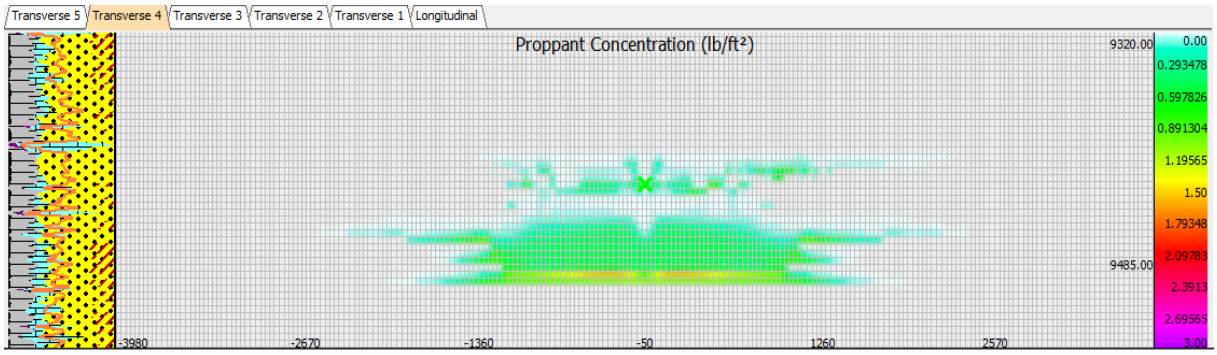

Figure 30 Proppant distribution for Stage 22, Cluster 4. Each grid cell is 5 ft height and 10 ft long.

Similar observations were made from coring through Upper and Middle Wolfcamp at Hydraulic Fracturing Test Site (HFTS) in Reagan County, published by Maity et al. (2018).

Therefore, the presence of proppant depends on the vertical and lateral variation of rock properties and requires physics-based modeling of fracture propagation before setting geological targets for drilling operations.

3.5. Fracture closure and final conductivity

One of the weak points of the selected simulator is its inability to predict fracture closure after pumps shut down. Therefore it is hard to predict exact migration of proppant during fracture closure. For high permeable formation, it is not an issue since slurry dehydrated fast enough to secure closure on proppant without significant proppant settlement from the slurry. For low permeable reservoirs, the fracture closure may take days and proppant will settle in the bottom of the created fracture since the industry moved from crosslinked gels to slickwater fracturing. However, this limitation does not seem critical for two reasons:

1. Real fracture surface has roughness, and multiple horizontal offsets effectively settle proppant at higher elevations that may be predicted with classical models assuming flat parallel fracture walls.
2. Slickwater and linear gel proppant transport are not as effective for viscous drag transport mechanism as in cross-linked gel slurry. Therefore with dominant bedload transport over settled proppant pack (dunes), propped fracture height does not change during the closure.

3.6. Microseismic monitoring

As it has been said, microseismic is a powerful tool to diagnose hydraulic fracturing operations if appropriately done with at least two monitoring wells. For the treatment well, however, only one monitoring well was used. Therefore, all events have higher spatial uncertainty, and it is no data available to conduct moment tensor inversion.

Figure 31 and **Figure 32** illustrate microseismic events location for each pumping stage from left (Stages 2 and 3– colored in dark blue and red respectively) to the right (Stages 7 and 8 colored in grey and indigo respectively). Each grid block is 400 ft x 400 ft.

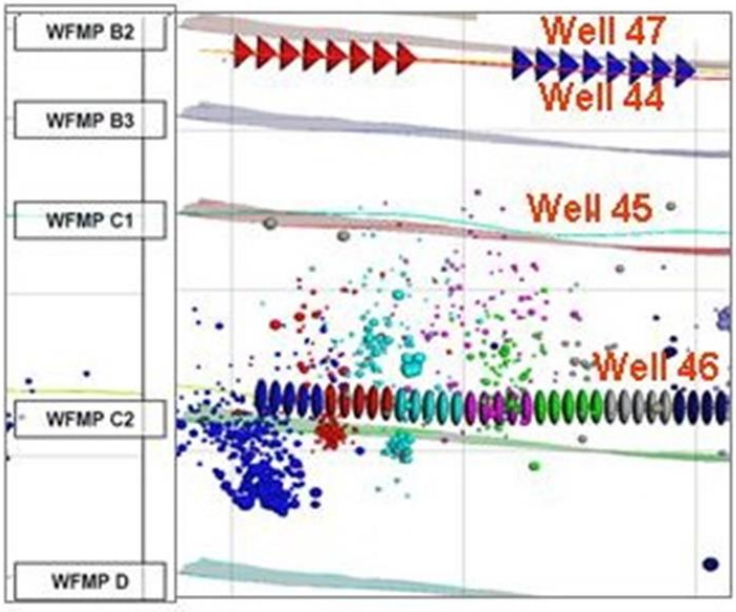

Figure 31 Side view of microseismic events from the treatment well #46. Each grid block is 400 ft x 400 ft. Reprinted from Parsegov et al. (2018a) with permission from URTeC, whose permission is required for further use.

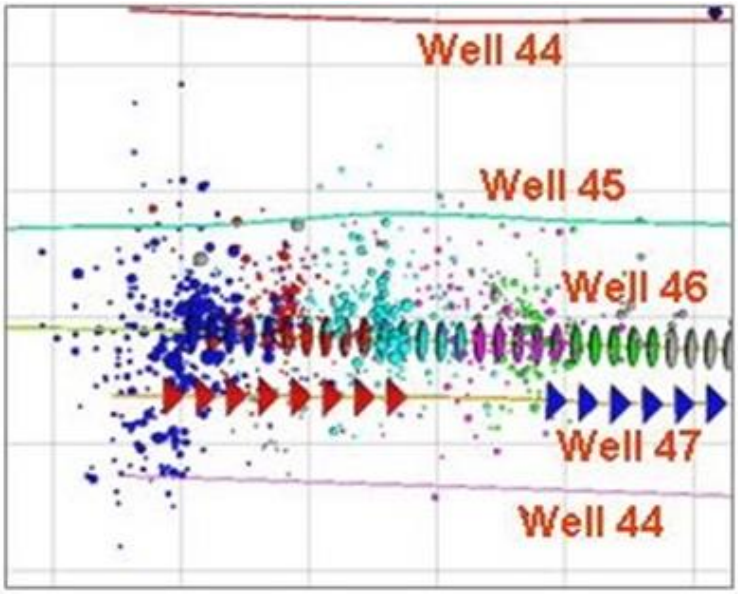

Figure 32 Map view of microseismic events for the treatment well #46. Each grid block is 400 ft x 400 ft. Reprinted from Parsegov et al. (2018a) with permission from URTeC, whose permission is required for further use.

Figure 33 demonstrates the correlation between propped fracture length and recorded microseismic events for Stage 5. Dark blue shaded events in the zone of Stage 4 indicate restimulation in the rock volume of the previous Stage 4. Similar observations are valid for other stages (e.g., Stages 4 and 6).

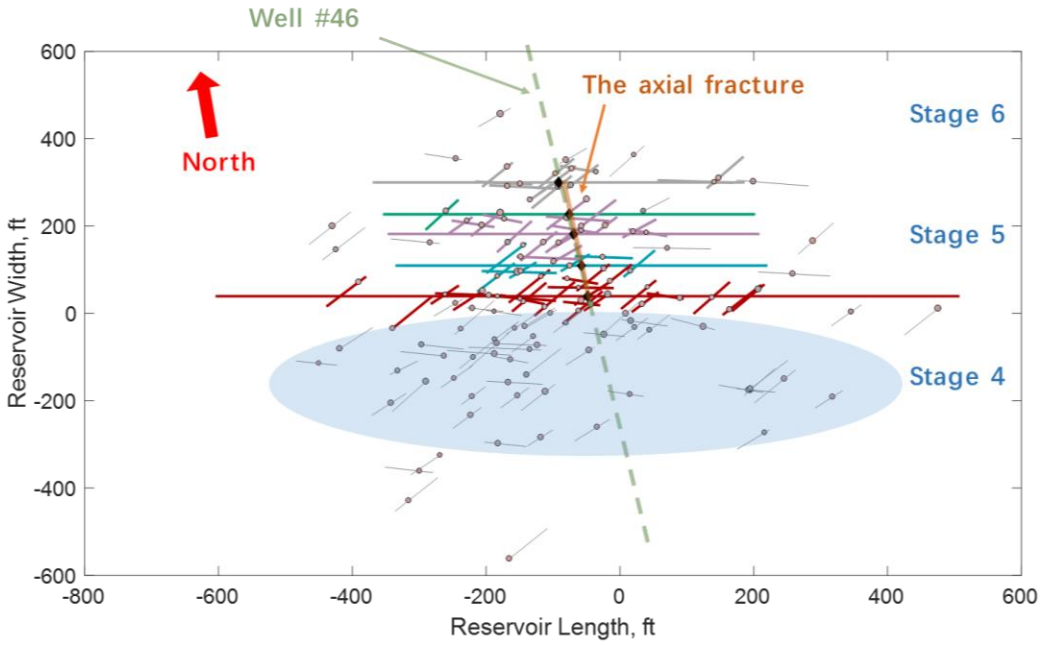

Figure 33 Microseismic monitoring of hydraulic fracturing during the treatment of Stage 5. Map view. Reprinted with permission from Parsegov et al. (2018b).

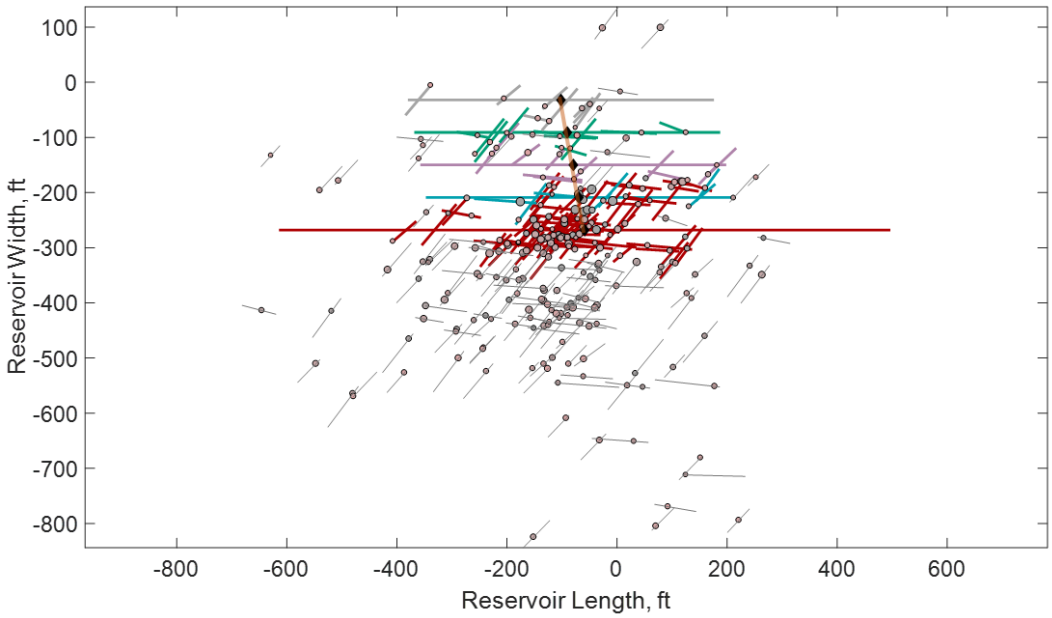

Figure 34 Microseismic monitoring of hydraulic fracturing during the treatment of Stage 4. Map view.

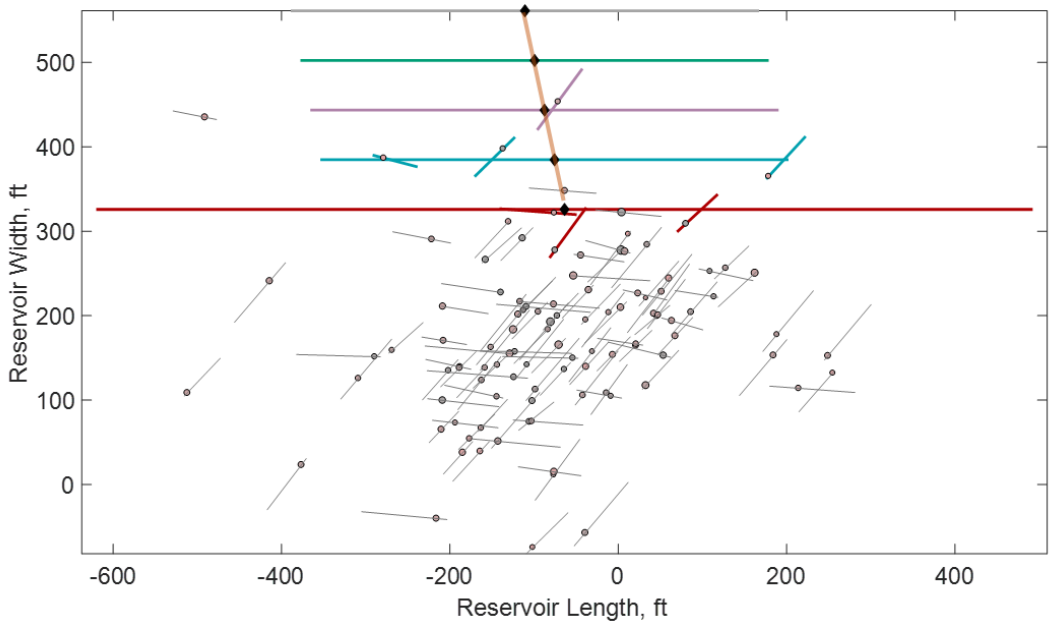

Figure 35 Microseismic monitoring of hydraulic fracturing during the treatment of Stage 6. Map view.

One possible explanation of microseismic activity in the previous stage area is leaking packers, but hydraulic communication over growing axial fractures may also be a factor (solid orange lines in **Figure 33, Figure 34,** and **Figure 35**). As it is shown in Chapter 4 oil and water based tracers study show almost equal flux allocation between individual stages. By taking into account the significant difference in fracture geometries from different stages, some pressure communication between stages due to longitudinal fractures may occur. Another possible explanation is a shear failure or rock mass due to stress relaxation after pumps shut-in as it was measured by Distributed Acoustic Sensors (DAS) by Raterman et al. (2017) in **Figure 36**. This version, however, is less likely to be true, because detected

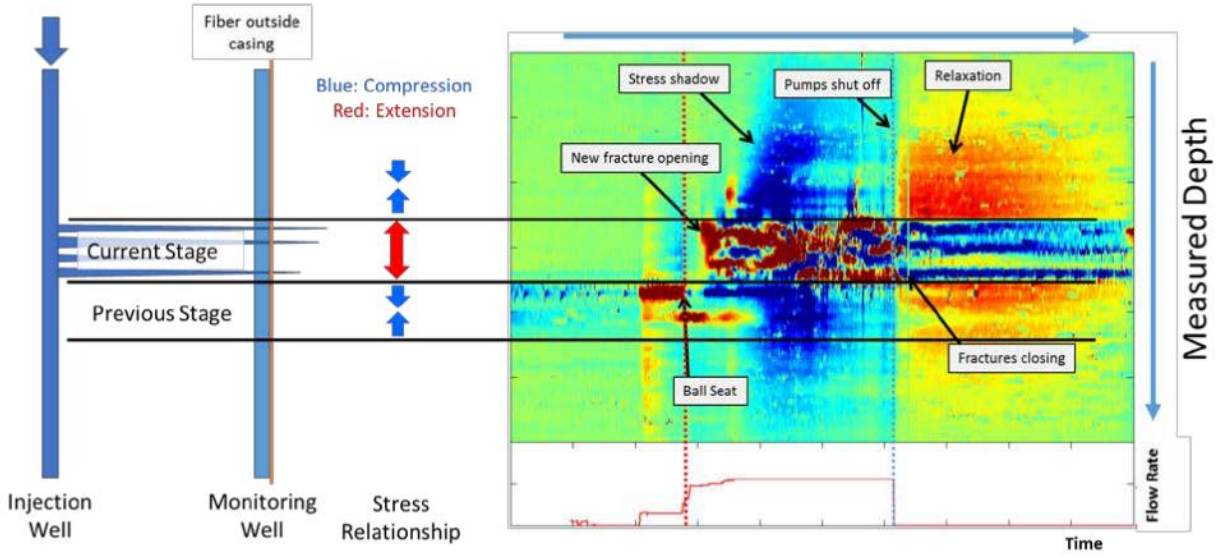

Figure 36 Strain rate in S3 well from DAS during stimulation of offset well. Reprinted from Raterman et al. (2017) with permission from URTeC, whose permission is required for further use.

3.7. Recommendations

It may be concluded that based on the pressure matched model, that chosen size of slick water pad is not required to create fracture width and may be reduced. Hence it can be recommended to reduce the size of the pad stage to decrease treatment cost. Alternatively, an engineer may increase the amount of sand by applying a more aggressive proppant rump-up schedule.

3.7.1. Pad size optimization

The physics-based model showed that relatively low matrix permeability and lack of accelerated pressure-dependent leakoff allows pumping all planned sand volume into the formation without screenout. To show the concept, pad size was reduced by 50% (with the

pumping schedule in **Table 6**, and resulting proppant distribution and effective conductivity are presented in **Figure 38** and **Figure 39** respectively.

Table 6 Proposed pumping schedule for 50% pad scenario (50,000-gal slick water plus 8,400 gal of 10# gel) for Stage 4.

Stage #	Elapsed Time.mm	Stage Time.mm	Fluid	Clean Stage Vol.GAL	Cum Clean Vol.GAL	Proppant	Slurry Conc.PF	Cum Proppant.LB	Slurry Rate.B	Cum Slurry.BE
1	0:00	0:00	SlickWater_120F	0.00	0.00	<None>	0.00	0.00	20.00	0.00
2	0:00	8:02	Acid_HCl_15%_100F	1500.00	1500.00	<None>	0.00	0.00	20.00	160.67
3	8:02	14:53	SlickWater_120F	50000.00	51500.00	<None>	0.00	0.00	80.00	1351.14
4	22:55	2:30	Guar_10#_120_SP_1	8400.00	59900.00	<None>	0.00	0.00	80.00	1551.14
5	25:25	7:37	Guar_10#_120_SP_1	25000.02	84900.02	Brady Sand 40/70 (A)	0.50	12500.01	80.00	2160.48
6	33:02	7:47	Guar_10#_120_SP_1	25000.00	109900.02	Brady Sand 40/70 (A)	1.00	37500.01	80.00	2783.14
7	40:49	9:32	Guar_10#_120_SP_1	29999.99	139900.00	Brady Sand 40/70 (A)	1.50	82499.99	80.00	3545.81
8	50:21	9:45	Guar_10#_120_SP_1	30000.00	169900.00	Brady Sand 40/70 (A)	2.00	142500.00	80.00	4325.81
9	1:00:06	11:36	Guar_10#_120_SP_1	35000.00	204900.00	Brady Sand 40/70 (A)	2.50	230000.00	80.00	5254.19
10	1:11:42	11:51	Guar_10#_120_SP_1	35000.00	239900.00	Brady Sand 40/70 (A)	3.00	335000.00	80.00	6202.19
11	1:23:33	10:25	SlickWater_120F	17490.00	257390.00	<None>	0.00	335000.00	40.00	6618.62
12	1:33:58	1:26	SlickWater_120F	6.00	257396.00	<None>	0.00	335000.00	0.10	6618.77
Total	1:35:23				257396.00			335000.00		6618.77

Treatment pressure curves from **Figure 37** demonstrates that pad reduction by 50% does not create treatment pressure spikes and risk of screenout.

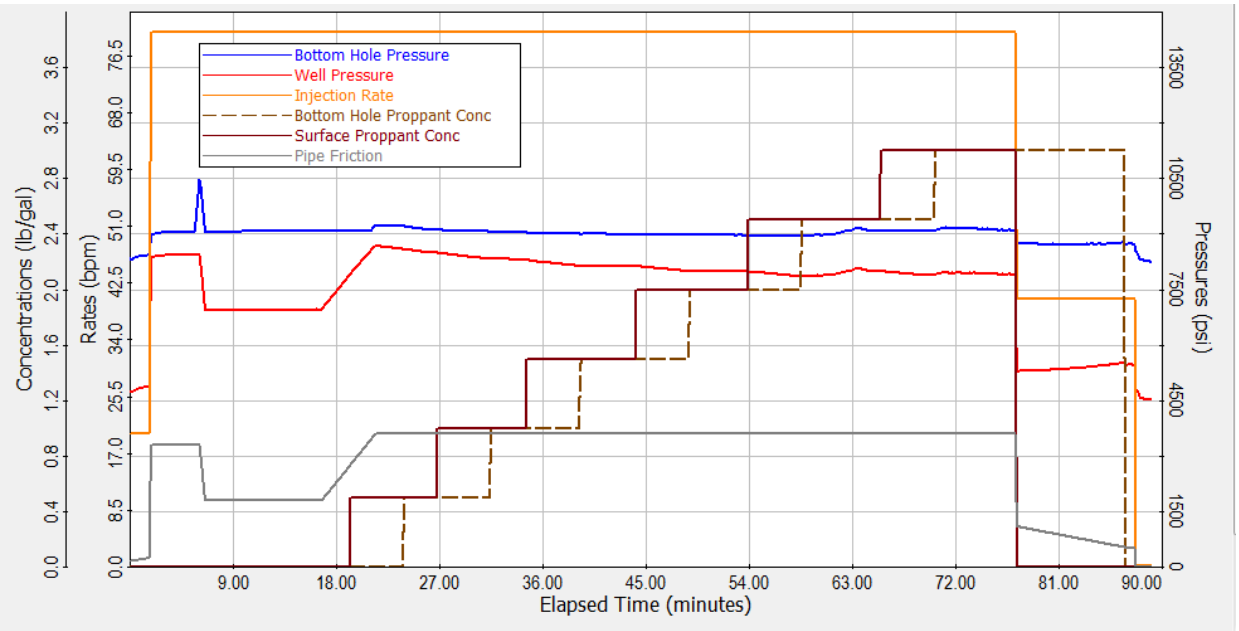

Figure 37 Vector output for 50% pad scenario for Stage 4.

Table 7 demonstrates that scenario "50% pad" involves the same Gross fracture length; at the same time proppant is distributed more equally between transverse fractures. Reduction of pad volume reduces proppant cutoff length for longitudinal fracture (-10%) and increase the wet height of the longitudinal fracture.

Table 7 Model output for base case scenario and "50% pad" scenario.

a) Base case scenario.

Perforations:		17119-17121' MD, .42" Diam, 8 Holes							
		17179-17181' MD, .42" Diam, 8 Holes							
		17239-17241' MD, .42" Diam, 8 Holes							
		17299-17301' MD, .42" Diam, 8 Holes							
		17359-17361' MD, .42" Diam, 8 Holes							
Total Clean Volume:		315,796 gallons							
Total Proppant:		335,000 lbs							
Cum. Fluid Lost:		140,836 gal							
Fracture		Gross Frac Length.ft	Proppant Cutoff Length.ft	Est Flowing Frac Length.ft	Est Inf Conductivity Length.ft	Fracture Height.ft	Average Proppant Conc.lb/ft²	Average Fracture Width.in	Max Fracture Width.in
	Transverse 5	4010.00	220.00	3.93	3.92998	55.00	0.617588	0.207	0.287
	Transverse 4	3190.00	160.00	3.59424	3.59408	55.00	0.339163	0.108676	0.17
	Transverse 3	4010.00	220.00	3.8938	3.89365	80.00	0.432663	0.163337	0.326
	Transverse 2	4010.00	160.00	2.76118	2.76093	60.00	0.161487	0.113269	0.211
	Transverse 1	590.00	110.00	2.99492	2.99474	30.00	0.291615	0.051903	0.21
	Longitudinal 1	320.00	270.00	2.87694	2.87681	20.00	0.325611	0.0457583	0.213
Fluids:		SlickWater_120F							
		Acid_HCl_15%_100F							
		Guar_10#_120_SP_1							
Proppants:		Brady Sand 40/70 (A)							

b) "50% pad" case scenario.

Total Clean Volume:		257,396 gallons						
Total Proppant:		335,000 lbs						
Cum. Fluid Lost:		108,674 gal						
Fracture		Gross Frac Length.ft	Proppant Cutoff Length.ft	Est Flowing Frac Length.ft	Est Inf Conductivity Length.ft	Fracture Height.ft	Average Proppant Conc.lb/ft²	Average Fracture Width.in	Max Fracture Width.in
	Transverse 5	4010.00	210.00	3.94921	3.9491	55.00	0.567527	0.209727	0.278
	Transverse 4	3070.00	160.00	3.61881	3.61864	55.00	0.353113	0.11121	0.171
	Transverse 3	4010.00	210.00	3.81	3.81	55.00	0.443807	0.148602	0.295
	Transverse 2	4010.00	160.00	3.06673	3.06651	70.00	0.24935	0.138728	0.235
	Transverse 1	650.00	110.00	3.08349	3.08332	30.00	0.261555	0.0538609	0.209
	Longitudinal 1	370.00	250.00	2.74642	2.74627	25.00	0.259544	0.0379317	0.209
Fluids:		SlickWater_120F							
		Acid_HCl_15%_100F							
		Guar_10#_120_SP_1							
Proppants:		Brady Sand 40/70 (A)							

At the same time for some clusters, pad reduction has adverse effects. **Figure 38** demonstrates that besides the overall positive effect for proppant distribution, the reduction of pad stage negatively affects proppant placement under the fracture wellbore for Cluster 3. At the same time, from **Table 6** proppant placement and fracture height of other clusters will benefit from the reduction of pad stage.

a) Base case scenario.

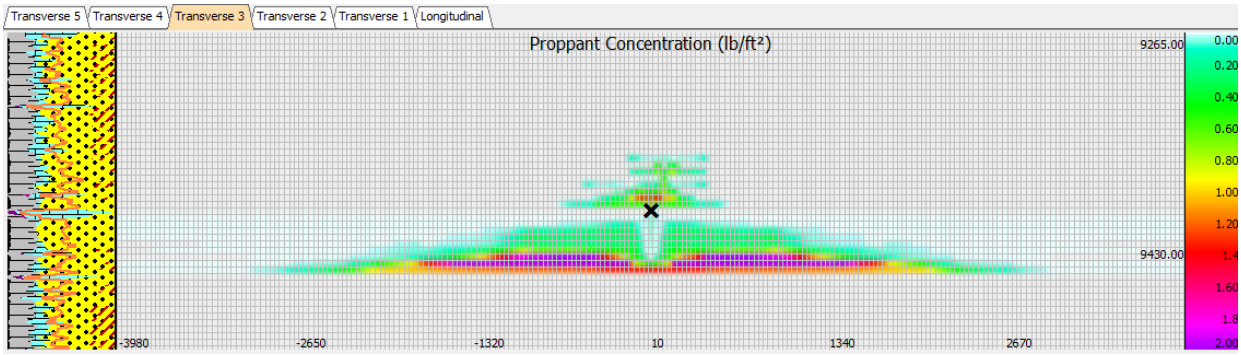

b) 50% pad case scenario.

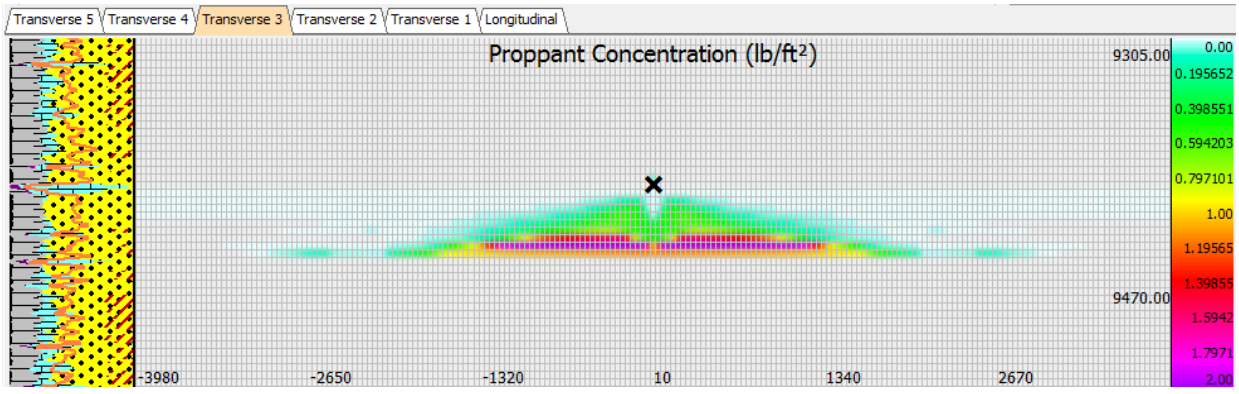

Figure 38 Proppant concentration for base case scenario a) and for "50% pad" – b). Stage 4, Cluster 3.

Fracture barriers associated with high-stress calcite-rich intervals (TVD 9,440 and 9,390 ft) limit fracture height. Therefore, a thin fluid pad cannot create any additional height for Cluster 3 out of this interval, and overall fracture conductivity has little or no benefit comparing to 50% pad scenario in **Figure 39.**

a) Base case scenario.

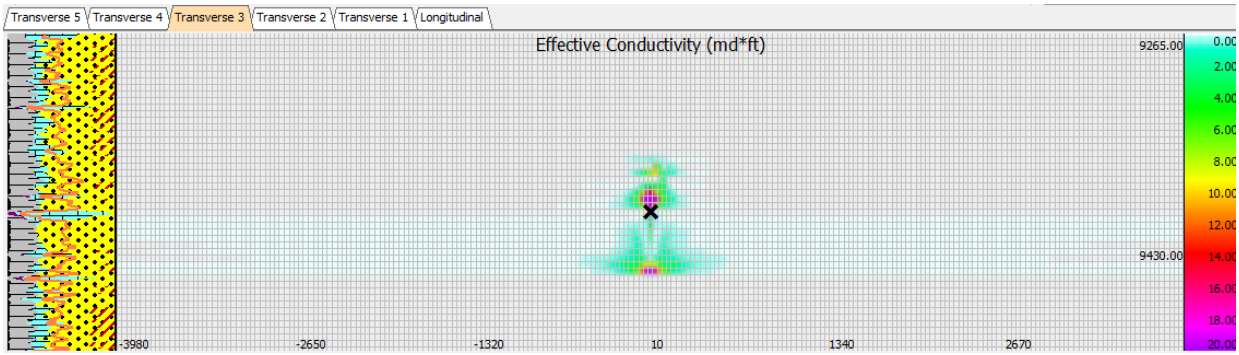

b) 50% pad case scenario.

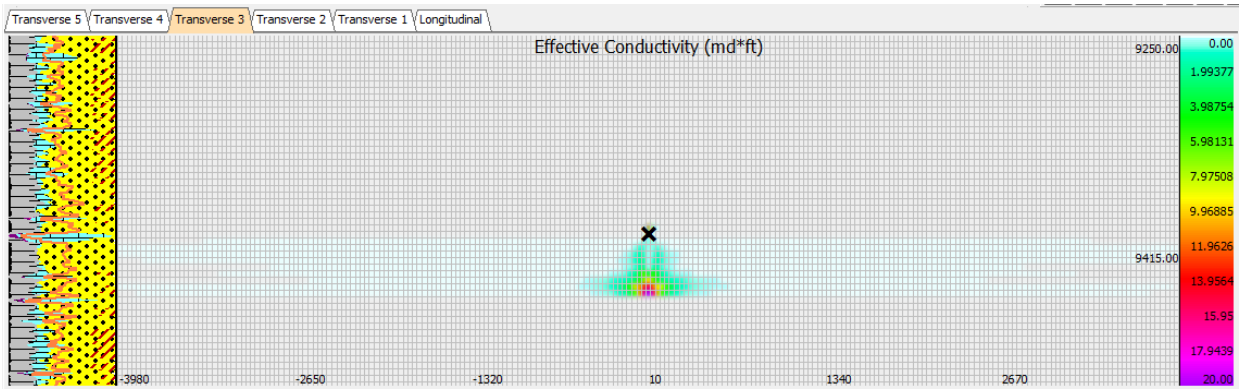

Figure 39 Effective fracture conductivity for scenario "50% pad". Stage 4, Cluster 3.

Recommendation to reduce the size of the slick water pad stage is in good agreement with Pankaj et al. (2018) for Wolfcamp completion design. Overall smaller pad stage will

benefit proppant placement for hybrid slick-water – gel stimulation because smaller resulted in length will reduce the chance of fracture hit; and reduced width and height increase fluid velocities and associated transport along the fracture length.

3.7.2. Perforation redesign for stress shadowing compensation

Stress shadowing effect is in order of hundreds of psi and may be comparable to friction losses around perforations especially for high rate designs. Therefore, it is reasonable to change the number and diameter of perforations in order to achieve similar net pressure for each simultaneously propagating fracture regardless of the difference in horizontal stresses due to mechanical interference. This technique seems to become sufficient for pad stage, but later with proppant ramp-up, the erosion of perforations will reduce possible effects of limited entry. Therefore, during the proppant ramp-up, it is preferable to use mechanical or chemical diverters.

As it was demonstrated on modeling cases and from literature review, stress shadowing cause suppression of some fractures and accelerate the growth of others. Additional stress generated by neighbor fractures promotes redistribution of proppant into the path of least resistance toward the dominant fractures. Initial geometrical design of perforations provides similar friction loss function for each cluster making uniform slurry flux unstable. To better allocate pad stage and proppant carrying slurry the engineer may vary perforation pressure loss function between clusters.

Crump and Conway (1988); Willingham et al. (1993) experimentally studied pressure losses over perforations and influence of erosion during proppant transport. Pressure losses are formulating as follows (in field units):

$$P_{perf} = \frac{0.2369 \cdot Q^2 \cdot \rho}{N_{perf}^2 \cdot d^4 \cdot C_d}$$

where C_d- an empirical coefficient of discharge in range 0.6-0.95.

For treatment conditions, assuming equal slurry rate distribution,

$$P_{perf} = \frac{0.2369 \cdot (80\ bbl/min)^2 \cdot 8.4\ lb/gal}{40^2 \cdot (0.42\ inch)^4 \cdot 0.7} = 365\ psi$$

Perforations pressure losses difference between clusters of 12 and 6 perforations/cluster, (assuming equal slurry rate per cluster):

$$\Delta P_{perf} = \frac{0.2369 \cdot 8.4\ lb/gal \cdot (16\ bbl/min)^2}{(0.42\ inch)^4 \cdot 0.7}\left(\frac{1}{36} - \frac{1}{144}\right) = 487\ psi$$

Section 3.3. demonstrates that stress shadowing between stages estimated by the dynamics of

Table 8 demonstrates the results of the simulation for the recommended perforation design. The difference between initial perforation design (8 shots per cluster in **Table 4**) with a modified one ("12-10-6-6-6") is in perforation redistribution between clusters while keeping the total number of shots the same (40 shots per stage). Comparing to the base case in **Table 4**, in the recommended design the transverse fracture from the Cluster 1 and 2 have larger fracture volume and more proppant placed.

Table 8 Simulation result with recommended perforation design ("12-10-6-6-6").

a) Base case perforation design ("8-8-8-8-8").

Perforations:	17119-17121' MD, .42" Diam, 8 Holes								
	17179-17181' MD, .42" Diam, 8 Holes								
	17239-17241' MD, .42" Diam, 8 Holes								
	17299-17301' MD, .42" Diam, 8 Holes								
	17359-17361' MD, .42" Diam, 8 Holes								
Total Clean Volume:	315,796 gallons								
Total Proppant:	335,000 lbs								
Cum. Fluid Lost:	140,836 gal								
Fracture		Gross Frac Length.ft	Proppant Cutoff Length.ft	Est Flowing Frac Length.ft	Est Inf Conductivity Length.ft	Fracture Height.ft	Average Proppant Conc.lb/ft²	Average Fracture Width.in	Max Fracture Width.in
	Transverse 5	4010.00	220.00	3.93	3.92998	55.00	0.617588	0.207	0.287
	Transverse 4	3190.00	160.00	3.59424	3.59408	55.00	0.339163	0.108676	0.17
	Transverse 3	4010.00	220.00	3.8938	3.89365	80.00	0.432663	0.163337	0.326
	Transverse 2	4010.00	160.00	2.76118	2.76093	60.00	0.161487	0.113269	0.211
	Transverse 1	590.00	110.00	2.99492	2.99474	30.00	0.291615	0.051903	0.21
	Longitudinal 1	320.00	270.00	2.87694	2.87681	20.00	0.325611	0.0457583	0.213
Fluids:	SlickWater_120F								
	Acid_HCl_15%_100F								
	Guar_10#_120_SP_1								
Proppants:	Brady Sand 40/70 (A)								

b) Modified perforation design ("12-10-6-6-6")

Perforations:	17119-17121' MD, .42" Diam, 6 Holes								
	17179-17181' MD, .42" Diam, 6 Holes								
	17239-17241' MD, .42" Diam, 6 Holes								
	17299-17301' MD, .42" Diam, 10 Holes								
	17359-17361' MD, .42" Diam, 12 Holes								
Total Clean Volume:	315,996 gallons								
Total Proppant:	335,000 lbs								
Cum. Fluid Lost:	132,439 gal								
Fracture		Gross Frac Length.ft	Proppant Cutoff Length.ft	Est Flowing Frac Length.ft	Est Inf Conductivity Length.ft	Fracture Height.ft	Average Proppant Conc.lb/ft²	Average Fracture Width.in	Max Fracture Width.in
	Transverse 5	4010.00	210.00	3.8396	3.83949	55.00	0.599524	0.20932	0.279
	Transverse 4	3400.00	170.00	3.57731	3.57714	55.00	0.371173	0.107396	0.173
	Transverse 3	4010.00	210.00	3.78986	3.78973	55.00	0.62227	0.202927	0.262
	Transverse 2	3600.00	170.00	3.90524	3.9051	40.00	0.399273	0.129559	0.231
	Transverse 1	1380.00	120.00	3.61442	3.61426	40.00	0.34443	0.085691	0.248
	Longitudinal 1	450.00	320.00	2.93598	2.93584	20.00	0.312113	0.0461202	0.133
Fluids:	SlickWater_120F								
	Acid_HCl_15%_100F								
	Guar_10#_120_SP_1								
Proppants:	Brady Sand 40/70 (A)								

At the same time, additional perforation pressure loss due to a decrease of the number of perforations in clusters 3-5 does not create a risk of screenouts, however, from the treatment pressure curve, there is an indication of begging of proppant bridging at concentrations 2.5 ppa and 3.0 ppa (starting t=80 min in **Figure 40**).

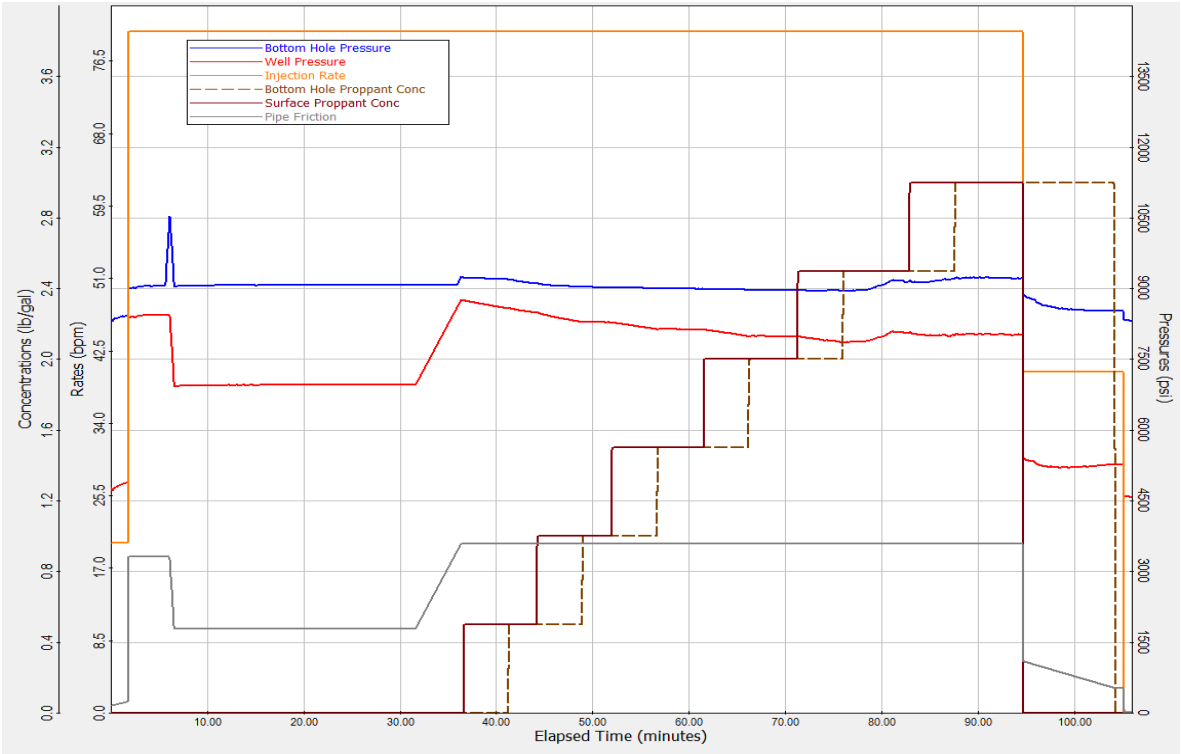

Figure 40 Modeling output for recommended perforation design ("12-10-6-6-6") for Stage 4. Starting t=80 min there is an indication of proppant bridging.

3.7.3. Small mesh proppant slugs in pad stage

Cleary et al. (1993) proposed small size proppant slugs as a remedy for near wellbore tortuosity pressure losses and to reduce the number of echelon fractures growing the cluster. Lab scale experiments show that small mesh proppant may be accumulated along dominant secondary fractures (open fissures and shear fractures) and divert fluid to smaller ones, increasing the size of stimulated rock volume and simultaneously reduce the risk of screenout as shown by Warpinski (1991), (1990) for WMX site.

Small mesh proppant will not hurt the final fracture conductivity but improve it by increasing the number of reactivated fractures and failed rock mass. By analogy to fluid loss

control materials in drilling application, use of proppant slugs in the oil-based fluid may increase the buoyancy of proppant slurry and barrier effect for pressure dependent leakoff at the fissure due to the created emulsion.

Small size proppant (100 mesh/silica flour) slugs also may reduce an adverse effect of cluster-to-cluster fluid communication at pad stage, hence making limited entry stress shadowing mitigation strategy feasible and increase the positive impact of near wellbore communication between transverse fractures and perforation clusters keeping longitudinal fractures open.

Unfortunately, to the author's best knowledge no commercial software is capable of modeling such effects directly. In GOHFER, such holdup effect is described but modeled with an empirical coefficient (Holdup coefficient). Critical Fissure Opening Pressure (CFOP) and PDL leakoff coefficients may be corrected to represent plugging of major secondary fissures. Therefore, the efficiency of the proposed recommendation needs further numerical or lab evaluation.

3.7.4. Optimization of near-wellbore fracture conductivity

As it was said in Sections 3.2, the formation permeability is an essential parameter in hydraulic fracturing design. Traditionally engineers use the dimensionless fracture conductivity concept introduced by Cinco-Ley (1982):

$$C_{fd} = \frac{k_f w_f}{k_m X_f}$$

For high values, C_{fd}>30 well productivity is driven by fracture length (infinite conductivity), whereas at C_{fd}<1.6 the productivity is driven by proppant pack width and conductivity. This

condition is applicable however for model rectangular fracture of constant conductivity, one phase pseudo-steady state flow. It is generally desirable to keep resulting fracture conductivity $C_{fd} > 2$.

Multiple numerical simulations show inefficient proppant placement laterally and vertically (e.g., **Figure 22** and **Figure 38**). The latter is essential because the highly conductive bottom part of the fracture is not connected with perforations resulting in $C_{fd} \ll 2$. For these cases it's desirable to reduce pumping rate at the end of high proppant step. This modification increases the quilibrium hight of the proppant pack close to the wellbore and reduces turbulence associated with slurry injection close to perforations.

Following calculations in Section 2.8., reduction of the pumping rate will decrease total leakoff, equilibrium fracture width and will allow proppant dunes to overfill the wellbore.

The increase of proppant volume may be considered as a direct response for small propped height. This recommendation, however, requires economic optimization.

4. PRACTICAL APPLICATIONS OF DEVELOPED MODEL*

The primary use of the developed hydraulic fracturing model is to forecast production from stimulated well and optimize the design for the next operations. Unfortunately, to the best knowledge of the author, only ResFrac code (McClure Geomechanics) is capable to couple fracture propagation problem with reservoir simulation on the same grid inside the same commercial software package. The standard industry practice is to export resulted in fracture conductivity and use it further in separate commercial or research reservoir simulator.

Based on modeled fracture conductivity, historical production of oil presented (in **Figure 41**) and water; and flux allocation from oil-soluble tracer study in Table 9, two reservoir models were built in order to identify undrained parts of the reservoir – published by Parsegov et al. (2018a) and effectiveness of surfactant EOR – published by Zhang et al. (2019).

* Part of the data reported in this chapter is reprinted with permission from "Physics-Driven Optimization of Drained Rock Volume for Multistage Fracturing: Field Example from the Wolfcamp Formation, Midland Basin" by Parsegov, S.G., Nandlal, K., Schechter, D.S., and Weijermars, R. in Proceedings of the 6th Unconventional Resources Technology Conference, 2018. Copyright 2018 by American Association of Petroleum Geologists; and from "Experimental and Numerical Studies of EOR for the Wolfcamp Formation by Surfactant Enriched Completion Fluids and Multi-Cycle Surfactant Injection" by Zhang, F., Saputra, I.W.R., Parsegov, S.G., Adel, I.A., and Schechter, D.S. in Proceedings of SPE Hydraulic Fracturing Technology Conference and Exhibition, 2019. Copyright 2019 by Society of Petroleum Engineers.

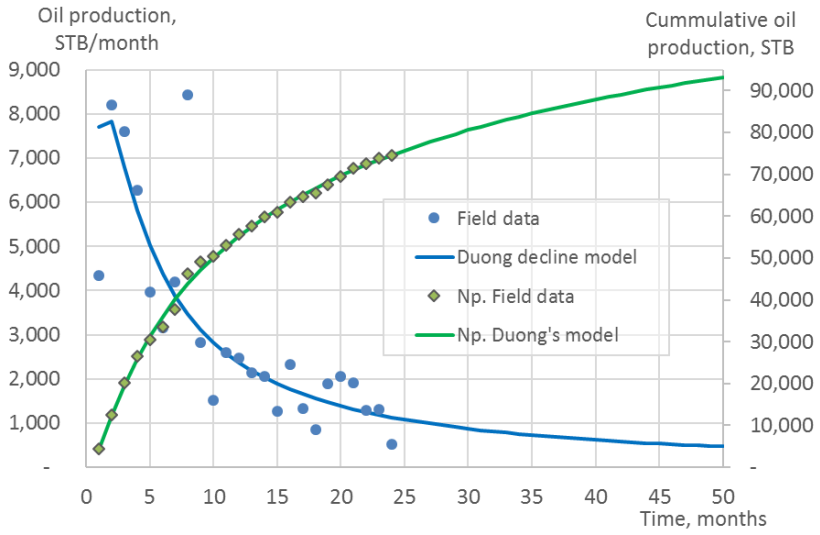

Figure 41 Actual production for the treatment well #46 and type curve forecasts used for the flow model.

Table 9 shows flux allocation between stages based on the results of oil-soluble tracers' study. For example, Stage 2 is a part of the traced segment "5-2" (Stages from 2 to 5), which contributes 13.1% of oil (3.28% per stage).

Table 9 Oil soluble tracer data for fracture stages for the treatment well. Reprinted from Parsegov et al. (2018a) with permission from URTeC, whose permission is required for further use.

	Oil Frac Tracer Concentration, ppb						
Traced Segment	30-26	25-21	20-17	16	15-11	10-6	5-2
Stim Date	7/30/14	7/27/14	7/24/14	7/24/14	7/22/14	7/20/14	7/18/14
OFT Injected (gr)	1,250	1,250	1,000	250	1,250	1,250	1,000
% Injected	17.2%	17.2%	13.8%	3.4%	17.2%	17.2%	13.8%
Sample Type	OFT 5800	OFT 5300	OFT 15010	OFT 15110	OFT 15000	OFT 5100	OFT 5500
Oil (Produced)	42.3	63.6	28.0	8.8	68.4	17.3	2.4
Oil (Produced)	33.6	49.8	26.1	8.5	58.2	13.0	2.6
Oil (Produced)	34.6	53.4	27.1	8.7	65.9	14.3	2.3
Oil (Produced)	38.5	57.7	27.8	8.4	63.5	15.3	2.7
Oil (Produced)	37.1	59.7	28.8	8.7	66.9	19.1	4.5
Oil (Produced)	40.1	65.0	28.6	8.5	69.5	24.1	5.2
Oil (Produced)	41.6	62.1	29.1	8.9	68.9	17.1	2.9
Oil (Produced)	28.8	52.0	24.5	8.0	60.0	20.5	9.7
Oil (Produced)	32.1	64.2	21.9	7.1	60.8	16.1	10.8
Oil (Produced)	39.7	64.1	30.1	9.4	76.4	23.8	12.3
Oil (Produced)	42.0	68.6	32.9	10.8	89.0	34.7	25.6
Oil (Produced)	35.3	56.3	27.6	9.3	72.8	28.3	32.3
Oil (Produced)	38.8	59.3	28.8	8.9	72.0	31.0	32.1
Oil (Produced)	39.0	43.2	21.2	13.0	70.2	21.8	28.9
Oil (Produced)	37.6	41.1	19.3	12.6	64.9	20.6	28.2
Oil (Produced)	44.5	48.6	18.6	11.6	61.2	24.8	28.2
Oil (Produced)	48.0	52.0	19.0	10.9	69.2	26.0	33.1
Oil (Produced)	24.2	27.0	15.9	6.4	52.6	15.2	49.6
Time Weighted Avg, ppb	36.8	47.7	21.5	9.2	64.5	21.8	30.3
% total ppb from Stage	15.9%	20.6%	9.3%	4.0%	27.8%	9.4%	13.1%

4.1. Single porosity semi-analytical model

From the modeled results for Stages 2 to 9 (**Figure 42**), the extreme ends of fracture stages appear to have higher velocities, due to less interference with adjacent fractures.

The highest velocities are confined to the near-axial region of the wellbore, again emphasizing how much of the created fracture length away from the near-wellbore area is unproductive. The pressure plot (**Figure 43**) suggests a large depletion region, while the time-of-flight contours after 40 years of production show the actual area drained is very small when compared to the areas that show marked pressure changes.

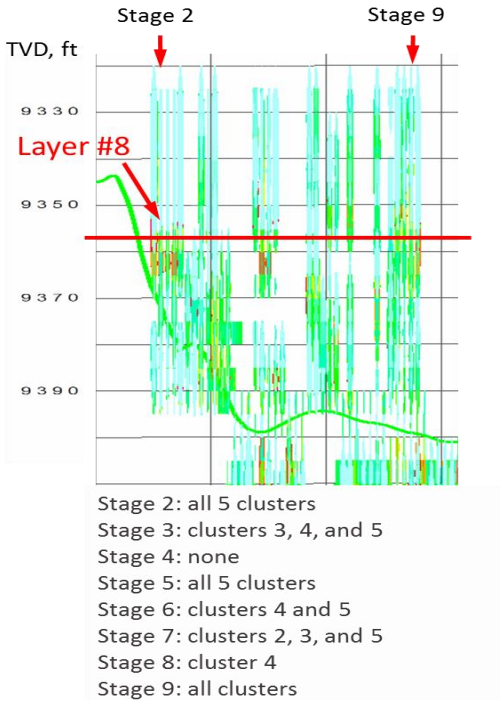

Figure 42 Side view of the proppant placement map. Layer #8 indicates the vertical position of the 2D map presented in Figure 43. Vertically exaggerated. Reprinted from Parsegov et al. (2018a) with permission from URTeC, whose permission is required for further use.

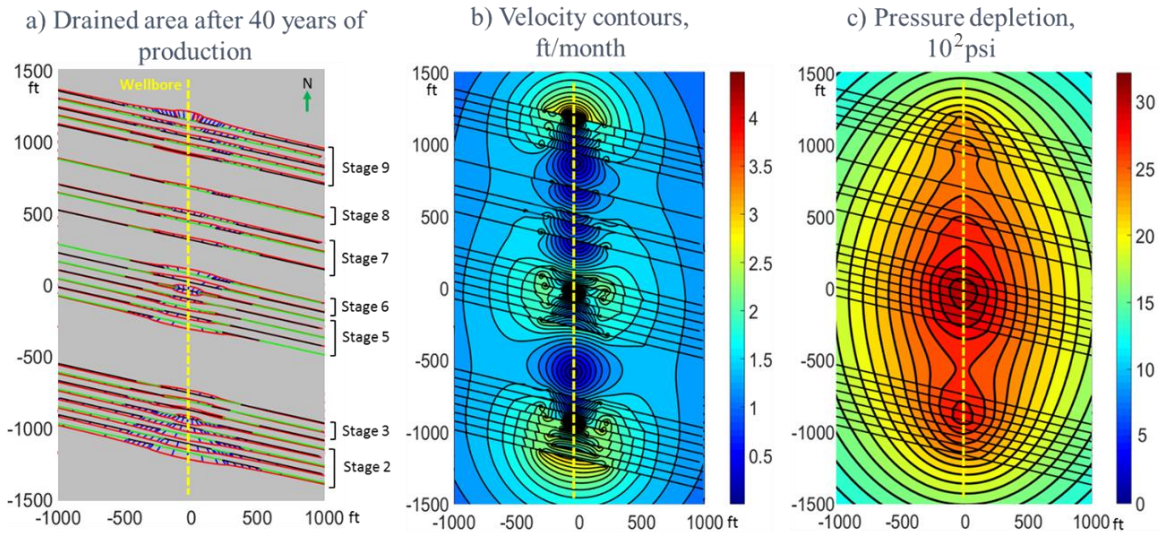

Figure 43 Map view for the drained area, Velocity contour, and Pressure depletion after 40 years of production for layer #8 shown in Figure 42. Reprinted from Parsegov et al. (2018a) with permission from URTeC, whose permission is required for further use.

4.2. Dual porosity compositional model

To reduce the computational cost of reservoir modeling and to keep in mind surprisingly uniform production based on long term tracers' study, two neighboring stages were modeled together for dual porosity fully compositional reservoir simulations.

Cropped reservoir model for 2 stages presented in Figure 44 has the dimension (X, Y, Z) of 600 ft, 2,000 ft, and 200 ft with the fracture half-length of 500 ft along the Y direction. Production and injection of surfactants were normalized accordingly. Central 2 ft wide blocks of the grid have equivalent permeability as proposed by Rubin (2010).

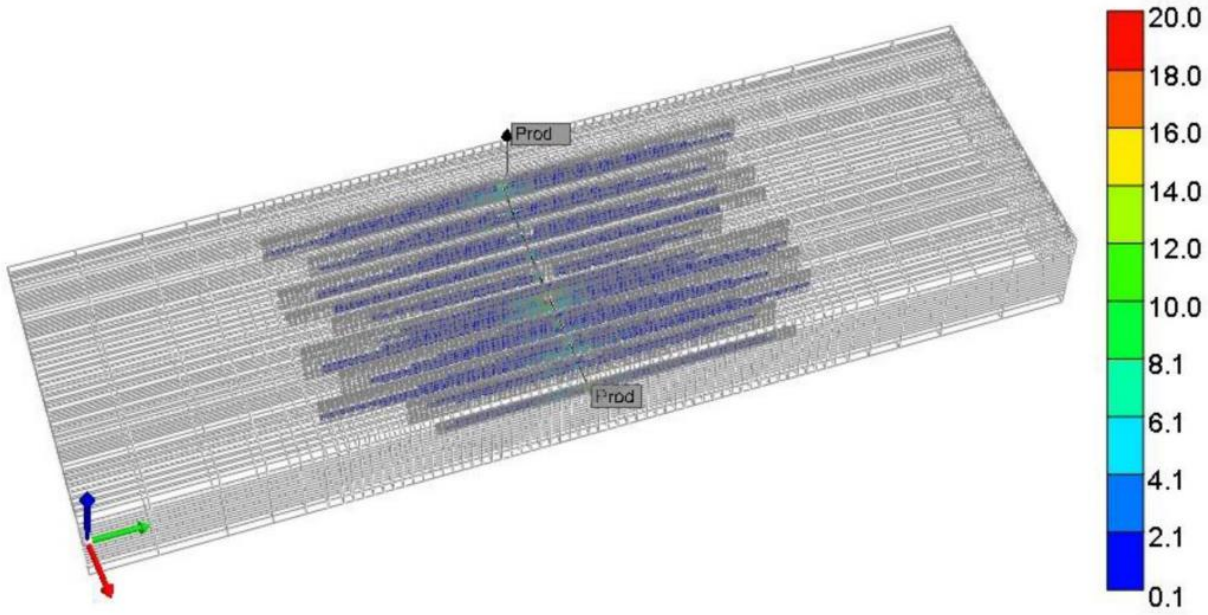

Figure 44 Equivalent permeability in the logarithmically refined grid in reservoir simulator built from hydraulic fracturing conductivity output. Reprinted with permission from Zhang et al. (2019).

Logarithmic grid refinement was done toward all fracture faces to reduce the number of required grid elements in **Figure 45**.

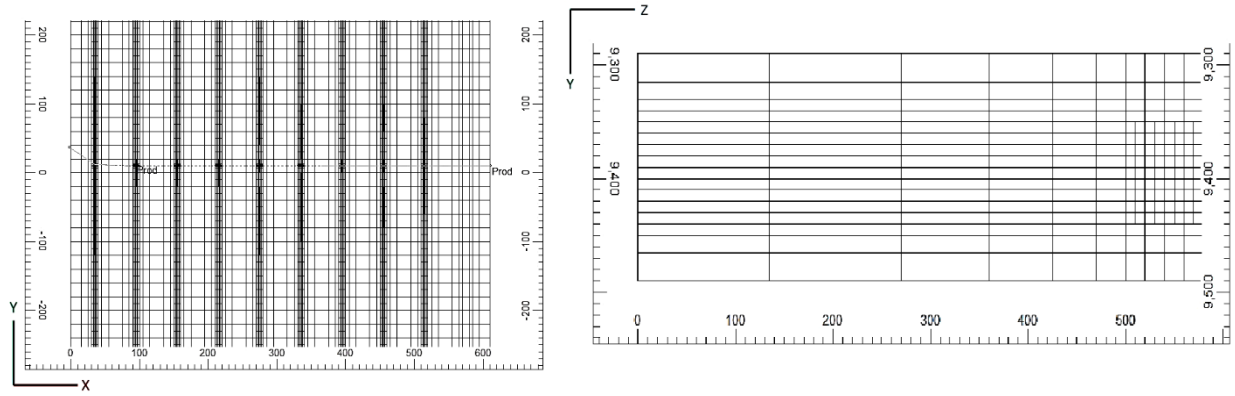

Figure 45 Logarithmic grid refinement in directions around the created grid. Reprinted with permission from Zhang et al. (2019).

Effective permeability and porosity of natural fractures were estimated based on the history matching process for oil and water production (**Figure 46**). Results are shown in **Table 10**.

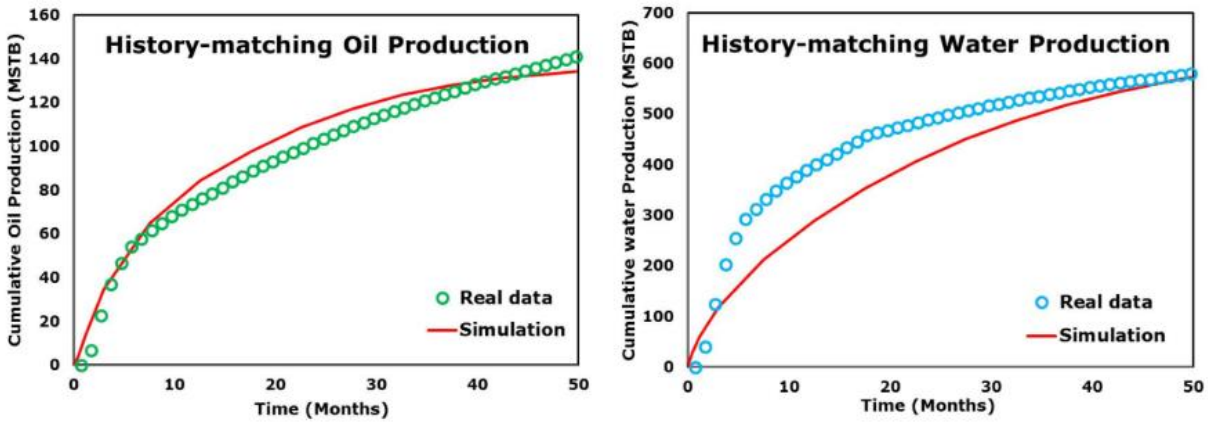

Figure 46 History matching for oil and water cumulative production of the treatment well #46. Reprinted with permission from Zhang et al. (2019).

The global error of history-matching oil production is less than 4%, and the 4-years cumulative oil production error is less than 1%. When history-matching the cumulative water production, the global error between the simulation results and the actual production data is less than 10%, and the 4-years cumulative oil production error is less than 1%.

Table 10 Reservoir properties of the field-scale model from history match. Reprinted with permission from Zhang et al. (2019).

Reservoir Property	Value	Reservoir Property	Value
Thickness (ft)	200	Hydraulic fracture half-length (ft)	500
Matrix porosity	5%	Fracture spacing (ft)	0.5
Fracture porosity	0.05%	Water saturation	0.45
Matrix permeability (nd)	150	Initial pressure (psi)	5,500
Fracture permeability (md)	0.04	Temperature (°F)	155

Based on the history-matching results, the field-scale model is capable of representing real reservoir conditions. The field-scale model provides convincing simulation results for investigating different EOR scenarios based on scaling model proposed by F. Zhang et al. (2018); Fan Zhang et al. (2018c), (2018a).

5. CONCLUSIONS

The following conclusions can be made from Chapters 1-4:

1. Operators may save a significant amount of money on dipole sonic logging by constructing 1D MEM based on correlations from triple combo logs for static Young's modulus and Poisson's ratio.
2. Based on pulse decay core measurements, a new correlation for matrix permeability was proposed for Wolfcamp formation in Midland Basin in the power-law form correlation.
3. Horizontal stress anisotropy is an important modeling parameter for any physics-based hydraulic fracturing model.
4. Lower stress anisotropy promotes open of secondary fissures and pressure dependent leakoff. Net pressure, required for tensile opening of fissures depends on their orientations as proposed Delaney et al. (1986) and may occur at pressures significantly lower than with estimation of Nolte and Smith (1981).
5. Literature coverage of horizontal stress anisotropy is limited and contradictory.
6. Breakdown pressure and ISIP escalation may be used for stress anisotropy range estimation. For the treatment well #46 horizontal stress anisotropy (ANI) may be estimated in range of 7.6-11%.
7. If stress anisotropy is inferred from inversion of microseismic moment tensor, events close to fracture tips and compression zones should be excluded. Otherwise, local strike-slip stress environment may be inferred instead of far-field stress.
8. Grid-based models are subject to scale effect and size of the grid block should be chosen as a practical balance of resolution of available data, the memory required and

computational cost. Numerical artifacts related to grid upscaling results in an overestimation of fracture width and height.

9. Multiple numerical experiments show that the vertical resolution of 5ft is a reasonable compromise. Further progress of logging tools and modeling software will make a smaller grid size feasible. At the same time, an increase of apparent fracture toughness should be included in the modeling of hydraulic fracture on fine grids.
10. Created fracture half-length is about one order of magnitude bigger than propped one due to inefficient proppant add-in design for thin fluids. Proposed design may be improved by adding proppant earlier than proposed by Nolte (1986).
11. Ineffective proppant transport in unconventional formations may be described by taking into account growth and propping of axial fractures, reactivation of natural fractures and associated local additional leakoff.
12. In order to partially mitigate the adverse effects of natural fractures the following techniques may be applied:
    - Amount of proppant increase in order to cover created fracture height. In all simulation runs the proppant pack was not able to reach equilibrium and settled in the bottom.
    - Variable pumping rate. A higher rate is beneficial to open secondary fractures and lower during proppant transport. At the same time, rate variation changes the equilibrium proppant pack height and improve proppant transport, keeping the volume of the fluid constant.
    - Use of solid diverters, 100 mesh sand (70/140 mesh) to selectively prop dominant secondary fractures.

- Geosteering the well to avoid perforation of high-stress calcite-rich intervals resulting in pitchouts and choking wellbore from the proppant pack.

13. Proposed workflow for effective fracture geometry forward modeling may be complemented with research and commercial reservoir simulators to run multiple production scenarios.

The contribution of this work is as follows:

1. A correlation for matrix permeability-effective porosity in lower Wolfcamp formation.
2. A workflow for estimation of the upper and lower limit for horizontal stress anisotropy (ANI) from breakdown pressures and ISIP escalation during the treatment.
3. Estimation of critical fissure opening pressure (CFOP) and pressure dependent leakoff (PDL) coefficient from DFN simulations.
4. Practical recommendations to reduce the size of the pad, increase the of proppant loading, perforation redesign.
5. Conductivity 2D maps for individual transverse and longitudinal fractures were proposed for reservoir simulation and modern EOR techniques assessment described by Fan Zhang et al. (2018b), (2018c).

REFERENCES

Abbas, S., Lecampion, B., Prioul, R., (2013). Competition Between Transverse And Axial Hydraulic Fractures In Horizontal Wells, in: SPE Hydraulic Fracturing Technology Conference. Society of Petroleum Engineers, pp. 4–6. https://doi.org/10.2118/163848-MS

Aderibigbe, A., Chen Valdes, C., Heidari, Z., (2016). Integrated rock classification in the Wolfcamp Shale based on reservoir quality and anisotropic stress profile estimated from well logs. Interpretation 4, SF1-SF18. https://doi.org/10.1190/INT-2015-0138.1

Agharazi, A., (2016). Determining Maximum Horizontal Stress with Microseismic Focal Mechanisms - Case Studies in the Marcellus, Eagle Ford, Wolfcamp, in: Proceedings of the 4th Unconventional Resources Technology Conference. American Association of Petroleum Geologists, Tulsa, OK, USA. https://doi.org/10.15530/urtec-2016-2461621

Alimahomed, F., Malpani, R., Jose, R., Haddad, E., Arteaga, E. V, Smith, L., Lati, S., (2017). Stacked Pay Pad Development in the Midland Basin, in: SPE Liquids-Rich Basins Conference - North America. Society of Petroleum Engineers. https://doi.org/10.2118/187496-MS

Avasthl, J.M., Nolen-Hoeksema, R.C., Al Rabaa, A.W.M., (1991). In-Situ Stress Evaluation in the McElroy Field, West Texas. SPE Form. Eval. 6, 301–309. https://doi.org/10.2118/20105-PA

Barree, R.D., (1984). Development of a numerical simulator for three-dimensional hydraulic fracture propagation in heterogeneous media. Colorado School of Mines.

Barree, R.D., Conway, M.W., (2001). Proppant Holdup, Bridging, and Screenout Behavior in Naturally Fractured Reservoirs, in: SPE Production and Operations Symposium. Society of Petroleum Engineers, p. 7. https://doi.org/10.2118/67298-MS

Barree, R.D., Cox, S.A., Gilbert, J.V., Dobson, M., (2003). Closing the Gap: Fracture Half Length from Design, Buildup, and Production Analysis, in: SPE Annual Technical Conference and Exhibition. Society of Petroleum Engineers, pp. 1–9. https://doi.org/10.2118/84491-MS

Barree, R.D., Gilbert, J.V., Conway, M., (2009). Stress and Rock Property Profiling for Unconventional Reservoir Stimulation, in: SPE Hydraulic Fracturing Technology Conference. Society of Petroleum Engineers, pp. 19–21. https://doi.org/10.2118/118703-MS

Barree, R.D., Miskimins, J.L., (2015). Calculation and Implications of Breakdown Pressures in Directional Wellbore Stimulation, in: SPE Hydraulic Fracturing Technology Conference. Society of Petroleum Engineers, p. 148–155; discussion 156. https://doi.org/10.2118/173356-MS

Barree, R.D., Mukherjee, H., (1996). Determination of Pressure Dependent Leakoff and Its Effect on Fracture Geometry, in: SPE Annual Technical Conference and Exhibition. Society of Petroleum Engineers, p. 10. https://doi.org/10.2118/36424-MS

Barree, R.D., Winterfeld, P.H., (1998). Effects of Shear Planes and Interfacial Slippage on Fracture Growth and Treating Pressures, in: SPE Annual Technical Conference and Exhibition. Society of Petroleum Engineers. https://doi.org/10.2118/48926-MS

Baumgardner, R.W., Hamlin, H.S., Rowe, H.D., (2014). High-Resolution Core Studies of Wolfcamp/Leonard Basinal Facies, Southern Midland Basin, Texas, AAPG Search and Discovery.

Bhandari, A.R., Flemings, P.B., Ramiro-Ramirez, S., Hofmann, R., Polito, P.J., (2019). Gas and liquid permeability measurements in Wolfcamp samples. Fuel 236, 1026–1036.

https://doi.org/10.1016/j.fuel.2018.09.038

Blot, M.A., Medlin, W.L., (1985). Theory of Sand Transport in Thin Fluids, in: SPE Annual Technical Conference and Exhibition. Society of Petroleum Engineers. https://doi.org/10.2118/14468-MS

Boussinesq, J., (1885). Application des potentiels à l'étude de l'équilibre et du mouvement des solides élastiques, principalement au calcul des deformations et des pressions que produisent, dans ces solides, des efforts quelconques exercés sur und petite partie de leur surface. Gauthier-Villars, Paris, France.

Bradley, W.B., (1979). Failure of inclined boreholes. J. Energy Resour. Technol. 101, 232. https://doi.org/10.1115/1.3446925

Carter, B.., Desroches, J., Ingraffea, A.R., Wawrzynek, P.A., (2000). Simulating Fully 3D Hydraulic Fracturing, in: Zaman, M., Gioda, G., Booker, J. (Eds.), Modeling in Geomechanics. Wiley Publishers, p. 730.

Casey, B., (2018). Opportunities and Geoscience Vision. Search and Discovery Article #70316, in: 2017 AAPG Southwest Section Annual Convention, Midland, Texas.

Cherian, B., Shoemaker, M., Nwoko, S., Narasimhan, S., Olaoye, O., Iqbal, J., Peacock, J., Becher, J., Ferguson, B., Zakhour, N., (2018). Understanding development drivers in horizontal wellbores in the Midland Basin. Soc. Pet. Eng. - SPE Liq. Basins Conf. - North Am. 2018, LRBC 2018.

Ciezobka, J., Courtier, J., Wicker, J., (2018). Hydraulic Fracture Test Site - Project Overview and Summary of Results. SPE/AAPG/SEG Unconv. Resour. Technol. Conf. 1–9. https://doi.org/10.15530/urtec-2018-2937168

Cinco-Ley, H., (1982). Evaluation of Hydraulic Fracturing By Transient Pressure Analysis

Methods, in: International Petroleum Exhibition and Technical Symposium. Society of Petroleum Engineers, pp. 639–665. https://doi.org/10.2118/10043-MS

Clark, J.B., (1949). A Hydraulic Process for Increasing the Productivity of Wells. J. Pet. Technol. 1, 1–8. https://doi.org/10.2118/949001-G

Cleary, M.P., Johnson, D.E., Kogsbøll, H.-H., Owens, K.A., Perry, K.F., de Pater, C.J., Stachel, A., Schmidt, H., Mauro, T., (1993). Field Implementation of Proppant Slugs To Avoid Premature Screen-Out of Hydraulic Fractures With Adequate Proppant Concentration, in: Low Permeability Reservoirs Symposium. Society of Petroleum Engineers. https://doi.org/10.2118/25892-MS

Cohen, C., Kresse, O., Weng, X., (2017). Stacked Height Model to Improve Fracture Height Growth Prediction, and Simulate Interactions With Multi-Layer DFNs and Ledges at Weak Zone Interfaces, in: SPE Hydraulic Fracturing Technology Conference and Exhibition. Society of Petroleum Engineers, pp. 1–29. https://doi.org/10.2118/184876-MS

Craft, B.C., Hawkins, M., Terry, R.E., (1991). Applied Petroleum Reservoir Engineering, Second. ed.

Craig, D., Hoang, T., Sivakumar, K., (2019). The Effect of Fracture Swarms and Finite Conductivity Fracture(s) on DFIT Analysis., in: To Be Presented at the SPE Annual Technical Conference and Exhibition. Calgary, Alberta, Canada.

Crawford, P.B., Landrum, B.L., (1955). Effect of Unsymmetrical Vertical Fractures on Production Capacity. Pet. Trans. AIME 204, 251–254.

Crawford, P.B., Landrum, B.L., (1954). Estimated Effect of Horizontal Fractures on Production Capacity, in: Fall Meeting of the Petroleum Branch of AIME. Society of Petroleum Engineers, pp. 1–8. https://doi.org/10.2118/414-G

Crouch, S.L., Starfield, A.M., (1983). Boundary element methods in solid mechanics: With applications in rock mechanics and geological engineering. George Allen & Unwin, London.

Crump, J.B., Conway, M.W., (1988). Effects of Perforation-Entry Friction on Bottomhole Treating Analysis. J. Pet. Technol. 40, 1041–1048. https://doi.org/10.2118/15474-PA

Daines, S.R., (1982). Prediction of Fracture Pressures for Wildcat Wells. J. Pet. Technol. 34, 863–872. https://doi.org/10.2118/9254-PA

Daneshy, A., (2019). Three-Dimensional Analysis of Interactions Between Hydraulic and Natural Fractures, in: SPE Hydraulic Fracturing Technology Conference and Exhibition. Society of Petroleum Engineers. https://doi.org/10.2118/194335-MS

Daneshy, A.A., (1973). A Study of Inclined Hydraulic Fractures. Soc. Pet. Eng. J. 13, 61–68. https://doi.org/10.2118/4062-PA

Daniels, J.L., Waters, G.A., Le Calvez, J.H., Bentley, D., Lassek, J.T., (2007). Contacting More of the Barnett Shale Through an Integration of Real-Time Microseismic Monitoring, Petrophysics, and Hydraulic Fracture Design, in: SPE Annual Technical Conference and Exhibition. Society of Petroleum Engineers. https://doi.org/10.2118/110562-MS

Delaney, P.T., Pollard, D.D., Ziony, J.I., McKee, E.H., (1986). Field relations between dikes and joints: Emplacement processes and paleostress analysis. J. Geophys. Res. 91, 4920. https://doi.org/10.1029/JB091iB05p04920

Dohmen, T., Zhang, J., Blangy, J., (2014). Measurement and Analysis of 3D Stress Shadowing Related to the Spacing of Hydraulic Fracturing in Unconventional Reservoirs, in: SPE Annual Technical Conference and Exhibition. Society of Petroleum Engineers, Amsterdam, The Netherlands. https://doi.org/10.2118/170924-MS

Dommisse, R., Sivila, L., Male, F., Hamlin, H.S., (2018). The Value of Building a Multiscale, Regional Geomodel for Reserves Assessment of the Midland Basin, in: Proceedings of the 6th Unconventional Resources Technology Conference. American Association of Petroleum Geologists, Tulsa, OK, USA, pp. 1–11. https://doi.org/10.15530/urtec-2018-2902841

Dutton, S.P., Kim, E.M., Broadhead, R.F., Raatz, W.D., Breton, C.L., Ruppel, S.C., Kerans, C., (2005). Play analysis and leading-edge oil-reservoir development methods in the Permian basin: Increased recovery through advanced technologies. Am. Assoc. Pet. Geol. Bull. 89, 553–576. https://doi.org/10.1306/12070404093

Eaton, B.A., (1969). Fracture Gradient Prediction and Its Application in Oilfield Operations. J. Pet. Technol. 21, 1353–1360. https://doi.org/10.2118/2163-PA

Economides, M.J., Hill, D.A., Ehlig-Economides, C., Zhu, D., (2002). Petroleum Production Systems, 2nd ed. Prentice Hall.

Edwards, K.L., Weissert, S., Jackson, J.B., Marcotte, D., (2011). Marcellus Shale Hydraulic Fracturing And Optimal Well Spacing To Maximize Recovery And Control Costs, in: SPE Hydraulic Fracturing Technology Conference. Society of Petroleum Engineers, p. SPE 140463. https://doi.org/10.2118/140463-MS

Eissa, E.A., Kazi, A., (1988). Relation between static and dynamic Young's moduli of rocks. Int. J. Rock Mech. Min. Sci. 25, 479–482. https://doi.org/10.1016/0148-9062(88)90987-4

Elkateb, T., Chalaturnyk, R., Robertson, P.K., (2003). An overview of soil heterogeneity: quantification and implications on geotechnical field problems. Can. Geotech. J. 40, 1–15. https://doi.org/10.1139/t02-090

Fisher, M.K., Heinze, J.R., Harris, C.D., Davidson, B.M., Wright, C. a., Dunn, K.P., (2004).

Optimizing Horizontal Completion Techniques in the Barnett Shale Using Microseismic Fracture Mapping. SPE Annu. Tech. Conf. Exhib. https://doi.org/10.2118/90051-MS

Fisher, M.K., Wright, C.A., Davidson, B.M., Goodwin, A.K., Fielder, E.O., Buckler, W.S., Steinsberger, N.P., (2002). Integrating Fracture Mapping Technologies to Optimize Stimulations in the Barnett Shale, in: SPE Annual Technical Conference and Exhibition. Society of Petroleum Engineers, San Antonio, Texas, USA. https://doi.org/10.2118/77441-MS

Friedrich, M., Monson, G., (2013). Two Practical Methods to Determine Pore Pressure Regimes in the Spraberry and Wolfcamp Formations in the Midland Basin, in: Unconventional Resources Technology Conference, Denver, Colorado, 12-14 August 2013. Society of Exploration Geophysicists, American Association of Petroleum Geologists, Society of Petroleum Engineers, pp. 2475–2486. https://doi.org/10.1190/urtec2013-258

Frocht, M.M., (1941). Photoelasticity vol.1. John Willey&Sons, New York, NY.

Fung, R.L., Vilayakumar, S., Cormack, D.E., (1987). Calculation of Vertical Fracture Containment in Layered Formations. SPE Form. Eval. 2, 518–522. https://doi.org/10.2118/14707-PA

Gale, J.F.W., Elliott, S.J., Laubach, S.E., (2018). Hydraulic Fractures in Core From Stimulated Reservoirs: Core Fracture Description of HFTS Slant Core, Midland Basin, West Texas. Proc. 6th Unconv. Resour. Technol. Conf. https://doi.org/10.15530/urtec-2018-2902624

Germanovich, L.N., Astakhov, D.K., (2004). Fracture closure in extension and mechanical interaction of parallel joints. J. Geophys. Res. Solid Earth 109, 1–22. https://doi.org/10.1029/2002JB002131

Grechka, V., Li, Z., Howell, B., Garcia, H., Wooltorton, T., (2017). High-resolution

microseismic imaging. Lead. Edge 36, 822–828. https://doi.org/10.1190/tle36100822.1

Gretener, P.E., (1965). Can the state of stress be determined from hydraulic fracturing data? J. Geophys. Res. 70, 6205–6212. https://doi.org/10.1029/JZ070i024p06205

Griffith, A.A.“., (1924). Theory of rupture, in: Proceedings of the First International Congress for Applied Mechanics. Delft, p. 55.

Griffith, A.A., (1921). The Phenomena of Rupture and Flow in Solids. Philos. Trans. R. Soc. A Math. Phys. Eng. Sci. 221, 163–198. https://doi.org/10.1098/rsta.1921.0006

Gruesbeck, C., Collins, R.E., (1982). Particle Transport Through Perforations. Soc. Pet. Eng. J. 22, 857–865. https://doi.org/10.2118/7006-PA

Guidry, K., Luffel, D., Curtis, J., (1996). Development of Laboratory and Petrophysical Techniques for Evaluating Shale Reservoirs - Final Technical Report. GRI-95/0496.

Hamlin, H.S., Baumgardner, R.W., (2012). Wolfberry Play, Midland Basin, West Texas. Search Discov. 10419, 3pp.

Hamza, F., Chen, C., Gu, M., Quirein, J., Martysevich, V., Matzar, L., (2018). Characterization of Anisotropic Elastic Moduli and Stress for Unconventional Reservoirs Using Laboratory Static and Dynamic Geomechanical Data (includes associated erratum). SPE Reserv. Eval. Eng. 21, 392–404. https://doi.org/10.2118/175907-PA

Han, G., (2017). Highlights from Hydraulic Fracturing Community : from Physics to Modelling, in: URTeC 2768686.

Havens, J.B., Batzle, M.L., (2011). Minimum Horizontal Stress in the Bakken Formation. Am. Rock Mech. Assoc. 11–322, 1–6.

Heidbach, O., Rajabi, M., Reiter, K., Ziegler, M., Team, W., (2016). World Stress Map Database Release 2016. GFZ Data Serv. https://doi.org/10.5880/WSM.2016.001

Hossain, M.M., Rahman, M.K., Rahman, S.S., (1999). A Comprehensive Monograph for Hydraulic Fracture Initiation From Deviated Wellbores Under Arbitrary Stress Regimes. SPE Asia Pacific Oil Gas Conf. Exhib. https://doi.org/10.2118/54360-MS

Howard, G.C., Fast, C.R., (1957). Optimum Fluid Characteristics for Fracture Extension., in: Sprlig Meeting of the Midcontinent District, Disvision of Production. Tulsa, OK, USA.

Huang, J., Griffiths, D.V., Wong, S.-W., (2011). In situ stress determination from inversion of hydraulic fracturing data. Int. J. Rock Mech. Min. Sci. 48, 476–481. https://doi.org/10.1016/j.ijrmms.2010.08.018

Hubbert, M.K., Willis, D.G.G., (1957). Mechanics Of Hydraulic Fracturing. Pet. Trans. AIME 210, 153–163.

Jones, S.C., (1997). A Technique for Faster Pulse-Decay Permeability Measurements in Tight Rocks. SPE Form. Eval. 12, 19–26. https://doi.org/10.2118/28450-PA

Kehle, R.O., (1964). The determination of tectonic stresses through analysis of hydraulic well fracturing. J. Geophys. Res. 69, 259–273. https://doi.org/10.1029/JZ069i002p00259

Kern, L.R., Perkins, T.K., Wyant, R.E., (1959). The Mechanics of Sand Movement in Fracturing. J. Pet. Technol. 11, 55–57. https://doi.org/10.2118/1108-G

Ketter, A. a, Daniels, J.L., Heinze, J.R., Waters, G., (2008). A Field Study in Optimizing Completion Strategies for Fracture Initiation in Barnett Shale Horizontal Wells. SPE Prod. Oper. 23, 373–378. https://doi.org/10.2118/103232-PA

Khristianovic, S.A., Zheltov, Y.P., (1955). Formation of Vertical Fractures by Means of Highly Viscous Liquid. Proceeding 4th World Pet. Congr.

Kirsch, E.G., (1898). Die Theorie der Elastizität und die Bedürfnisse der Festigkeitslehre. Zeitschrift des Vereines Dtsch. Ingenieure 42, 797–807.

Kresse, O., Cohen, C., Weng, X., Wu, R., Gu, H., (2011). Numerical Modeling of Hydraulic Fracturing in Naturally Fractured Formations, in: 45th US Rock Mechanics / Geomechanics Symposium. Society of Petroleum Engineers, pp. 61–68.

Kresse, O., Weng, X., Gu, H., Wu, R., (2013). Numerical Modeling of Hydraulic Fractures Interaction in Complex Naturally Fractured Formations. Rock Mech. Rock Eng. 46, 555–568. https://doi.org/10.1007/s00603-012-0359-2

Kuang, W., Zoback, M., Zhang, J., (2017). Estimating geomechanical parameters from microseismic plane focal mechanisms recorded during multistage hydraulic fracturing. Geophysics 82, KS1-KS11. https://doi.org/10.1190/geo2015-0691.1

Lacy, L.L., (1997). Dynamic Rock Mechanics Testing for Optimized Fracture Designs, in: SPE Annual Technical Conference and Exhibition. Society of Petroleum Engineers. https://doi.org/10.2118/38716-MS

Lecampion, B., Desroches, J., (2014). Simultaneous initiation of multiple transverse hydraulic frac- tures from a horizontal well. Arma 14–7110.

Liu, S., Valkó, P.P., (2017). A Rigorous Hydraulic-Fracture Equilibrium-Height Model for Multilayer Formations. SPE Prod. Oper. https://doi.org/10.2118/173335-PA

Loughry, D., Epps, D., Forrest, J., (2015). Using Pad ISIP, DFIT, and ESP Data to Generate a Pore Pressure Model for the Midland Basin, in: Proceedings of the 3rd Unconventional Resources Technology Conference. American Association of Petroleum Geologists, Tulsa, OK, USA. https://doi.org/10.15530/urtec-2015-2162973

Luffel, D.L., Hopkins, C.W., Schettler, P.D., (1993). Matrix Permeability Measurement of Gas Productive Shales, in: SPE Annual Technical Conference and Exhibition. Society of Petroleum Engineers. https://doi.org/10.2118/26633-MS

Mahrer, K.D., (1999). A review and perspective on far-field hydraulic fracture geometry studies. J. Pet. Sci. Eng. 24, 13–28. https://doi.org/10.1016/S0920-4105(99)00020-0

Maity, D., Ciezobka, J., Eisenlord, S., (2018). Assessment of In-situ Proppant Placement in SRV Using Through-Fracture Core Sampling at HFTS. Proc. 6th Unconv. Resour. Technol. Conf. 1–16. https://doi.org/10.15530/urtec-2018-2902364

Manchanda, R., Roussel, N.P., Sharma, M.M., (2012). Factors Influencing Fracture Trajectories and Fracturing Pressure Data in a Horizontal Completion, in: 46th US Rock Mechanics / Geomechanics Symposium. ARMA 12-633. Chicago, IL, USA.

Mathur, A., Sondergeld, C.H., Rai, C.S., (2016). Comparison of Steady-State and Transient Methods for Measuring Shale Permeability. SPE Low Perm Symp. https://doi.org/10.2118/180259-MS

Mavko, G., Mukerji, T., Dvorkin, J., (2009). The Rock Physics Handbook. Cambridge University Press, Cambridge. https://doi.org/10.1017/CBO9780511626753

McClure, M., Babazadeh, M., Shiozawa, S., Huang, J., (2015). Fully Coupled Hydromechanical Simulation of Hydraulic Fracturing in Three-Dimensional Discrete Fracture Networks, in: SPE Hydraulic Fracturing Technology Conference. Society of Petroleum Engineers. https://doi.org/10.2118/173354-MS

Mcclure, M., Kang, C., (2018). ResFrac Technical Writeup.

McClure, M.W., (2012). Modeling and Characterization of Hydraulic Stimulation and Induced Seismicity in Geothermal and Shale Gas Reservoirs, SGP-TR-199.

McClure, M.W., Horne, R.N., (2011). Investigation of injection-induced seismicity using a coupled fluid flow and rate/state friction model. GEOPHYSICS 76, WC181-WC198. https://doi.org/10.1190/geo2011-0064.1

McClure, M.W., Jung, H., Cramer, D.D., Sharma, M.M., (2016). The Fracture-Compliance Method for Picking Closure Pressure From Diagnostic Fracture-Injection Tests (see associated supplementary discussion/reply). SPE J. 21, 1321–1339. https://doi.org/10.2118/179725-PA

McClure, M.W., Zoback, M.D., (2013). Computational investigation of trends in initial shut-in pressure during multi-stage hydraulic stimulation in the Barnett Shale. 47th US Rock Mech. / Geomech. Symp. 2013 2, 902–916.

Medlin, W.L., Sexton, J.H., Zumwalt, G.L., (1985). Sand Transport Experiments in Thin Fluids, in: SPE Annual Technical Conference and Exhibition. Society of Petroleum Engineers. https://doi.org/10.2118/14469-MS

Meyer, B.R., Bazan, L.W., (2011). A Discrete Fracture Network Model for Hydraulically Induced Fractures - Theory, Parametric and Case Studies, in: SPE Hydraulic Fracturing Technology Conference. Society of Petroleum Engineers. https://doi.org/10.2118/140514-MS

Morales, R.H., Marcinew, R.P., (1993). Fracturing of High-Permeability Formations: Mechanical Properties Correlations, in: Proceedings of SPE Annual Technical Conference and Exhibition. Society of Petroleum Engineers, pp. 467–475. https://doi.org/10.2523/26561-MS

Mullen, M.J., Roundtree, R., Turk, G.A., (2007). A Composite Determination of Mechanical Rock Properties for Stimulation Design (What to Do When You Don’t Have a Sonic Log), in: Rocky Mountain Oil & Gas Technology Symposium. Society of Petroleum Engineers, pp. 1–13. https://doi.org/10.2118/108139-MS

Narasimhan, S., Mainali, P., Rowe, H., Morrell, A., Benson, A., Ganser, N., Arrington, S.,

(2017). Constructing High Resolution, Inch Scale Continuous Logs via a Multi Domain Approach to Improve Hydraulic Fracturing by Capturing Thin Beds in Bone Spring, Delaware Basin, Reeves County, TX, in: Proceedings of the 5th Unconventional Resources Technology Conference. American Association of Petroleum Geologists, Tulsa, OK, USA. https://doi.org/10.15530/urtec-2017-2670758

Ning, X., (1992). The measurement of matrix and fracture properties in naturally fractured low permeability cores using a pressure pulse method. Society of Petroleum Engineers. https://doi.org/10.2118/25898-MS

Niu, G., Sun, J., Parsegov, S., Schechter, D., (2017). Integration of Core Analysis, Pumping Schedule and Microseismicity to Reduce Uncertainties of Production Performance of Complex Fracture Networks for Multi-Stage Hydraulically Fractured Reservoirs, in: SPE Eastern Regional Meeting. Society of Petroleum Engineers, Lexington, Kentucky, USA. https://doi.org/10.2118/187524-MS

Nolen-Hoeksema, R.C., Avasthi, J.M., Pape, W.C., El Rabaa, A.W.M., (1994). Waterflood Improvement in the Permian Basin: Impact of In-Situ-Stress Evaluations. SPE Reserv. Eng. 9, 254–260. https://doi.org/10.2118/24873-PA

Nolte, K.G., (1986). Determination of Proppant and Fluid Schedules From Fracturing-Pressure Decline. SPE Prod. Eng. 1, 255–265. https://doi.org/10.2118/13278-PA

Nolte, K.G., Smith, M.B., (1981). Interpretation of Fracturing Pressures. J. Pet. Technol. 33, 1767–1775. https://doi.org/10.2118/8297-PA

Olson, J.E., (2008). Multi-fracture propagation modeling: Applications to hydraulic fracturing in shales and tight gas sands., in: The 42nd U.S. Rock Mechanics Symposium (USRMS). San Francisco, California.

Olson, J.E., Taleghani, A.D., (2009). Modeling simultaneous growth of multiple hydraulic fractures and their interaction with natural fractures. SPE Hydraul. Fract. Technol. Conf. https://doi.org/10.2118/119739-MS

Pankaj, P., Morrell, J.C., Pope, T., Maguire, M., Gray, D., Smith, M., Greenwald, J., Ajisafe, F., Li, J., Fan, L., Zheng, W., Judd, T., (2018). Introducing Hydraulic Fracture Heat Maps: Deriving Completion Changes to Increase Production in the Wolfcamp Formation, in: SPE Annual Technical Conference and Exhibition. Society of Petroleum Engineers. https://doi.org/10.2118/191442-MS

Parsegov, S.G., Nandlal, K., Schechter, D.S., Weijermars, R., (2018a). Physics-Driven Optimization of Drained Rock Volume for Multistage Fracturing: Field Example from the Wolfcamp Formation, Midland Basin, in: Proceedings of the 6th Unconventional Resources Technology Conference. American Association of Petroleum Geologists, Tulsa, OK, USA. https://doi.org/10.15530/urtec-2018-2879159

Parsegov, S.G., Niu, G., Schechter, D.S., Laprea-Bigott, M., (2018b). Benefits of Engineering Fracture Design. Lessons Learned from Underperformers in the Midland Basin., in: SPE Hydraulic Fracturing Technology Conference and Exhibition. Society of Petroleum Engineers, The Woodlands, Texas, USA. https://doi.org/10.2118/189859-MS

Parsegov, S.G., Schechter, D.S., (2017). Mudstone Nanoindentation — How Little Cuttings can Make a Big Difference, in: Gulf Coast Association of Geological Societies Transactions. Gulf Coast Association of Geological Societies (GCAGS) Transactions, San Antonio, TX, pp. 477–480.

Passey, Q.R., Bohacs, K., Esch, W.L., Klimentidis, R., Sinha, S., (2010). From Oil-Prone Source Rock to Gas-Producing Shale Reservoir - Geologic and Petrophysical

Characterization of Unconventional Shale Gas Reservoirs, in: International Oil and Gas Conference and Exhibition in China. Society of Petroleum Engineers, pp. 740–741. https://doi.org/10.2118/131350-MS

Patankar, N.. A., Joseph, D.. D., Wang, J., Barree, R.. D., Conway, M., Asadi, M., Joseph, D.. D., Patankar, N.. A., Conway, M., Barree, R.. D., (2002). Power law correlations for sediment transport in pressure driven channel flows. Int. J. Multiph. Flow 28, 1269–1292. https://doi.org/10.1016/S0301-9322(02)00030-7

Patterson, R.A., (2017). Characterizing Complex Fracture Geometry Through Data. Texas A&M University.

Peirce, A.P., Siebrits, E., (2001). Uniform asymptotic approximations for accurate modeling of cracks in layered elastic media. Int. J. Fract. 110, 205–239. https://doi.org/10.1023/A:1010861821959

Perkins, T.K., Kern, L.R., (1961). Widths of Hydraulic Fractures. J. Pet. Technol. 13, 937–949. https://doi.org/10.2118/89-PA

Pollard, D.D., Segall, P., Delaney, P.T., (1982). Formation and interpretation of dilatant echelon cracks. Geol. Soc. Am. Bull. 93, 1291. https://doi.org/10.1130/0016-7606(1982)93<1291:FAIODE>2.0.CO;2

Raterman, K.T., Farrell, H.E., Mora, O.S., Janssen, A.L., Gomez, G.A., Busetti, S., Mcewen, J., Davidson, M., Friehauf, K., Rutherford, J., Reid, R., Jin, G., Roy, B., Warren, M., (2017). Sampling a Stimulated Rock Volume: An Eagle Ford Example. Unconv. Resour. Technol. Conf. 24–26. https://doi.org/10.15530/urtec-20172670034

Ray, B., Lewis, C., Martysevich, V., Shetty, D.A., Walters, H.G., Bai, J., Ma, J., (2017). An Investigation into Proppant Dynamics in Hydraulic Fracturing, in: SPE Hydraulic

Fracturing Technology Conference and Exhibition. Society of Petroleum Engineers. https://doi.org/10.2118/184829-MS

Renshaw, C.E., Pollard, D.D., (1995). An experimentally verified criterion for propagation across unbounded frictional interfaces in brittle, linear elastic materials. Int. J. Rock Mech. Min. Sci. Geomech. Abstr. 32, 237–249. https://doi.org/10.1016/0148-9062(94)00037-4

Roberts, E.A.L., (1866). Improvement in method of increasing capacity of oil-wells.

Roundtree, R., Eberhard, M.J., Barree, R.D., (2009). Horizontal, Near-Wellbore Stress Effects on Fracture Initiation. SPE Rocky Mt. Pet. Technol. Conf. 14–16. https://doi.org/10.2118/123589-MS

Roussel, N.P., (2017). Analyzing ISIP Stage-by-Stage Escalation to Determine Fracture Height and Horizontal-Stress Anisotropy, in: SPE Hydraulic Fracturing Technology Conference and Exhibition. Society of Petroleum Engineers. https://doi.org/10.2118/184865-MS

Rubin, B., (2010). Accurate Simulation of Non Darcy Flow in Stimulated Fractured Shale Reservoirs, in: SPE Western Regional Meeting. Society of Petroleum Engineers. https://doi.org/10.2118/132093-MS

Rutledge, J., Leaney, S., Best, J., Craven, M., Swafford, L., (2018). High-resolution microseismic source locations and moment tensor solutions from the Permian Basin, in: SEG International Exposition and Annual Meeting. Anaheim, California, USA, pp. 3022–3026.

Sack, R.A., (1946). Extension of Griffith's theory of rupture to three dimensions. Proc. Phys. Soc. 58, 729–736. https://doi.org/10.1088/0959-5309/58/6/312

Schechter, R.S., (1991). Oil Well Stimulation. Prentice Hall.

Settari, A., Cleary, M.P., (1986). Development and Testing of a Pseudo-Three-Dimensional

Model of Hydraulic Fracture Geometry. SPE Prod. Eng. 1, 449–466. https://doi.org/10.2118/10505-PA

Shapiro, S. a., Huenges, E., Borm, G., (1997). Estimating the crust permeability from fluid-injection-induced seismic emission at the KTB site. Geophys. J. Int. 131, F15–F18. https://doi.org/10.1111/j.1365-246X.1997.tb01215.x

Shapiro, S.A., (2015). Fluid-Induced Seismicity. Cambridge University Press, Cambridge. https://doi.org/10.1017/CBO9781139051132

Shapiro, S.A., Dinske, C., (2009). Fluid-induced seismicity: Pressure diffusion and hydraulic fracturing. Geophys. Prospect. 57, 301–310. https://doi.org/10.1111/j.1365-2478.2008.00770.x

Shelokov, V., Sarkar, M., Wydrinski, R., (2017). Geomechanical Facies Model for Wolfcamp Formation (Midland Basin), in: Proceedings of the 5th Unconventional Resources Technology Conference. American Association of Petroleum Geologists, Tulsa, OK, USA, pp. 24–26. https://doi.org/10.15530/urtec-2017-2694220

Shetty, D.A., Lin, A., (2014). A Fast Parallel Coupled Hydraulic Fracture Simulator, in: Abu Dhabi International Petroleum Exhibition and Conference. Society of Petroleum Engineers, pp. 10–13. https://doi.org/10.2118/171902-MS

Shlyapobersky, J., Walhaug, W.., Sheffield, R.E., Huckabee, P.T., (1988). Field Determination of Fracturing Parameters, for Overpressure Calibrated Design of Hydraulic Fracturing. SPE Annu. Tech. Conf. Exhib. https://doi.org/10.2118/18195-MS

Shoemaker, M., Narasimhan, S., Quimby, S., Hawkins, J., (2019). Calculating far-field anisotropic stress from 3D seismic in the Permian Basin. Lead. Edge 38, 96–105. https://doi.org/10.1190/tle38020096.1

Simonson, E.R., Abou-Sayed, A.S., Clifton, R.J., (1978). Containment of Massive Hydraulic Fractures. Soc. Pet. Eng. J. 18, 27–32. https://doi.org/10.2118/6089-PA

Simpson, R.W., (1997). Quantifying Anderson's fault types. J. Geophys. Res. Solid Earth 102, 17909–17919. https://doi.org/10.1029/97JB01274

Smith, M.B., Bale, A.B., Britt, L.K., Klein, H.H., Siebrits, E., Dang, X., (2001). Layered Modulus Effects on Fracture Propagation, Proppant Placement, and Fracture Modeling, in: SPE Annual Technical Conference and Exhibition. Society of Petroleum Engineers, p. 14. https://doi.org/10.2118/71654-MS

Smith, M.B., Montgomery, C.T., (2015). Hydraulic Fracturing, 1st ed. Taylor & Francis Group, LLC.

Sneddon, I.N., (1946). The Distribution of Stress in the Neighbourhood of a Crack in an Elastic Solid. Proc. R. Soc. A Math. Phys. Eng. Sci. 187, 229–260. https://doi.org/10.1098/rspa.1946.0077

Snee, J.-E.L., Zoback, M.D., (2018). State of stress in the Permian Basin, Texas and New Mexico: Implications for induced seismicity. Lead. Edge 37, 127–134. https://doi.org/10.1190/tle37020127.1

Sondergeld, C.H., Ambrose, R.J., Rai, C.S., Moncrieff, J., (2010). Micro-Structural Studies of Gas Shales, in: SPE Unconventional Gas Conference. Society of Petroleum Engineers. https://doi.org/10.2118/131771-MS

Suarez-Rivera, R., Deenadayalu, C., Chertov, M., Hartanto, R.N., Gathogo, P., Kunjir, R., (2011). Improving Horizontal Completions on Heterogeneous Tight Shales. Can. Unconv. Resour. Conf. 21. https://doi.org/10.2118/146998-MS

Suarez-Rivera, R., Green, S.J., McLennan, J., Bai, M., (2006). Effect of Layered Heterogeneity

on Fracture Initiation in Tight Gas Shales. SPE Annu. Tech. Conf. Exhib. https://doi.org/10.1002/marc.200800230

Svatek, K.J. (Barree and A., (2017). GOHFER 3D User Manual.

Tölke, J., Baldwin, C., Mu, Y., Derzhi, N., Fang, Q., Grader, A., Dvorkin, J., (2010). Computer simulations of fluid flow in sediment: From images to permeability. Lead. Edge 29, 68–74. https://doi.org/10.1190/1.3284055

Van Heerden, W.L., (1987). General relations between static and dynamic moduli of rocks. Int. J. Rock Mech. Min. Sci. Geomech. Abstr. 24, 381–385. https://doi.org/10.1016/0148-9062(87)92262-5

Vermylen, J., Zoback, M.D., (2011). Hydraulic Fracturing, Microseismic Magnitudes, and Stress Evolution in the Barnett Shale, Texas, USA, in: SPE Hydraulic Fracturing Technology Conference. Society of Petroleum Engineers. https://doi.org/10.2118/140507-MS

Walls, J., Foster, M., (2017). Integrated Multi-Scale Reservoir Characterization : Wolfcamp Formation – Midland Basin 1420–1430.

Walls, J., Morcote-Rios, A., (2015). Quantifying Variability of Reservoir Properties From a Wolfcamp Formation Core. Proc. 3rd Unconv. Resour. Technol. Conf. 1–10. https://doi.org/10.15530/urtec-2015-2154633

Walsh, J.B., (1981). Effect of pore pressure and confining pressure on fracture permeability. Int. J. Rock Mech. Min. Sci. Geomech. Abstr. 18, 429–435. https://doi.org/10.1016/0148-9062(81)90006-1

Wang, J., Joseph, D.D., Patankar, N.A., Conway, M., Barree, R.D., (2003). Bi-power law correlations for sediment transport in pressure driven channel flows. Int. J. Multiph. Flow

29, 475–494. https://doi.org/10.1016/S0301-9322(02)00152-0

Warpinski, N.R., (1991). Hydraulic Fracturing in Tight, Fissured Media. J. Pet. Technol. 43, 146–209. https://doi.org/10.2118/20154-PA

Warpinski, N.R., (1990). Dual Leakoff Behavior in Hydraulic Fracturing of Tight, Lenticular Gas Sands. SPE Prod. Eng. 5, 243–252. https://doi.org/10.2118/18259-PA

Warpinski, N.R., (1985). Measurement of Width and Pressure in a Propagating Hydraulic Fracture. Soc. Pet. Eng. J. 25, 46–54. https://doi.org/10.2118/11648-PA

Warpinski, N.R., Branagan, P.T., (1989). Altered-Stress Fracturing. J. Pet. Technol. 41, 990–997. https://doi.org/10.2118/17533-PA

Warpinski, N.R., Lorenz, J.C., Branagan, P.T., Myal, F.R., Gall, B.L., (1993). Examination of a Cored Hydraulic Fracture in a Deep Gas Well. SPE Prod. Facil. 8, 150–158. https://doi.org/10.2118/22876-PA

Warpinski, N.R., Moschovidis, Z.A., Parker, C.D., Abou-Sayed, I.S., (1994). Comparison Study of Hydraulic Fracturing Models—Test Case: GRI Staged Field Experiment No. 3 (includes associated paper 28158). SPE Prod. Facil. 9, 7–16. https://doi.org/10.2118/25890-PA

Warpinski, N.R., Wolhart, S., (2016). A Validation Assessment of Microseismic Monitoring. SPE Hydraul. Fract. Technol. Conf. 9–11. https://doi.org/10.2118/179150-MS

Warren, J.E., Root, P.J., (1963). The Behavior of Naturally Fractured Reservoirs. Soc. Pet. Eng. J. 3, 245–255. https://doi.org/10.2118/426-PA

Waters, G.A., Heinze, J.R., Jackson, R., Ketter, A.A., Daniels, J.L., Bentley, D., (2006). Use of Horizontal Well Image Tools to Optimize Barnett Shale Reservoir Exploitation, in: SPE Annual Technical Conference and Exhibition. Society of Petroleum Engineers. https://doi.org/10.2118/103202-MS

Wattenbarger, R.A., El-Banbi, A.H., Villegas, M.E., Maggard, J.B., (1998). Production Analysis of Linear Flow Into Fractured Tight Gas Wells, in: SPE Rocky Mountain Regional/Low-Permeability Reservoirs Symposium. Society of Petroleum Engineers. https://doi.org/10.2118/39931-MS

Weijers, L., de Pater, C.J., Owens, K.A., Kogsbøll, H.H., (1994). Geometry of Hydraulic Fractures Induced From Horizontal Wellbores. SPE Prod. Facil. 9, 87–92. https://doi.org/10.2118/25049-PA

Weng, X., (1993). Fracture Initiation and Propagation From Deviated Wellbores, in: SPE Annual Technical Conference and Exhibition. Society of Petroleum Engineers, Houston, Texas. https://doi.org/10.2118/26597-MS

White, T., Clarke, P., Stephens, A., Laughland, M.M., Ye, H., (2014). Fault and Fracture Characterization from an Integrated Subsurface and Seismic Dataset: Impact on Well Performance of the Wolfcamp Shale, Midland Basin, West Texas. Proc. 2nd Unconv. Resour. Technol. Conf. 1–9. https://doi.org/10.15530/urtec-2014-1934166

Willingham, J.D., Tan, H.C., Norman, L.R., (1993). Perforation Friction Pressure of Fracturing Fluid Slurries, in: Low Permeability Reservoirs Symposium. Society of Petroleum Engineers. https://doi.org/10.2118/25891-MS

Wilson, K., Ahmed, I., MacIvor, K., (2016). Geomechanical Modeling of Flowback Scenarios to Establish Best Practices in the Midland Basin Horizontal Program. Proc. 4th Unconv. Resour. Technol. Conf. https://doi.org/10.15530/urtec-2016-2448089

Woodworth, T.R., Miskimins, J.L., (2007). Extrapolation of Laboratory Proppant Placement Behavior to the Field in Slickwater Fracturing Applications. SPE Hydraul. Fract. Technol. Conf. https://doi.org/10.2118/106089-MS

Wu, K., Olson, J.E., (2016). Mechanisms of Simultaneous Hydraulic-Fracture Propagation From Multiple Perforation Clusters in Horizontal Wells. SPE J. 21, 1000–1008. https://doi.org/10.2118/178925-PA

Xiong, H., Liu, S., Feng, F., Liu, S., Yue, K., (2019). Optimize Completion Design and Well Spacing with the Latest Complex Fracture Modeling & Reservoir Simulation Technologies – A Permian Basin Case Study with Seven Wells, in: SPE Hydraulic Fracturing Technology Conference and Exhibition, 5-7 February. The Woodlands, Texas, USA, pp. 1–22. https://doi.org/10.2118/194367-MS

Xiong, H., Wu, W., Gao, S., (2018). Optimizing Well Completion Design and Well Spacing with Integration of Advanced Multi-Stage Fracture Modeling & Reservoir Simulation - A Permian Basin Case Study, in: SPE Hydraulic Fracturing Technology Conference and Exhibition. Society of Petroleum Engineers, pp. 1–21. https://doi.org/10.2118/189855-MS

Xu, S., Zoback, M.D., (2015). Analysis of stress variations with depth in the Permian Basin Spraberry / Dean / Wolfcamp Shale. Am. Rock Mech. Assoc. 15–189.

Yew, C.H., Liu, G.H., (1993). The Fracture Tip and Critical Stress Intensity Factor of a Hydraulically Induced Fracture. Soc. Pet. Eng. 8, 171–177. https://doi.org/10.2118/22875-PA

Zhang, F., Adel, I.A., Park, K.H., Saputra, I.W.R., Schechter, D.S., (2018a). Enhanced Oil Recovery in Unconventional Liquid Reservoir Using a Combination of CO2 Huff-n-Puff and Surfactant-Assisted Spontaneous Imbibition, in: SPE Annual Technical Conference and Exhibition. Society of Petroleum Engineers. https://doi.org/10.2118/191502-MS

Zhang, F., Saputra, I.W.R., Adel, I., Schechter, D.S., (2018b). Scaling for Wettability Alteration

Induced by Addition of Surfactants in Completion Fluids: Surfactant Selection for Optimum Performance. Proc. 6th Unconv. Resour. Technol. Conf. https://doi.org/10.15530/urtec-2018-2889308

Zhang, F., Saputra, I.W.R., Adel, I.A., Schechter, D.S., (2018). Scaling for Wettability Alteration Induced by Addition of Surfactants in Completion Fluids: Surfactant Selection for Optimum Performance in: Unconventional Resources Technology Conference., in: URTeC. https://doi.org/10.15530/urtec-2018-2889308

Zhang, F., Saputra, I.W.R., Niu, G., Adel, I.A., Xu, L., Schechter, D.S., (2018c). Upscaling Laboratory Result of Surfactant-Assisted Spontaneous Imbibition to the Field Scale through Scaling Group Analysis, Numerical Simulation, and Discrete Fracture Network Model, in: SPE Improved Oil Recovery Conference. Society of Petroleum Engineers. https://doi.org/10.2118/190155-MS

Zhang, F., Saputra, I.W.R., Parsegov, S.G., Adel, I.A., Schechter, D.S., (2019). Experimental and Numerical Studies of EOR for the Wolfcamp Formation by Surfactant Enriched Completion Fluids and Multi-Cycle Surfactant Injection, in: SPE Hydraulic Fracturing Technology Conference and Exhibition. Society of Petroleum Engineers, The Woodlands, Texas, USA. https://doi.org/10.2118/194325-MS

Zhou, X., Ghassemi, A., Riley, S., Roberts, J., (2017). Biot ' s Effective Stress Coefficient of Mudstone Source Rocks. 51st US Rock Mech. / Geomech. Symp. held San Fr. California, USA, 25-28 June.

Zhou, X., Vachaparampil, A., Ghassemi, A., (2015). A combined method to measure Biot's coefficient for Rock. 49th US Rock Mech. / Geomech. Symp. 2015 4, 1–9.